*J. Earth Syst. Sci.* (2020)129 89
https://doi.org/10.1007/s12040-019-1313-4



# Physico-chemical conditions of crystallization and composition of source magma of the Grenvillian post-collisional mafic–ultramafic rocks in the Chhotanagpur Gneissic Complex, Eastern India

Susmita Das, Bapi Goswami* and Chittaranjan Bhattacharyya

*Department of Geology, University of Calcutta, 35, Ballygunge Circular Road, Kolkata 700 019, India.*
**Corresponding author. e-mail: bapigoswami69@gmail.com*

MS received 1 March 2019; revised 2 August 2019; accepted 16 October 2019

In the Chhotanagpur Gneissic Complex (CGC) of Eastern India a suite of mafic and ultramafic rocks occurs as sills, dykes and enclaves within porphyritic granitoid pluton. These mafic and ultramafic rocks and host porphyritic granitoids were emplaced in a post-collisional setting around 998 ± 10 Ma ago. Field occurrence, petrology and mineral chemistry of the mafic–ultramafic rocks have been studied. Both the mafic (Pl + Hyp + Di + Hbl + Bt + Mag + Spn ± Ol ± Spl) and ultramafic rocks (Di + Hyp + Bt ± Hbl ± Ol ± Pl ± Spl ± Ep ± Spn) are composed of same minerals but in different modal proportions. Plagioclase, clinopyroxene, orthopyroxene, amphibole, biotite and rarely olivine and spinel are important primary minerals of mafic–ultramafic suite. Primary amphiboles, biotites and pyroxenes show their affinity with shoshonitic lamprophyres. Chemically these rocks are similar to the kentallenite (of appinite suite) and are enriched in both compatible (Fe, Mg, Ni, and Cr) and incompatible (K, Ba, Rb, and LREE) elements and show crust-like trace element patterns. Crystallization of clinopyroxene before labradorite and presence of primary hornblende and biotite suggest high water content while biotite–magnetite–sphene assemblage suggests high $fO_2$ of the magma. Liquidus temperature (975–1088°C) of the parental magma of the mafic–ultramafic rocks was obtained by two-pyroxene thermometer. The pressure (2.9–5.7 kbar) and near-solidus temperature (782–819°C) of crystallization were determined using the amphibole–plagioclase geothermobarometry. Similar range of values of pressure, temperature and $fO_2$ values were obtained using other thermobarometers. High $H_2O$ and $fO_2$ (>NNO buffer) of the magma are characteristics of convergent setting. The mafic–ultramafic rocks of the suite probably crystallized from a magma which had high $SiO_2$ (48.16–67.64 wt%), high CaO (3.01–11.73 wt%), high $K_2O$ (1.34–4.49 wt%) and low $TiO_2$ (0.04–2.71 wt%) contents and intermediate Mg# (46.73 and 59.78).

**Keywords.** Mafic–ultramafic rocks; Chhotanagpur Gneissic Complex (CGC); physico-chemical parameters; magma composition.

## 1. Introduction

The simultaneous emplacement of granitoids and mafic and ultramafic suite of rocks characterize post-collisional magmatism. This specific magmatic association is relatively rare in nature but they are emplaced at the end of major orogenic episodes (Couzinié *et al.* 2014) and thus are very much useful to understand the evolution of lithosphere and asthenosphere. In the British Islands, the suite

Published online: 11 March 2020

of mafic–ultramafic rocks is known as 'Appinites' and calc-alkaline lamprophyres, which were emplaced at the end of Caledonian orogeny (Fowler *et al.* 2008). Such mafic–ultramafic rocks were emplaced during the end of Variscan orogeny in Europe and are diversely known as 'Vaugnerites' in the French massif central (Couzinié *et al.* 2014 and references therein), 'Durbachites' in the Czech Republic (Bowes and Košler 1993) and 'Shoshonites' or 'Appinites' in central Spain (Castro *et al.* 2003; Molina *et al.* 2009; Scarrow *et al.* 2009). Post-collisional mafic–ultramafic rocks have also been studied in the Dabie orogenic belt (Dai *et al.* 2015). Schaltegger (1997) suggested a possible genetic relation of this mafic–ultramafic magmatic suite with a paleosuture. The vaugnerite, durbachite, appinites and lamprophyres are considered to belong to shoshonitic series by Bowes and Košler (1993). All these rocks show remarkable chemical similarities. All these rocks are plotted in the shoshonitic field of the $SiO_2$–$K_2O$ diagram, recommended for the subdivision of the sub-alkaline rock series of the TAS diagram (Le Bas *et al.* 1986). They show similar N-MORB normalized trace-element patterns with significant enrichment in Ni and Cr, Large Ion Lithophile Elements (LILE) and Light Rare Earth elements (LREE), strong negative Nb and Ti anomalies, strong positive K and Pb anomalies and high LREE/HREE ratios, which are commonly seen in the magma, generated in subduction zone (reviewed by Scarrow *et al.* 2009). However, certain dissimilarities also prevail among them. For example, vaugnerites and lamprophyres are richer in $MgO/FeO_t$, LILE, LREE, HFSE and particularly Th and U concentrations than shoshonites (Scarrow *et al.* 2009). Thus, post-collisional mafic–ultramafic igneous rocks commonly display petrological and geochemical divergence and an enigmatic origin (Dai *et al.* 2015).

The parental mafic magma of these mafic–ultramafic rocks may be originated from partial melting of ultramafic mantle (Wyllie 1995), but similarities of some geochemical features with crustal rocks raises problem for their petrogenesis. Moreover, post-collisional mafic–ultramafic rocks are enriched in radiogenic isotopes which refute the possibility for their derivation from isotopically depleted normal asthenospheric mantle (Hofmann 1988). The continental crust-like geochemistry for these mafic rocks may be achieved either by (i) assimilation of crustal rocks by asthenospheric mantle derived magma during ascent or (ii) contamination of mantle ultramafic source by crustal material followed by subsequent melting of this contaminated mantle material. Diverse petrogenetic processes have been postulated to explain the physical and chemical characteristics of the post-collisional mafic–ultramafic suite and granitoids with which they are associated.

1. Mafic (lamprophyric), syenitic and granitic rocks of appinitic suite of Scotland are suggested cogenetic and can be correlated by fractionation and limited crustal assimilation process (Fowler and Henney 1996).
2. The sharp contacts, disparity on the volumes of basic and acidic rocks and different Nd isotope compositions of the members of the appinite suite of Scotland indicate that the granites were not formed by fractional crystallization of the parental magmas of appinite suite (Rapp *et al.* 2002; Macpherson *et al.* 2006).
3. The vaugnerites are suggested to be generated by melting of enriched phlogopite-(and/or amphibole-) bearing peridotite mantle. The contamination of mantle was due to the addition of 10–20% of crustal material during continental subduction shortly before the continent–continent collision (Ferré and Leake 2001; Couzinié *et al.* 2016).
4. The durbachites in the Moldanubian Zone of Bohemian Massif are suggested to be formed from the mixing between an upper mantle-derived melt and a crustal granitic melt followed by fractional crystallization (Janoušek and Holub 2007).
5. The durbachites of the northern extremity of the Bohemian Massif are suggested to be formed by mixing of felsic and mafic magmas (Slaby and Martin 2008). The mafic magma was generated by partial melting of a fertile peridotite, metasomatized by previous subduction processes (Slaby and Martin 2008).
6. Post-collisional mafic–ultramafic rocks of the Dabie–Sulu orogenic belt are suggested to be formed from melting of enriched peridotite of subcontinental lithospheric mantle sources which was enriched by melt produced from subducted continental crust (Jahn *et al.* 1999; Zhao *et al.* 2013; Dai *et al.* 2015). Solgadi *et al.* (2007) put forward a model involving partial melting of an enriched mantle at the transition from thickening to collapse of the Variscan orogenic belt for the emplacement of these suites of rocks.

In the Chhotanagpur Gneissic Complex (CGC) of Eastern India a suite of mafic and ultramafic

rocks including pyroxenite, hornblendite, peridotite, norite and gabbro are reported to occur in close temporal and spatial association with a shoshonitic porphyritic granitoid (Mandal *et al.* 2007; Goswami and Bhattacharyya 2014). These mafic and ultramafic rocks and host porphyritic granitoids were emplaced along the regional scale North Purulia Shear Zone (NPSZ). The host porphyritic granitoid intruded the crust around 998 ± 10 Ma ago (U–Pb zircon dating by LA-ICPMS analysis, see Chakraborty *et al.* 2019).

The aims of the present study are (1) to document the geology, petrology, mineral chemistry and rock chemistry of the Neoproterozoic mafic–ultramafic suite occurring in close spatial and temporal association with shoshonitic porphyritic granitoid of Raghunathpur, Purulia and (2) to establish the nature of the source magma for the Purulia mafic–ultramafic suite using mineral chemistry and geochemical data.

## 2. Geology of the study area

The present study area belongs to the Chhotanagpur Gneissic Complex (CGC) of the Central Indian Tectonic Zone that reflects the amalgamation of South and North Indian cratonic blocks during Grenvillian times (Radhakrishna and Naqvi 1986; Bhowmik *et al.* 2012; Goswami and Bhattacharyya 2014; figure 1). The CGC represents a migmatitic granite gneiss terrain with enclaves of older metaigneous and metasedimentary rocks metamorphosed under amphibolite to granulite facies. The granitoid gneisses are intruded by younger basic, granitic and alkaline–peralkaline intrusives (figure 1) (Mahadevan 2002). In the CGC, convergence and continental collision gave rise to the emplacement of several granite bodies including the porphyritic granitoid batholith of Raghunathpur (Goswami *et al.* 2018).

A medium to coarse grained felsic biotite/hornblende migmatitic gneiss characterized by alternate biotite ± hornblende bearing melanosomes and quartzo-feldspathic leucosomes represents the oldest rock type in this area (figure 1). This migmatitic gneiss occurs to the north of the nearly ENE–WSW trending Raghunathpur porphyritic granitoid batholith (figure 1c). Axial planes of the megascopic $D_2$ folds of the amphibolite facies migmatitic gneisses show moderate northerly dip (Goswami and Bhattacharyya 2008). Porphyritic granitoids intrude the migmatitic gneiss country (Sen 1956; Goswami and Bhattacharyya 2008; see also figure 2(e) in Karmakar *et al.* 2011). The third phase deformation ($D_3$) produced ENE–WSW trending regional shear zones, which is steeply dipping to the N, with steeply plunging mineral lineation. The shear zone passes along the northern boundary of the porphyritic granitoid batholith and demarcates roughly the amphibolite facies of the northwestern part from the granulite facies of the southeastern part of the area. The boundary between the amphibolite facies terrain (WNW) and the granulite facies terrain (ESE) is sharp, and there is no gradational change in mineral composition of amphibolites from amphibolite facies terrain to basic granulites of the southeastern part. South of the southern boundary of the porphyritic granitoids, the country rock granitoids are highly sheared in nature. The peripheral zone of the porphyritic granitoids itself is also sheared and feldspar megacrysts are transformed into augens; however, the central part the porphyritic granitoids shows magmatic flow foliation defined by the preferred alignment of K-feldspar megacrysts. Turbulent flow of magma defined by haphazard orientations of K-feldspar megacrysts is also not uncommon (see Goswami and Bhattacharyya 2008, 2014 for details).

The mafic–ultramafic rocks of the present study are found closely associated in field and are more common near the southern boundary of the porphyritic granitoid batholith and show east–west trend parallel to the trend of elongation of porphyritic granitoid body and parallel to the strike direction of regional shear zone.

The mafic and ultramafic rocks of present study usually occur as small dykes and sills running parallel and also transverse to the flow foliation of the porphyritic granitoids (figure 2a), or mafic magmatic enclaves in coeval porphyritic granitoids. The contact of porphyritic granitoids with adjoining mafic sill/ dyke is lobate (figure 2a). The mafic dykes depict injection of mafic magma along early fractures developed in the crystallizing granitoid body during cooling (Barbarin 2005). One mappable body (length 1250 m and thickness 500 m) of mafic–ultramafic rock whose composition varies between websterite and hornblende norite, was encountered in and around Palashkura. The pyroxenite shows prominent banding in this body (figure 2b). These ultramafic cumulates are interpreted as autoliths, formed from the fractional crystallization of parental homogenized magma (Barbarin 2005). Also, at many places along the

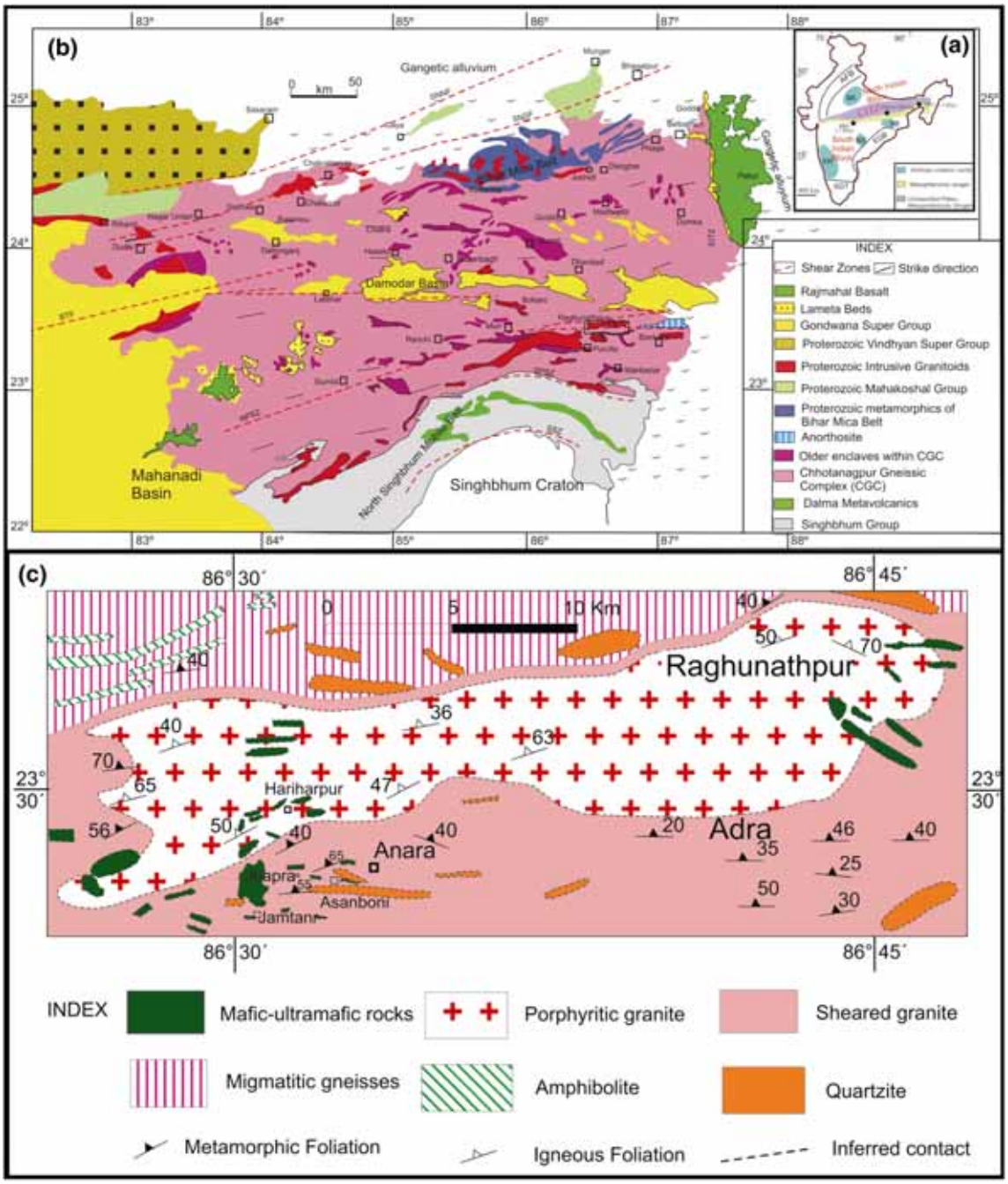


Figure 1. (**a**) Main tectonic domains of India (inset figure on the top right corner) and sketch map showing the Precambrian geology of the Central Indian Tectonic Zone and adjacent areas. (**b**) Simplified geological map showing the distribution of main lithological units within the CGC (based on the data compiled from Mazumdar 1988; Mahadevan 2002; Acharya 2003). (**c**) Schematic geological map of Anara and Raghunathpur areas from northern Purulia in the eastern part of CGC showing the distribution of porphyritic granitoids and mafic–ultramafic rocks (modified after GSI 1977; Mandal *et al.* 2007; Goswami and Bhattacharyya 2014). Explanations: (**a**) AFB, Aravalli Fold Belt; BK, Bundelkhand craton; CITZ, Central Indian tectonic Zone; CGC, Chhotanagpur Gneissic Complex; SPGC, Shilong Plateau Gneissic Complex; BBG, Bhandara–Balaghat granulite; SB, Singhbhum craton; BS, Bastar craton; KR, Karnataka craton; EGB, Eastern Ghats Mobile Belt; SGT, Southern Granulite terrain. (**b**) SNNF, Son-Narmada North Fault; SNSF, Son-Narmada South Fault; BT, Balarampur-Tattapani Fault; NPSZ, North Purulia Shear Zone; SPSZ, South Purulia Shear Zone; SSZ, Singhbhum Shear Zone.

contact of porphyritic granitoid and mafic rocks, there occurs a variegated rock with irregularly distributed felsic and mafic patches of varying dimensions (figure 2c). Enclaves of mafic igneous rocks often contain megacrysts of K-feldspar, derived from the surrounding porphyritic

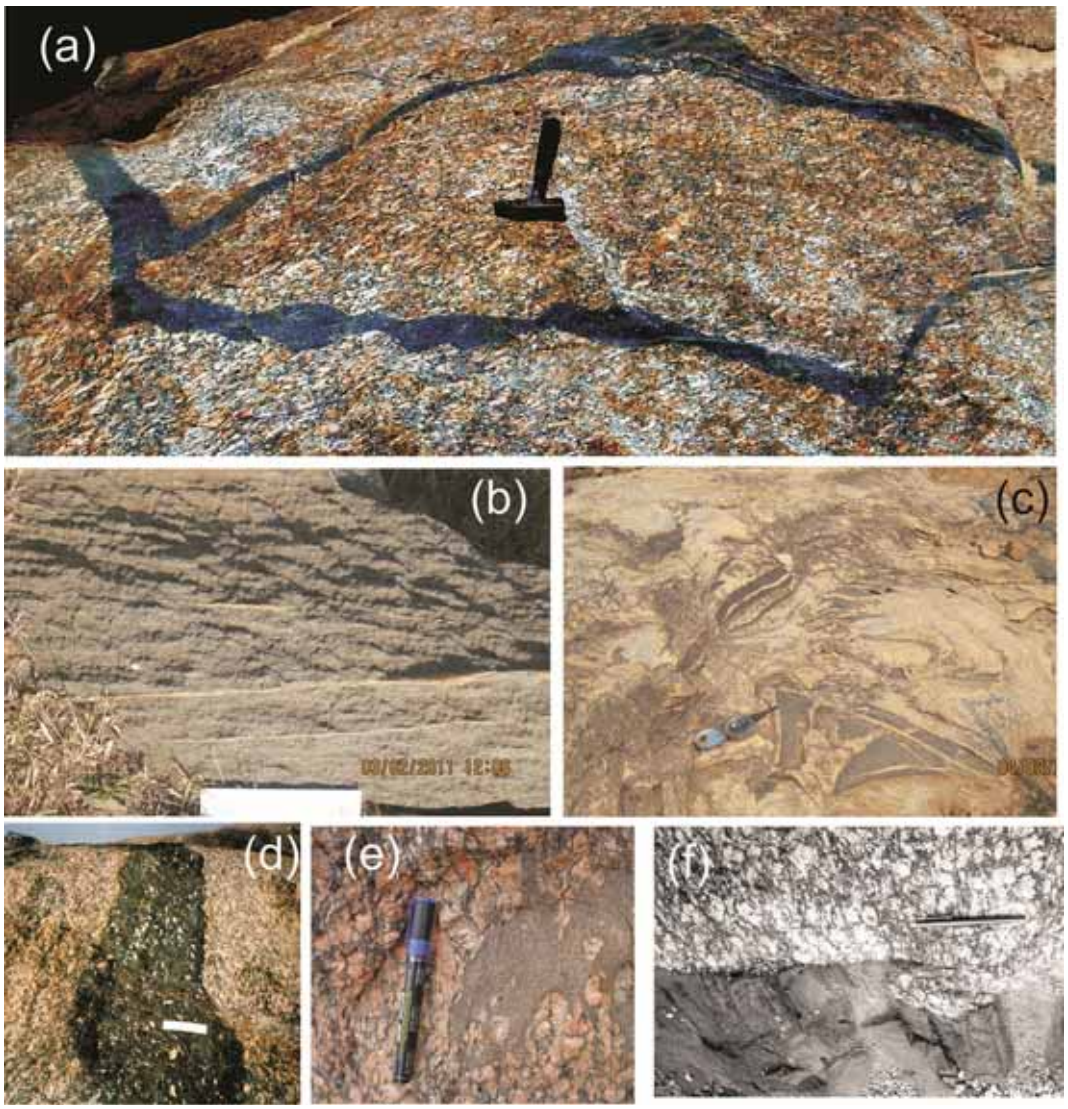


Figure 2. (**a**) Intrusion of basic magma along and across the foliation of the porphyritic granitoids. Note the lobate margin of the basic rocks. Location: Harai river section, hammer = 45 cm. (**b**) Banding formed by cumulate minerals in pyroxenite. Note: injection of granitic material along fractures cutting across the bands, white scale = 14 cm. (**c**) Irregularly distributed mafic rocks within granitoid, scale = Brunton compass. (**d**) Megacrysts of K-feldspar within mafic rock suggesting mixing of felsic and mafic magma, white scale = 14 cm. (**e**) Mesocratic mafic microgranular enclave shows sharp contact with the host porphyritic granitoids. Note that the mafic rock engulfs the K-feldspar megacryst. (**f**) Mafic dyke intrudes the porphyritic granite. Note the apophyses of basic rock within the granite. Pen = 15.5 cm, location: Bero Hills.

granitoids (figure 2d and e). Such enclaves are described as hybrid-type enclaves by Bora *et al.* (2013). Incorporation of K-feldspars into mafic magma indicates that the host granitoid magma was affected by strong internal movement during its emplacement and crystallization (Slaby and Martin 2008). Mesocratic mafic microgranular enclaves show sharp contact with the host porphyritic granitoids (figure 2c and e). Linear mafic dyke has also intruded the porphyritic granite in Bero Hills showing apophyses (figure 2f). Thus, with increasing viscosity contrast between mafic and felsic magma, the occurrences of mafic magma transform from rounded mafic magmatic enclaves, to sills and dykes with lobate margins and finally to dykes with straight margins. Similar relationships between mafic and felsic rocks are suggested as the result of injection of mafic magma into the granitoid over the entire crystallization history (cf. Slaby and Martin 2008; Jayananda *et al.* 2009; Kumar 2014).

The host porphyritic granitoid intruded the crust around 998 ± 10 Ma ago (U–Pb zircon dating by LA-ICPMS analysis, see Chakraborty *et al.* 2019). Since mafic–ultramafic rocks are shown to be emplaced during or slightly later than the

emplacement of porphyritic granitoids, we can assume that the mafic–ultramafic rocks emplaced around 998 ± 10 Ma ago.

## 3. Petrography

Below, we give a summary of previously published (Mandal *et al.* 2007) and new data pertaining to the petrography of the different lithounits distinguished within the mafic–ultramafic suite. The mafic–ultramafic rocks are sporadically found as magmatic enclaves and small sills or dykes in the porphyritic granitoid batholith and are characterized by the ubiquitous presence of amphibole and/or biotite. Near the southern margin of the porphyritic granitoid batholith, the mafic–ultramafic bodies are affected by shearing and no detailed studies have been made with the sheared samples.

### 3.1 *Mafic rocks*

These dark coloured, coarse-grained rocks generally show cumulate and ophitic texture and sometimes show crude banding which is defined by irregular discontinuous mafic layers, composed dominantly of hornblende–biotite aggregates with hypersthenes, within discontinuous parallel runs of felsic mass. Modes (vol.%) are given in table 1. Compositionally mafic rocks are broadly classified as norite, clinopyroxene norite and orthopyroxene gabbro (figure 3a–c). The colour index (M) varies from ∼59 to ∼89 for most of the samples (table 1). Few samples show some degree of metamorphism related to the shearing which are prefixed with meta-.

Plagioclase (labradorite to andesine) occurs as coarse criss-cross tabular plates and laths. Further, aggregates of subequant grains of medium to fine-sized plagioclase occur throughout the rocks. Frequently thin greenish yellow and yellowish green veins traverse through the plagioclase grains. Occasionally potash feldspar replaces plagioclase along the contact giving rise to replacement antiperthite. Olivine grains are generally mantled by orthopyroxene and the coronal grain occurs within plagioclase (figure 4a). Olivine may contain inclusions of spinel and magnetite (figure 4b). Medium to coarse-sized subhedral grains of clinopyroxene (diopside) are commonly associated with both hypersthene and hornblende, and in places, occur within aggregates of plagioclase. Inclusions of small grains of clinopyroxene occur frequently within plagioclase lath (figure 4c) and occasionally following the cleavage traces (figure 4d). Inclusions of clinopyroxene within labradoritic plagioclase suggest that the former crystallized earlier than plagioclase, a characteristic of hydrous calc-alkaline magma (Müntener *et al.* 2001). Hypersthene (strongly pleochroic from pale green to pale pink) occurs as coarse sub-idiomorphic grains. Pyroxenes are replaced by both hornblende and biotite which is a very common phenomenon in plutonic mafic rocks and is suggested to be due to the reaction taking place between anhydrous pyroxene and hydrous melt (Beard *et al.* 2004). Euhedral inclusions of hornblende (pleochroic from yellowish green to dark green, $Z\hat{}C = 22°$) are frequently noticed within plagioclase (figure 4e) suggesting their magmatic crystallization. Hornblende also occurs mantling plagioclase in some slides (figure 4f). Sometimes hornblende occurs as coarse to medium-sized anhedral to subhedral grains along the contact of pyroxene and plagioclase but the absence of turbidity in plagioclase in such mineral assemblage tends to suggest that these hornblendes, in all probability, have not been formed by metamorphism. Biotite (pleochroic from straw yellow to dark greenish brown) occurs as clusters of coarse to medium-sized laths. Phlogopitic biotites (orange-yellow to almost colourless) often occur as large plates poikilitically enclosing early formed pyroxene, plagioclase and amphiboles (figure 4f). Thus, both amphibole and biotites of the present rock suite are primary in nature. At places, biotites show kinking. Opaque minerals occur as medium-sized subhedral to anhedral grains in the interspaces of ferromagnesian minerals and occasionally fine grains or their aggregates occur as inclusions in the latter.

### 3.2 *Ultramafic rocks*

Modes of the representative samples are given in table 1. These rocks comprise plagioclase-bearing pyroxenite (figure 3c), olivine pyroxenite, olivine hornblende–pyroxenite, olivine pyroxene–hornblendite, and olivine hornblendite (figure 3d). All these types are coarse-grained and massive except plagioclase-bearing pyroxenite which is medium to coarse grained.

#### 3.2.1 *Plagioclase-bearing pyroxenite*

The rock shows mesoscopic banding in exposure (figure 2b). Under microscope the rock is

Table 1. *Modes (vol.%) of representative ultramafic and mafic intrusives of Purulia.*

| | Mela olivine hornblende clinopyroxene norite | Mela clinopyroxene norite | Hornblende clinopyroxene (meta) norite | Olivine hornblende clinopyroxene (meta) norite | Mela-olivine orthopyroxene gabbro | Mela hornblende orthopyroxene gabbro |
|---|---|---|---|---|---|---|
| Serial no. | 1 | 2 | 3 | 4 | 5 | 6 |
| Sample no. | 39 | 43 | 47a | 47b | 42 | BG/25 |
| Olivine | 6.8 | 0.0 | 0.0 | 3.3 | 6.5 | 0 |
| Serpentine | 0.0 | 0.0 | 0.0 | 0 | 0 | 0 |
| Hypersthene | 36.6 | 39.5 | 31.8 | 31.1 | 19.5 | 15.6 |
| Diopside | 9.8 | 27.5 | 4.3 | 4.5 | 43.0 | 35.3 |
| Titanaugite | 0.0 | 0.0 | 0.0 | 0 | 0 | 0 |
| Hornblende | 7.1 | 0.0 | 6.2 | 6.0 | 0.0 | 17.1 |
| Tremolite + Actinolite | 0.0 | 0.0 | 0.0 | 0 | 0 | Trace |
| Biotite | 10.0 | 5.5 | 18.3 | 0 | 12.6 | 12.2 |
| Phlogopite | | | | 13 | | |
| Chlorite | 5.3 | | | | | |
| Plagioclase | 21.0 | 25.0 | 39.1 | 40.9 | 14.1 | 18.7 |
| Magnetite | 3.6 | 2.2 | 0.3 | 0.9 | 3.9 | 1.1 |
| Sphene | | | 0 | | 0.6 | |
| **Total** | 100.1 | 99.7 | 100.0 | 99.7 | 100.2 | 100.0 |
| Colour index | 79.1 | 74.7 | 60.9 | 58.8 | 87.8 | 84.4 |

| | Olivine pyroxenite | Olivine hornblende pyroxenite | | | Plagioclase bearing Pyroxenite | | | | Olivine pyroxene hornblendite | Olivine hornblendite |
|---|---|---|---|---|---|---|---|---|---|---|
| Serial no. | 7 | 8 | 9 | 10 | 11 | 12 | 13 | 14 | 15 | 16 |
| Sample no. | AD 443C | SM 46B | SM 11 | SD 21a | 41 | SM 46A | 28 | 46 | SM 170A | SM 299 |
| Olivine | 16.7 | 9.8 | 15.0 | 19.3 | 0.0 | 0.0 | 0.0 | 0.0 | 11.2 | 21.3 |
| Serpentine | 0.0 | 0.0 | 13.7 | 0.0 | 0.0 | 0.0 | 0.0 | 0.0 | 1.6 | Trace |
| Hypersthene | 19.7 | 37.3 | 37.3 | 7.2 | 35.4 | 39.9 | 19.4 | 9.8 | 27.9 | 4.9 |
| Diopside | 35.4 | 24.1 | 10.3 | 0.0 | 42.8 | 44.8 | 58.5 | 34.2 | 0.0 | 0.0 |
| Titanaugite | 0.0 | 0.0 | 0.0 | 35.5 | 0.0 | 0.0 | 0.0 | 0.0 | 0.0 | 0.0 |
| Hornblende | 7.8 | 9.3 | 4.6 | 16.6 | 3.2 | 0.0 | 0.0 | 0.0 | 49.4 | 73.2 |
| Tremolite + Actinolite | 0.0 | Trace | 0.0 | 0.0 | 0.0 | 0.7 | 0.0 | 0.0 | 0.0 | 0.0 |
| Biotite + Phlogopite | 10.2 | 10.7 | 9.2 | 12.8 | 13.2 | 4.7 | 0.0 | 50.9 | 0.0 | 0.0 |
| Plagioclase | 9.1 | 7.0 | 8.0 | 8.0 | 4.6 | 8.9 | 1.7 | 1.5 | 0.0 | 0.0 |
| Spinel | 0.0 | 0.0 | 0.0 | 0.0 | | 0.0 | | | 5.3 | Trace |
| Rutile | 0.0 | 0.0 | 0.0 | 0.0 | | Trace | | | 0.0 | 0.0 |
| Calcite | 0.0 | 0.0 | 0.0 | 0.0 | | 0.0 | | | 1.8 | 0.0 |
| Magnetite | 1.1 | 0.9 | 1.3 | 0.7 | 0.8 | 1.2 | | 3.5 | 3.2 | 0.6 |
| Epidote | | | | | | | 14.1 | | | |
| Sphene | | | | | | | 2.3 | 0 | | |
| **Total** | 100.0 | 99.1 | 99.4 | 100.1 | 100.0 | 100.2 | 100.0 | 99.9 | 100.4 | 100.0 |
| Colour index | 90.9 | 92.1 | 91.4 | 92.1 | 95.4 | 91.3 | 94.3 | 98.4 | 100.4 | 100.0 |

Data source. 1–6, 11, 13, 14: present study; 7–10, 12, 15, 16: Mandal *et al.* (2007).

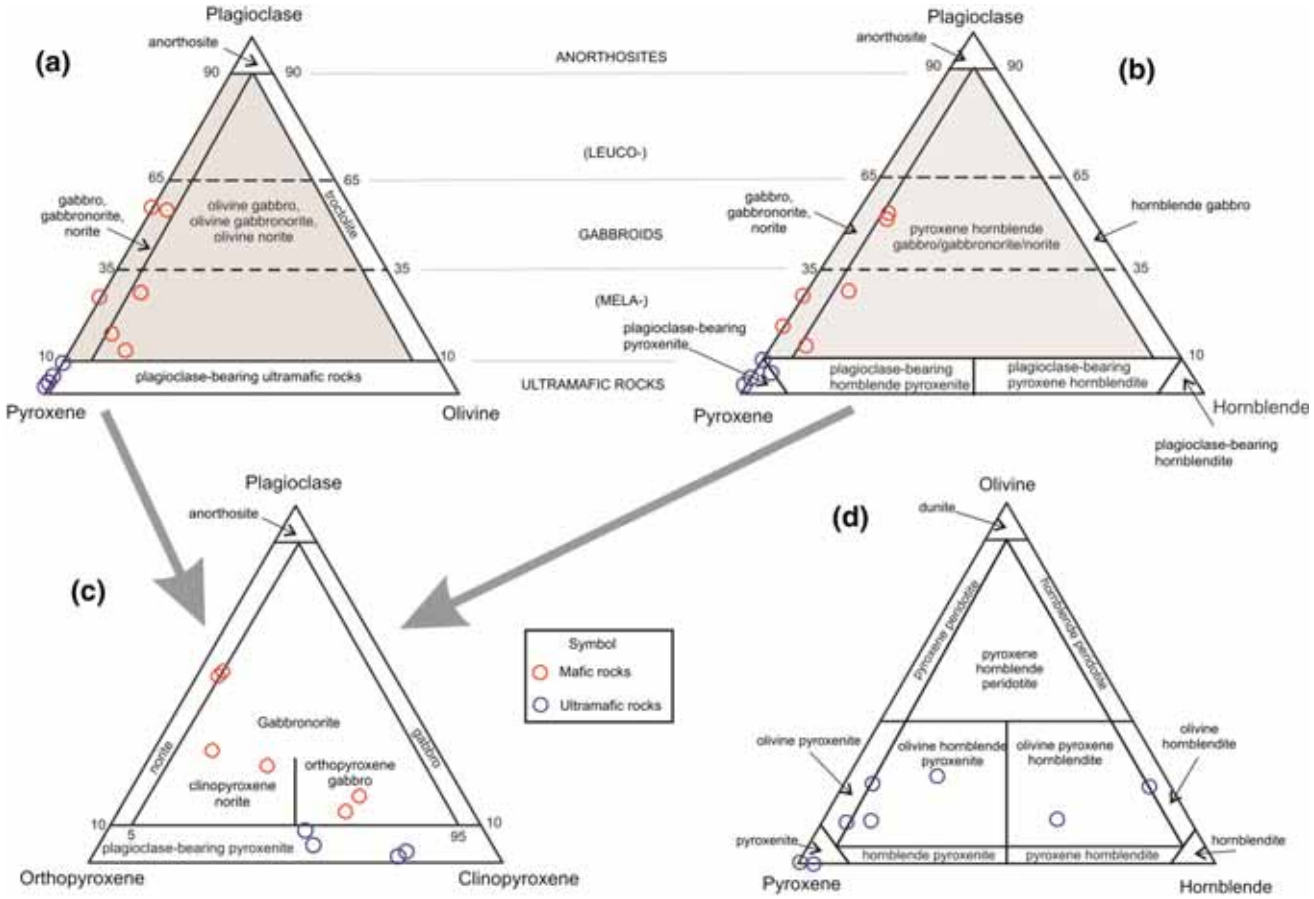


Figure 3. Classification of mafic–ultramafic rocks of present study area following IUGS (Le Maitre 2002).

characterized by cumulus aggregate of coarse subhedral stumpy plates and equant grains of diopside with which are intimately associated hypersthene and sporadic intercumulus plagioclase (figure 4g). Diopside is the predominant pyroxene and occurs as subidiomorphic to xenomorphic phenocrysts. Occasionally coronas of hornblende and biotite around clinopyroxene are present (figure 4h). Hypersthene (pleochroic from pale pink to colourless) occurs generally as coarse subidiomorphic grains most of which are short prismatic and contain inclusions of medium-sized diopside. It occurs also as fine to medium-sized grains with or without forming aggregates in the groundmass. Needle-shaped and fine laths of biotite and hornblende occur as alteration products along cleavage of orthopyroxene. Biotite (pleochroic from dark reddish brown to pale yellowish brown) occurs as subhedral grains in association with pyroxene and plagioclase. Plagioclase occurs as subidiomorphic medium-sized intercumulus fresh grains within aggregates of hypersthene and diopside. Zoning is occasionally present. Deformed twin lamellae in some plagioclase laths indicate later deformation. Hornblende (pleochroic from pale yellowish green to yellowish green, $Z^{\wedge}C = 21°$) occurs as medium-sized xenoblastic to subidioblastic, subequant to slightly elongate grains. Fine irregular specks of sphene may be present as minor accessory associated with the ferromagnesian minerals. Rutile occurs as extremely fine haphazardly oriented needles within some clinopyroxene phenocrysts.

### 3.2.2 *Olivine–hornblende pyroxenite*

These are also characterized by cumulous aggregate of coarse subhedral stumpy plates and equant grains of predominant diopside with which are intimately associated enstatite, hypersthene, olivine and sporadic intercumulous plagioclase, amphibole, phlogopite, and opaque minerals. Early formed euhedral grains of clinopyroxene are surrounded by plagioclase (figure 4i). Diopside plates frequently contain:

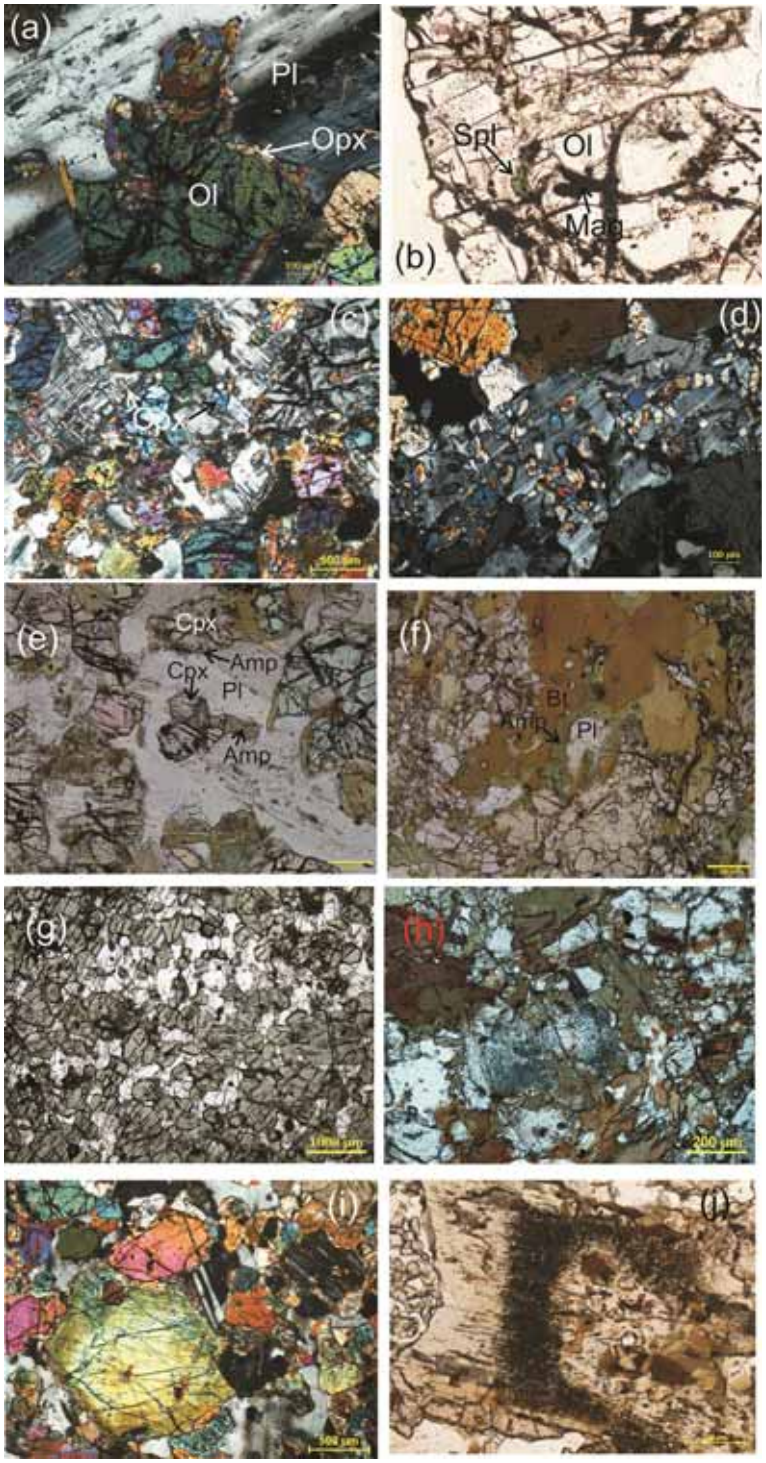


Figure 4. Textural attributes from olivine hornblende clinopyroxene norite. (**a**) Olivine grain mantled by orthopyroxene grains is enclosed by plagioclase. (**b**) Inclusion of spinel and magnetite within olivine. (**c**) Inclusion of clinopyroxene along the cleavage of plagioclase. (**d**) Inclusions of small grains of clinopyroxene within plagioclase lath. (**e**) Euhedral pyroxene and hornblende poikilitically enclosed within plagioclase (a to e from sample SD47b) (**f**) Multilayered corona of amphibole and biotite around plagioclase (sample H2). (**g**) Cumulus aggregates of pyroxenes with intercumulus plagioclases in plagioclase pyroxenite (sample SD28). (**h**) Corona of amphibole and biotite around pyroxene in plagioclase pyroxenite (sample SD46). (**i**) Early formed euhedral grain of clinopyroxene surrounded by plagioclase in olivine hornblende pyroxenite. Sample SM46B. (**j**) Crowds of fine opaque needles forming a zone, the needles being oriented parallel to prismatic cleavage of the host diopside in plagioclase pyroxenite (sample SD46).

(i) grey or dark grey thin stringers which may be bastitic alterations along the cleavage, (ii) irregular patches of phlogopite through which prismatic cleavage of pyroxene is occasionally continuous, (iii) irregular patches or crowds of fine opaque needles, the needles being oriented parallel to prismatic cleavage of the host diopside, and possibly have formed due to exsolution (figure 4j), (iv) irregular patches of green-brown hornblende, particularly along the contact with plagioclase, and (v) inclusions of subrounded grains of olivine. Corona of hypersthene occurs around olivine. Coarse subidiomorphic and short prismatic grains of hypersthene are common. It contains inclusions of both medium-sized olivine and diopside. Olivine ($Fo_{68\text{-}75}$) of chrysolite variety mostly occurs as coarse, equant, subhedral or slightly elongate grains in the intergranular space formed between cumulate pyroxenes and sometimes as subrounded grains enclosed by orthopyroxene and/or clinopyroxene. It is frequently enclosed successively by thin coronal rims of orthopyroxene and amphibole in contact with plagioclase. Some olivine grains are conspicuously serpentinized with release of minute magnetites. Amphibols are of two types; the predominant one is greenish brown or brownish green hornblende (X = pale green, Y = green, Z = brownish green to greenish brown; $Z'\wedge C = 19°–21°$), which occurs as corona around orthopyroxene along the contact with plagioclase, as already mentioned or along the contact of pyroxene–olivine or pyroxene–plagioclase; the greenish colour is stronger just along the contact with plagioclase. In places, it replaces pyroxenes due to the reaction taking place between anhydrous pyroxene and hydrous melt (Beard *et al.* 2004). The other type is fibrous greenish tremolite–actinolite association which generally occurs forming the outer rim of hypersthene corona (around olivine) in contact with plagioclase. Brownish green to greenish brown hornblende occurs throughout the rock as medium-sized subidiomorphic to xenomorphic grains along the contacts of pyroxene or pyroxene–plagioclase. Biotite occurs sporadically as skeletal grains occupying the vacant space remaining after the crystallization of the cumulous pyroxenes and occasionally associated with hornblende plates. Coarse, subhedral, skeletal laths occur in the intergranular spaces of olivine, olivine–pyroxene, pyroxene–plagioclase and olivine–plagioclase grains. Some coarse laths contain inclusions of medium-sized olivine and also pyroxene. Plagioclase ($An_{47}$–$An_{57}$) occurs as medium to coarse subhedral intercumulous to cumulous grains between olivine and pyroxene. Zoning is occasionally present. Spinel is a very minor accessory and occurs as fine irregular specks associated with the ferromagnesian minerals.

#### 3.2.3 *Olivine–pyroxene–hornblendite and olivine–hornblendite*

These massive, coarse-grained rocks are composed predominantly of hornblende with subordinate olivine, hypersthene, magnetite, serpentine and spinel. These rocks show an aggregate of short, stumpy, prismatic grains of hornblende showing cumulous texture with few relatively olivine-rich layers alternating with thicker hornblende-rich bands. Both subordinate hypersthene and opaque are more or less uniformly distributed within aggregates of hornblende ($Z'\wedge C = 18°$, Z′ = green, Y′ = light green, X′ = pale yellowish green) which occurs as short prismatic, idiomorphic to subidiomorphic crystal cumulates. Olivine, occasionally with serpentinized cracks containing fine subidiomorphic magnetite, occurs dominantly as medium to fine idiomorphic to xenomorphic grains. Hypersthene occurs as medium to coarse subidiomorphic to xenomorphic grains interstitial to hornblendes and also closely associated with olivine. Magnetite, apart from occurring mostly as fine grains in the serpentinized cracks, is also present as medium and coarse grains sporadically throughout the rock. Spinel occurs as rare accessory at the interstices of olivine–hornblende–magnetite.

## 4. Analytical techniques

The analysis of the representative minerals in polished sections of the rock samples was performed by a CAMECA SX100 microprobe with wavelength dispersive spectrometers at the Central Petrology Division, Geological Survey of India, Kolkata. An accelerating voltage of 15 kV was maintained with a beam current of 12 nA. Beam diameter was fixed at 1 μ. All natural standards were used for precision and correction. Whole rock major and trace element compositions of 8 samples of mafic and ultramafic rocks were determined by X-ray fluoroscence analyses in the Department of Geology, Presidency University, Kolkata, West Bengal, using Axios XRF spectrometer, manufactured by PANalytical, Netherlands. Samples were crushed and carefully chosen to avoid the weathered surfaces and reduced to powder form (200 mesh) with agate mortar.

## 5. Mineral chemistry

### 5.1 *Plagioclase*

Representative chemical compositions of plagioclase and their structural formulae are given in table 2. Considerable variations in the anorthite content of plagioclases of the studied rocks have been noticed (figure 5). It is more calcic ($An_{98.5}$) in plagioclase–epidote-bearing pyroxenite (the only epidote bearing sample in table 1) than those in plagioclase bearing pyroxenite ($An_{64.4–52.9}$) and websterite ($An_{51.6–40.5}$) (figure 5). The lower anorthite content of plagioclase of mafic rocks than that of the ultramafic rocks is indicative of its differentiated nature. The anorthite content of plagioclase crystals from plagioclase–epidote-bearing pyroxenite lies above the range ($An_{75–94}$) reported from the Zabargad peridotite–pyroxenite of mantle origin (Piccardo *et al.* 1988). The analyzed plagioclases are depleted in $K_2O$ (0.0–0.20 wt%).

### 5.2 *Clinopyroxene*

Clinopyroxenes were analyzed from plagioclase–epidote bearing pyroxenite, plagioclase-bearing hornblende pyroxenite, websterite, metanorite and hornblende gabbro-norite. Representative chemical compositions, structural formulae and end-member percentage of these clinopyroxenes are shown in table 3. The clinopyroxenes are dominantly diopside except one sample of plagioclase-bearing hornblende pyroxenite and one of websterite, which is classified as augite (figure 6a). Mg# of these clinopyroxenes decreases from plagioclase-bearing hornblende pyroxenite (86.8–83.6) through websterite (84.5–80) to plagioclase–epidote-bearing pyroxenite (63.7–61.5), a feature consistent with their crystallization from a fractionating magma. In metanorite and hornblende gabbro-norite the Mg# of clinopyroxenes varies between 88.3–81.5 and 85.1–80.9, respectively. The lower Mg# of clinopyroxenes from the ultramafic samples (86.8–61.5) compared to those from mafic rocks olivine metanorite/hornblende gabbro-norite (88.3–80.9) seems unusual in that clinopyroxene from the ultramafic rocks should have the higher Mg# than those of mafic rocks. The lower Mg# of olivine ($Fo_{72.03}$) and orthopyroxene (En73.94–76.22) in the ultramafic rocks (see later sections) could have made the magma relatively Mg-rich resulting in more magnesian clinopyroxene in the mafic rocks.

The compositional range of clinopyroxene falls within the field of shoshonitic lamprophyre (figure 6a) except the plots from plagioclase–epidote pyroxenite which lie outside the field. In all the rock samples clinopyroxenes have relatively low $TiO_2$ content (0–0.84 wt%) than $Al_2O_3$ (1.24–6.05 wt%). The clinopyroxene from shoshonitic lamprophyres also show similar characters with $Al_2O_3 > TiO_2$ (Rock 1991). When plotted in the $SiO_2$ (wt%) *vs.* $Al_2O_3$ (wt%) binary diagram (after Le Bas 1962) the clinopyroxenes plot within the sub-alkaline field (figure 6b). In the $TiO_2$ (wt%) *vs.* $Al_2O_3$ (wt%) diagram plots of the clinopyroxenes are mostly restricted within the calc-alkaline field (figure 6c). However, all the the clinopyroxenes, except one, of the mafic–ultramafic rocks of the present study are plotted within the alkaline field in the Ti *vs.* Ca + Na diagram (figure 6d) (after Nisbet and Pearce 1977). It is obvious from field evidence and petrography that the mafic–ultramafic rocks are igneous intrusions in the porphyritic granitoids. Whatever may be the stage of crystallization of the porphyritic granitoids at the time of emplacement of mafic–ultramafic magma, there is every possibility of migration of alkalies from porphyritic granitoids to the crystallizing mafic–ultramafic magmas. As a result, the difference in the degree of migration of alkalies towards the different mafic–ultramafic bodies or even the same body of each has given rise to differential amount of alkalies in these bodies culminating in the alkaline/sub-alkaline/calc-alkaline types of the mafic–ultramafic rocks. Most of the clinopyroxenses fall in the field of arc-cumulte-type intrusion in the $TiO_2$ *vs.* $Al_z$ ($Al^{iv} * 100/2$) diagram (figure 6e) (after Loucks 1990).

### 5.3 *Orthopyroxene*

The representative orthopyroxenes have been analyzed from plagioclase-bearing pyroxenite, websterite and plagioclase hornblende pyroxenite, plagioclase-bearing hornblende pyroxenite and metanorite (table 4). The orthopyroxenes show restricted range in Mg# varying between 81.2–73.5 and plot in the enstatite field (figure 6a). The orthopyroxenes in websterite are characterized by slightly higher CaO component (0.28–2.2 wt%) than those of plagioclase-bearing pyroxenite (0.25–0.36 wt%), plagioclase-bearing hornblende pyroxenite (0.04–0.35 wt%) and metanorite (0.02–0.35 wt%). The $Na_2O$ component of orthopyroxene is low in all these rocks. The $Al_2O_3$ content is relatively higher in orthopyroxene from websterite (1.43 to 1.9 wt%) and

Table 2. *Representative analyses of plagioclase from mafic and ultramafic intrusives and cationic calculations on the basis of 32 oxygen.*

| Sample | 28 | 28 | 41 | 41 | 41 | 41 | 41 |
|---|---|---|---|---|---|---|---|
| Analysis | 81/1 | 86/1 | 10\1 | 16/1 | 17/1 | 20/1 | 21/1 |
| Location | | | Rim | Core | Rim | Core | Rim |
| $SiO_2$ | 42.07 | 43.13 | 52.58 | 52.36 | 53.87 | 53.33 | 54.57 |
| $TiO_2$ | 0 | 0.06 | 0 | 0.16 | 0.06 | 0 | 0 |
| $Al_2O_3$ | 36.26 | 36.38 | 28.75 | 28.53 | 28.33 | 28.27 | 28.2 |
| FeO | 0.05 | 0.09 | 0.14 | 0.12 | 0.29 | 0.08 | 0.2 |
| MnO | 0 | 0.01 | 0.03 | 0 | 0 | 0.09 | 0 |
| MgO | 0.01 | 0 | 0.05 | 0.02 | 0.04 | 0 | 0.07 |
| CaO | 20.01 | 20.06 | 11.56 | 11.73 | 11.05 | 11.21 | 10.85 |
| $Na_2O$ | 0.17 | 0.16 | 4.57 | 4.51 | 5.06 | 5.01 | 5.22 |
| $K_2O$ | 0.01 | 0 | 0.1 | 0.06 | 0.1 | 0.23 | 0.19 |
| **Total** | 98.58 | 99.89 | 97.78 | 97.49 | 98.8 | 98.22 | 99.3 |
| Si | 7.923 | 8.005 | 9.72 | 9.712 | 9.848 | 9.819 | 9.917 |
| Al | 8.042 | 7.952 | 6.259 | 6.232 | 6.099 | 6.13 | 6.035 |
| Ti | 0 | 0.008 | 0 | 0.022 | 0.008 | 0 | 0 |
| $Fe_2$ | 0.008 | 0.014 | 0.022 | 0.019 | 0.044 | 0.012 | 0.03 |
| Mn | 0 | 0.002 | 0.005 | 0 | 0 | 0.014 | 0 |
| Mg | 0.003 | 0 | 0.014 | 0.006 | 0.011 | 0 | 0.019 |
| Ca | 4.037 | 3.989 | 2.29 | 2.331 | 2.164 | 2.211 | 2.113 |
| Na | 0.062 | 0.058 | 1.638 | 1.622 | 1.794 | 1.789 | 1.839 |
| K | 0.002 | 0 | 0.024 | 0.014 | 0.023 | 0.054 | 0.044 |
| Cations | 20.077 | 20.028 | 19.972 | 19.958 | 19.991 | 20.029 | 19.997 |
| End member calculation | | | | | | | |
| Ab | 1.5 | 1.4 | 41.4 | 40.9 | 45.1 | 44.1 | 46 |
| An | 98.4 | 98.6 | 57.9 | 58.8 | 54.4 | 54.5 | 52.9 |
| Or | 0 | 0 | 0.6 | 0.4 | 0.6 | 1.3 | 1.1 |

| Sample | 41 | 41 | 41 | 41 | 41 | 41 | 46 |
|---|---|---|---|---|---|---|---|
| Analysis | 30/1 | 31/1 | 41/1 | 42/1 | 8\1 | 9\1 | 44/1 |
| Location | Rim | Core | Core | Core | Core | Core | Core |
| $SiO_2$ | 52.56 | 53.46 | 52.51 | 51.29 | 50.8 | 52.83 | 54.67 |
| $TiO_2$ | 0.16 | 0.02 | 0.03 | 0.23 | 0.1 | 0.06 | 0.02 |
| $Al_2O_3$ | 27.38 | 27.62 | 27.54 | 28.68 | 29.75 | 28.67 | 27.33 |
| FeO | 0.1 | 0.13 | 0.18 | 0.15 | 0.3 | 0.04 | 0.28 |
| MnO | 0 | 0 | 0 | 0 | 0 | 0.01 | 0 |
| MgO | 0 | 0.02 | 0 | 0 | 0.01 | 0.03 | 0.28 |
| CaO | 10.87 | 10.52 | 11.14 | 12.06 | 13.01 | 11.83 | 10.19 |
| $Na_2O$ | 4.95 | 5.06 | 4.71 | 4.32 | 3.9 | 4.6 | 5.28 |
| $K_2O$ | 0.08 | 0.07 | 0.08 | 0.06 | 0.11 | 0.14 | 0.05 |
| **Total** | 96.1 | 96.9 | 96.19 | 96.79 | 97.98 | 98.21 | 98.1 |
| Si | 9.873 | 9.937 | 9.857 | 9.603 | 9.429 | 9.729 | 10.03 |
| Al | 6.057 | 6.046 | 6.088 | 6.324 | 6.503 | 6.218 | 5.905 |
| Ti | 0.023 | 0.003 | 0.004 | 0.032 | 0.014 | 0.008 | 0.003 |
| $Fe_2$ | 0.016 | 0.02 | 0.028 | 0.023 | 0.047 | 0.006 | 0.043 |
| Mn | 0 | 0 | 0 | 0 | 0 | 0.002 | 0 |
| Mg | 0 | 0.006 | 0 | 0 | 0.003 | 0.008 | 0.077 |
| Ca | 2.188 | 2.095 | 2.241 | 2.419 | 2.587 | 2.334 | 2.003 |
| Na | 1.803 | 1.824 | 1.714 | 1.568 | 1.404 | 1.643 | 1.878 |
| K | 0.019 | 0.017 | 0.019 | 0.014 | 0.026 | 0.033 | 0.012 |
| Cations | 19.979 | 19.948 | 19.951 | 19.983 | 20.013 | 19.981 | 19.951 |
| End member calculation | | | | | | | |
| Ab | 45 | 46.3 | 43.1 | 39.2 | 35 | 41 | 48.2 |
| An | 54.6 | 53.2 | 56.4 | 60.5 | 64.4 | 58.2 | 51.5 |
| Or | 0.5 | 0.4 | 0.5 | 0.3 | 0.6 | 0.8 | 0.3 |

Table 2. *(Continued.)*

| Sample | 46 | 46 | 46 | 46 | 46 | 46 | 46 |
|---|---|---|---|---|---|---|---|
| Analysis | 45/1 | 48/1 | 51/1 | 58/1 | 61/1 | 65/1 | 70/1 |
| Location | Core | Core | Core | Core | Core | Core | Core |
| $SiO_2$ | 54.8 | 54.18 | 54.62 | 54.45 | 54.9 | 55.88 | 57.11 |
| $TiO_2$ | 0 | 0 | 0.05 | 0 | 0 | 0.04 | 0.15 |
| $Al_2O_3$ | 26.7 | 27.33 | 27.62 | 27.26 | 27.3 | 26.92 | 25.93 |
| FeO | 0.08 | 0.05 | 0.1 | 0.02 | 0.12 | 0.13 | 0.04 |
| MnO | 0.06 | 0 | 0.02 | 0 | 0 | 0 | 0 |
| MgO | 0.04 | 0.02 | 0 | 0 | 0.02 | 0.01 | 0 |
| CaO | 9.2 | 10.04 | 10.28 | 10.14 | 9.95 | 9.49 | 8.06 |
| $Na_2O$ | 5.67 | 5.14 | 5.25 | 5.4 | 5.37 | 5.67 | 6.45 |
| $K_2O$ | 0.03 | 0.06 | 0.11 | 0.14 | 0.06 | 0.1 | 0.15 |
| **Total** | 96.58 | 96.82 | 98.05 | 97.41 | 97.72 | 98.24 | 97.89 |
| Si | 10.174 | 10.049 | 10.02 | 10.054 | 10.09 | 10.202 | 10.424 |
| Al | 5.838 | 5.969 | 5.967 | 5.928 | 5.909 | 5.788 | 5.574 |
| Ti | 0 | 0 | 0.007 | 0 | 0 | 0.005 | 0.021 |
| $Fe_2$ | 0.012 | 0.008 | 0.015 | 0.003 | 0.018 | 0.02 | 0.006 |
| Mn | 0.009 | 0 | 0.003 | 0 | 0 | 0 | 0 |
| Mg | 0.011 | 0.006 | 0 | 0 | 0.005 | 0.003 | 0 |
| Ca | 1.83 | 1.995 | 2.021 | 2.006 | 1.959 | 1.856 | 1.576 |
| Na | 2.041 | 1.848 | 1.868 | 1.933 | 1.914 | 2.007 | 2.283 |
| K | 0.007 | 0.014 | 0.026 | 0.033 | 0.014 | 0.023 | 0.035 |
| Cations | 19.922 | 19.889 | 19.927 | 19.957 | 19.909 | 19.904 | 19.919 |
| End member calculation | | | | | | | |
| Ab | 52.6 | 47.9 | 47.7 | 48.7 | 49.2 | 51.6 | 58.6 |
| An | 47.2 | 51.7 | 51.6 | 50.5 | 50.4 | 47.8 | 40.5 |
| Or | 0.2 | 0.4 | 0.7 | 0.8 | 0.4 | 0.6 | 0.9 |

| Sample | 46 | 46 | 46 | 47b | 47b | 47b | 47b |
|---|---|---|---|---|---|---|---|
| Analysis | 75/1 | 77/1 | 82/1 | 34/1 | 35/1 | 45/1 | 46/1 |
| Location | Core | Core | Core | Core | Rim | Rim | Core |
| $SiO_2$ | 55.62 | 55.76 | 55.94 | 55.06 | 58.4 | 56.77 | 53.3 |
| $TiO_2$ | 0.02 | 0 | 0 | 0.18 | 0 | 0 | 0.14 |
| $Al_2O_3$ | 27.41 | 28.06 | 27.07 | 27.44 | 25.6 | 25.76 | 28.67 |
| FeO | 0.28 | 0.24 | 0.13 | 0 | 0.13 | 0.18 | 0 |
| MnO | 0 | 0 | 0 | 0 | 0.02 | 0.03 | 0 |
| MgO | 0 | 0 | 0.01 | 0 | 0.02 | 0 | 0.01 |
| CaO | 9.66 | 10.07 | 9.73 | 9.9 | 7.52 | 8.15 | 11.03 |
| $Na_2O$ | 5.84 | 5.54 | 5.8 | 5.74 | 6.74 | 6.39 | 4.86 |
| $K_2O$ | 0.06 | 0.08 | 0.1 | 0.09 | 0.07 | 0.07 | 0.04 |
| **Total** | 98.89 | 99.75 | 98.78 | 98.41 | 98.5 | 97.35 | 98.05 |
| Si | 10.111 | 10.05 | 10.172 | 10.06 | 10.567 | 10.426 | 9.798 |
| Al | 5.868 | 5.956 | 5.797 | 5.904 | 5.455 | 5.572 | 6.207 |
| Ti | 0.003 | 0 | 0 | 0.025 | 0 | 0 | 0.019 |
| $Fe_2$ | 0.043 | 0.036 | 0.02 | 0 | 0.02 | 0.028 | 0 |
| Mn | 0 | 0 | 0 | 0 | 0.003 | 0.005 | 0 |
| Mg | 0 | 0 | 0.003 | 0 | 0.005 | 0 | 0.003 |
| Ca | 1.882 | 1.945 | 1.896 | 1.938 | 1.458 | 1.604 | 2.172 |
| Na | 2.059 | 1.936 | 2.045 | 2.034 | 2.365 | 2.276 | 1.732 |
| K | 0.014 | 0.018 | 0.023 | 0.021 | 0.016 | 0.016 | 0.009 |
| Cations | 19.98 | 19.941 | 19.956 | 19.982 | 19.889 | 19.927 | 19.94 |
| End member calculation | | | | | | | |
| Ab | 52.1 | 49.7 | 51.6 | 50.9 | 61.6 | 58.4 | 44.3 |
| An | 47.6 | 49.9 | 47.8 | 48.5 | 38 | 41.2 | 55.5 |
| Or | 0.4 | 0.5 | 0.6 | 0.5 | 0.4 | 0.4 | 0.2 |

Table 2. *(Continued.)*

| Sample | 47b | 47b | H2 | H2 | H2 |
|---|---|---|---|---|---|
| Analysis | 52/1 | 54/1 | 105/1 | 107/1 | 110/1 |
| Location | Core | Core | Core | Core | Core |
| $SiO_2$ | 57.87 | 58.51 | 58.59 | 56.17 | 59.42 |
| $TiO_2$ | 0.01 | 0.21 | 0 | 0 | 0.03 |
| $Al_2O_3$ | 25.71 | 25.58 | 26.53 | 26.43 | 26.05 |
| FeO | 0.05 | 0.11 | 0.19 | 0.42 | 0.03 |
| MnO | 0 | 0.01 | 0 | 0 | 0 |
| MgO | 0.01 | 0.01 | 0 | 0.24 | 0.03 |
| CaO | 7.72 | 7.6 | 7.79 | 8.62 | 7.46 |
| $Na_2O$ | 6.67 | 6.7 | 6.82 | 5.76 | 7.2 |
| $K_2O$ | 0.2 | 0.11 | 0.09 | 0.08 | 0.09 |
| **Total** | 98.24 | 98.84 | 100.01 | 97.72 | 100.31 |
| Si | 10.513 | 10.555 | 10.459 | 10.291 | 10.556 |
| Al | 5.501 | 5.434 | 5.577 | 5.703 | 5.45 |
| Ti | 0.001 | 0.028 | 0 | 0 | 0.004 |
| $Fe_2$ | 0.008 | 0.017 | 0.028 | 0.064 | 0.004 |
| Mn | 0 | 0.002 | 0 | 0 | 0 |
| Mg | 0.003 | 0.003 | 0 | 0.066 | 0.008 |
| Ca | 1.503 | 1.469 | 1.49 | 1.692 | 1.42 |
| Na | 2.35 | 2.344 | 2.361 | 2.046 | 2.48 |
| K | 0.046 | 0.025 | 0.02 | 0.019 | 0.02 |
| Cations | 19.925 | 19.877 | 19.935 | 19.881 | 19.972 |
| End member calculation | | | | | |
| Ab | 60.3 | 61.1 | 61 | 54.5 | 63.3 |
| An | 38.5 | 38.3 | 38.5 | 45 | 36.2 |
| Or | 1.2 | 0.7 | 0.5 | 0.5 | 0.5 |

plagioclase-bearing hornblende pyroxenite (1.2–1.58 wt%) than that in plagioclase bearing pyroxenite (0.86–1.12 wt%), whereas in metanorite, it has a wide range (0.02–2.21 wt%). The $TiO_2$ content is low in orthopyroxene in all the rock types. The composition of orthopyroxene shows similarity with those from the Vestfold lamprophyres (figure 6a).

### 5.4 *Amphiboles*

Representative chemical analyses of amphiboles from plagioclase-bearing pyroxenite, websterite and plagioclase-bearing hornblende pyroxenite and olivine metanorite are given in table 5. According to the IMA classification scheme (Leake 1997), all the analyzed amphiboles are calcic in composition. The amphiboles from plagioclase-bearing pyroxenite, websterite, metanorite and plagioclase bearing hornblende pyroxenite have high CaO content (11.47–12.21 wt%) with $Ca_B > 1.5$ pfu (table 5) and are classified as members of calcic amphibole group. Four samples of amphiboles from plagioclase-bearing pyroxenite are classified as magnesio-hornblende group (figure 7a) with $(Na + K)_A < 0.5$ and 2 samples as edenitic hornblende (figure 7b) with $(Na + K)_A > 0.5$. Five samples of websterite, plagioclase-bearing hornblende pyroxenite and metanorite are classified as pargasitic hornblende to pargasite (figure 7b) with $(Na + K)_A > 0.5$ and $Fe^{3+} <$ Al. Only one sample from websterite falls within the magnesio-hastingsite group, which is common in the shoshonitic lamprophyres. In comparison with the lamproitic amphiboles after Rock (1991), these amphiboles have low $SiO_2$ and $TiO_2$ contents, which are characteristics of the shoshonitic lamprophyres worldwide.

The amphiboles of plagioclase-bearing pyroxenite, websterite and plagioclase bearing hornblende pyroxenite are of primary origin as they are rich in $TiO_2$ (1.54–1.88, 1.06–1.56 and 0.96–1.52 wt%, respectively) and contain >0.1 Ti pfu (cf. Girardeau and Mevel 1982), while those of olivine metanorite are of secondary origin which are formed by the replacement of pyroxene and have low $TiO_2$ (0.61 wt%). In addition to this, the plots

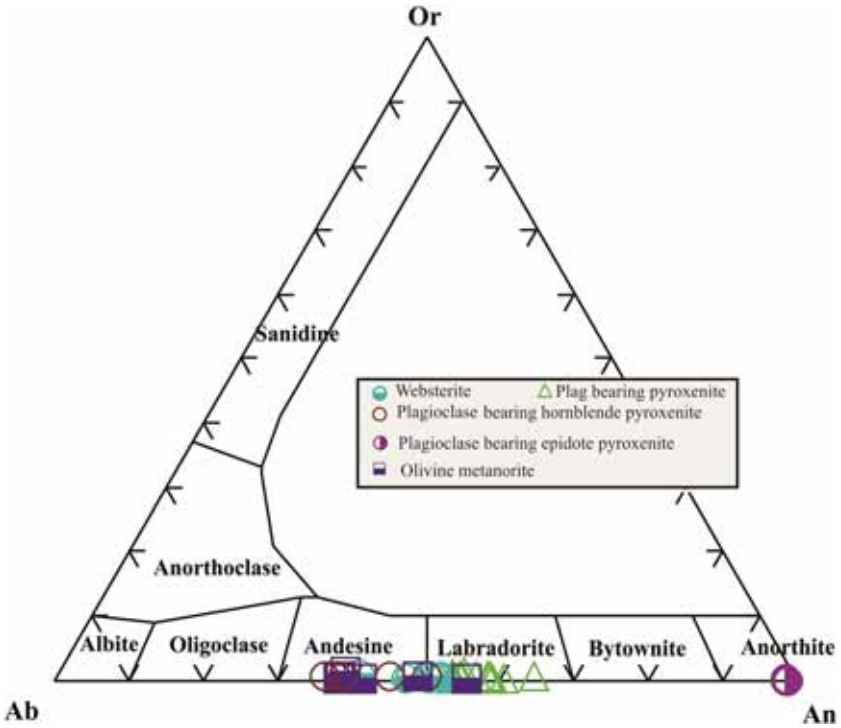


Figure 5. Feldspars from the mafic–ultramafic rocks of Purulia plotted on the ternary classification diagram of Deer *et al.* (1992). Ab = albite, An = anorthite, Or = orthoclase.

of the amphibole composition in $SiO_2$ *vs.* $TiO_2$ discrimination diagram (after Rock 1991) confirm that they are of primary rather than secondary phase (figure 7c). Primary amphiboles in the plagioclase-bearing pyroxenite and websterite are represented by edenitic hornblende and pargasitic hornblende, respectively, while primary amphiboles in the plagioclase-bearing hornblende pyroxenite are represented by pargasite. Secondary amphiboles in olivine metanorite are also represented by pargasite.

Positive correlation between Mg# and Cr (pfu) of amphiboles in plagioclase-bearing pyroxenite and websterite is consistent with their crystallization from a fractionating magma (figure not shown). When they are plotted in the $Al_2O_3$ *vs.* $TiO_2$ binary diagram (after Molina *et al.* 2009) the samples straddle between the sub-alkaline and sub-alkaline–alkaline domains (figure 7d).

### 5.5 *Biotite*

The EPMA data of biotites from mafic–ultramafic rocks are shown in table 6. The biotites in plagioclase-bearing hornblende pyroxenite are characterized by higher $TiO_2$ component (5.54 wt%) than those from websterite (3.37 wt%), metanorite (2.88 wt%) and plagioclase-bearing hornblende pyroxenite (3.05 wt%). The relatively high $TiO_2$ content in biotite suggests high temperature formation. The $Al_2O_3$ content of biotite ranges between 13.21 and 16.11 wt%. $Al_2O_3$ and $TiO_2$ contents of biotite of the present study are comparable to those in worldwide shoshonitic lamprophyre. In the Al–Mg–Fe (per formula unit) triangular diagram the biotites of the mafic–ultramafic rocks of present study are plotted in the shoshonitic lamprophyre field (figure 8a). In the $Al^{iv}$ *vs.* Fe/(Fe+Mg) (mole %) diagram the biotites of phlogopitic composition plot within the durbachite/vaugnerite field (figure 8b). In Mg (pfu) *vs.* Fe (pfu) diagram (after Pivec *et al.* 2002) the samples are plotted within or near the field of the lamprophyres (figure 8c). The biotites of the present study plot in the field of experimentally determined composition of magmatic biotite (under high oxygen fugacity condition; between NNO and NNO + 2.6) of the mafic durbachite in the Mg-number *vs.* $TiO_2$ diagram (figure 8d after Parat *et al.* 2010).

### 5.6 *Olivine*

Fresh olivine crystals analyzed from the olivine metanorite (table 7) are of restricted compositional

Table 3. *Representative analyses of clinopyroxenes from mafic and ultramafic intrusives and cationic calculation on the basis of 6 oxygen.*

| Sample | 28 | 28 | 28 | 28 | 28 | 41 | 41 |
|---|---|---|---|---|---|---|---|
| Analysis | 79/1 | 80/1 | 82/1 | 83/1 | 85/1 | 18/1 | 24/1 |
| Location | Core | Core | Core | Core | Core | Core | Core |
| $SiO_2$ | 50.01 | 50.88 | 50.41 | 49.5 | 50.41 | 51.6 | 51.32 |
| $TiO_2$ | 0.54 | 0.21 | 0.28 | 0.24 | 0.12 | 0.19 | 0.27 |
| $Al_2O_3$ | 1.88 | 1.42 | 2.06 | 2 | 1.54 | 1.71 | 1.69 |
| FeO | 12.46 | 12.63 | 12.74 | 12.67 | 12.75 | 5.63 | 6.13 |
| $Cr_2O_3$ | 0 | 0.14 | 0.15 | 0.25 | 0.05 | 0.13 | 0.21 |
| MnO | 0.31 | 0.23 | 0.21 | 0.25 | 0.21 | 0.09 | 0.18 |
| MgO | 10.07 | 10.56 | 9.7 | 9.71 | 10.45 | 14.88 | 14.86 |
| CaO | 24.09 | 23.83 | 23.73 | 23.48 | 23.94 | 23.11 | 22.36 |
| $Na_2O$ | 0.04 | 0.07 | 0.06 | 0.09 | 0.03 | 0.35 | 0.42 |
| $K_2O$ | 0 | 0 | 0 | 0.02 | 0 | 0.03 | 0 |
| **Total** | 99.4 | 99.97 | 99.34 | 98.21 | 99.5 | 97.72 | 97.44 |
| TSi | 1.92 | 1.939 | 1.939 | 1.925 | 1.93 | 1.942 | 1.939 |
| TAl | 0.08 | 0.061 | 0.061 | 0.075 | 0.069 | 0.058 | 0.061 |
| $TFe^{3+}$ | 0 | 0 | 0 | 0 | 0.001 | 0 | 0 |
| M1Al | 0.005 | 0.002 | 0.032 | 0.016 | 0 | 0.017 | 0.014 |
| M1Ti | 0.016 | 0.006 | 0.008 | 0.007 | 0.003 | 0.005 | 0.008 |
| $M1Fe^{3+}$ | 0.048 | 0.048 | 0.012 | 0.045 | 0.064 | 0.053 | 0.056 |
| M1Fe2 | 0.352 | 0.34 | 0.387 | 0.361 | 0.335 | 0.086 | 0.079 |
| M1Cr | 0 | 0.004 | 0.005 | 0.008 | 0.002 | 0.004 | 0.006 |
| M1Mg | 0.576 | 0.6 | 0.556 | 0.563 | 0.596 | 0.835 | 0.837 |
| M2Mg | 0 | 0 | 0 | 0 | 0 | 0 | 0 |
| $M2Fe^{2+}$ | 0 | 0.015 | 0.011 | 0.006 | 0.009 | 0.038 | 0.058 |
| M2Mn | 0.01 | 0.007 | 0.007 | 0.008 | 0.007 | 0.003 | 0.006 |
| M2Ca | 0.991 | 0.973 | 0.978 | 0.978 | 0.982 | 0.932 | 0.905 |
| M2Na | 0.003 | 0.005 | 0.004 | 0.007 | 0.002 | 0.026 | 0.031 |
| M2K | 0 | 0 | 0 | 0.001 | 0 | 0.001 | 0 |
| **Total** | 4 | 4 | 4 | 3.999 | 4 | 3.999 | 4 |
| End member calculation | | | | | | | |
| WO | 50.112 | 49.07 | 50.13 | 49.875 | 49.261 | 47.867 | 46.619 |
| EN | 29.146 | 30.256 | 28.512 | 28.698 | 29.919 | 42.883 | 43.108 |
| FS | 20.741 | 20.674 | 21.358 | 21.427 | 20.82 | 9.25 | 10.273 |
| WEF | 99.692 | 99.468 | 99.54 | 99.297 | 99.77 | 97.373 | 96.839 |
| JD | 0.027 | 0.023 | 0.332 | 0.187 | 0 | 0.647 | 0.628 |
| AE | 0.281 | 0.508 | 0.128 | 0.516 | 0.23 | 1.98 | 2.533 |
| Mg# | 62.92 | 63.71 | 61.52 | 61.67 | 63.25 | 84.73 | 83.58 |

| Sample | 41 | 41 | 41 | 41 | 41 | 46 | 46 |
|---|---|---|---|---|---|---|---|
| Analysis | 26/1 | 33/1 | 3\1 | 4\1 | 5\1 | 52/1 | 66/1 |
| Location | Rim | Core | Core | Core | Core | Core | Core |
| $SiO_2$ | 51.15 | 52.78 | 52.88 | 51.94 | 51.96 | 51.02 | 52.41 |
| $TiO_2$ | 0.18 | 0.27 | 0.23 | 0.09 | 0 | 0.17 | 0.24 |
| $Al_2O_3$ | 1.74 | 1.52 | 1.36 | 1.34 | 1.24 | 3.16 | 2.08 |
| FeO | 5.78 | 5.53 | 5 | 5.2 | 5.22 | 5.76 | 5.82 |
| $Cr_2O_3$ | 0.07 | 0.2 | 0.1 | 0.12 | 0.17 | 0.32 | 0 |
| MnO | 0.16 | 0.19 | 0.12 | 0.13 | 0.11 | 0.16 | 0.14 |
| MgO | 14.12 | 15.42 | 15.45 | 15.03 | 15.45 | 14.51 | 15.09 |
| CaO | 22.16 | 23.02 | 23.58 | 23.61 | 23.16 | 22.15 | 22.47 |
| $Na_2O$ | 0.37 | 0.34 | 0.38 | 0.41 | 0.37 | 0.61 | 0.49 |
| $K_2O$ | 0.03 | 0 | 0 | 0.01 | 0 | 0 | 0.03 |
| **Total** | 95.76 | 99.27 | 99.1 | 97.88 | 97.68 | 97.86 | 98.77 |

Table 3. *(Continued.)*

| Sample | 41 | 41 | 41 | 41 | 41 | 46 | 46 |
|---|---|---|---|---|---|---|---|
| Analysis | 26/1 | 33/1 | 3\1 | 4\1 | 5\1 | 52/1 | 66/1 |
| Location | Rim | Core | Core | Core | Core | Core | Core |
| TSi | 1.969 | 1.954 | 1.958 | 1.948 | 1.95 | 1.914 | 1.949 |
| TAl | 0.031 | 0.046 | 0.042 | 0.052 | 0.05 | 0.086 | 0.051 |
| TFe3 | 0 | 0 | 0 | 0 | 0 | 0 | 0 |
| M1Al | 0.048 | 0.021 | 0.017 | 0.007 | 0.005 | 0.054 | 0.04 |
| M1Ti | 0.005 | 0.008 | 0.006 | 0.003 | 0 | 0.005 | 0.007 |
| M1Fe3 | 0 | 0.028 | 0.037 | 0.066 | 0.067 | 0.057 | 0.035 |
| M1Fe2 | 0.134 | 0.086 | 0.084 | 0.08 | 0.059 | 0.063 | 0.082 |
| M1Cr | 0.002 | 0.006 | 0.003 | 0.004 | 0.005 | 0.009 | 0 |
| M1Mg | 0.81 | 0.851 | 0.853 | 0.84 | 0.864 | 0.812 | 0.836 |
| M2Mg | 0 | 0 | 0 | 0 | 0 | 0 | 0 |
| M2Fe2 | 0.052 | 0.056 | 0.034 | 0.017 | 0.038 | 0.06 | 0.064 |
| M2Mn | 0.005 | 0.006 | 0.004 | 0.004 | 0.003 | 0.005 | 0.004 |
| M2Ca | 0.914 | 0.913 | 0.935 | 0.949 | 0.931 | 0.89 | 0.895 |
| M2Na | 0.028 | 0.024 | 0.027 | 0.03 | 0.027 | 0.044 | 0.035 |
| M2K | 0.001 | 0 | 0 | 0 | 0 | 0 | 0.001 |
| **Total** | 3.999 | 4 | 4 | 4 | 4 | 4 | 3.999 |
| End member calculation | | | | | | | |
| WO | 47.713 | 47.035 | 48.049 | 48.496 | 47.441 | 47.166 | 46.696 |
| EN | 42.301 | 43.838 | 43.805 | 42.956 | 44.035 | 42.991 | 43.633 |
| FS | 9.986 | 9.126 | 8.146 | 8.548 | 8.524 | 9.843 | 9.671 |
| WEF | 97.197 | 97.512 | 97.223 | 96.942 | 97.239 | 95.376 | 96.382 |
| JD | 2.803 | 1.046 | 0.873 | 0.302 | 0.191 | 2.241 | 1.928 |
| AE | 0 | 1.443 | 1.904 | 2.757 | 2.571 | 2.383 | 1.69 |
| Mg# | 83.68 | 85.41 | 86.64 | 85.85 | 86.14 | 84.10 | 84.48 |

| Sample | 46 | 46 | 46 | 46 | 47b | 47b | 47b |
|---|---|---|---|---|---|---|---|
| Analysis | 69/1 | 71/1 | 72/1 | 78/1 | 49/1 | 50/1 | 51/1 |
| Location | Core | Core | Core | Core | Rim | Core | Core |
| $SiO_2$ | 51.15 | 52.43 | 49.06 | 51.41 | 53.14 | 53.38 | 55.06 |
| $TiO_2$ | 0 | 0.7 | 0.84 | 0.47 | 0.08 | 0 | 0.12 |
| $Al_2O_3$ | 3.01 | 2.3 | 6.05 | 3.09 | 2.16 | 2.18 | 1.4 |
| FeO | 6.09 | 5.97 | 7.63 | 6 | 4.53 | 4.39 | 13.8 |
| $Cr_2O_3$ | 0.36 | 0.7 | 0.52 | 0.42 | 0.41 | 0.44 | 0.17 |
| MnO | 0.06 | 0.19 | 0.08 | 0.14 | 0.17 | 0.08 | 0.27 |
| MgO | 14.29 | 14.29 | 14.52 | 14.29 | 15.72 | 15.57 | 28.88 |
| CaO | 22.43 | 21.99 | 17.33 | 22.17 | 22.15 | 22.4 | 0.36 |
| $Na_2O$ | 0.57 | 0.5 | 1.21 | 0.66 | 0.73 | 0.73 | 0.01 |
| $K_2O$ | 0 | 0.01 | 0.12 | 0 | 0.01 | 0 | 0.04 |
| **Total** | 97.96 | 99.08 | 97.36 | 98.65 | 99.1 | 99.17 | 100.11 |
| TSi | 1.92 | 1.956 | 1.845 | 1.918 | 1.957 | 1.965 | 1.963 |
| TAl | 0.08 | 0.044 | 0.155 | 0.082 | 0.043 | 0.035 | 0.037 |
| TFe3 | 0 | 0 | 0 | 0 | 0 | 0 | 0 |
| M1Al | 0.053 | 0.057 | 0.112 | 0.054 | 0.051 | 0.06 | 0.021 |
| M1Ti | 0 | 0.02 | 0.024 | 0.013 | 0.002 | 0 | 0.003 |
| M1Fe3 | 0.057 | 0 | 0.073 | 0.036 | 0.028 | 0.014 | 0.007 |
| M1Fe2 | 0.079 | 0.108 | 0 | 0.089 | 0.044 | 0.059 | 0 |
| M1Cr | 0.011 | 0.021 | 0.015 | 0.012 | 0.012 | 0.013 | 0.005 |
| M1Mg | 0.8 | 0.795 | 0.775 | 0.795 | 0.863 | 0.854 | 0.964 |
| M2Mg | 0 | 0 | 0.039 | 0 | 0 | 0 | 0.571 |
| M2Fe2 | 0.055 | 0.078 | 0.167 | 0.062 | 0.068 | 0.062 | 0.404 |
| M2Mn | 0.002 | 0.006 | 0.003 | 0.004 | 0.005 | 0.002 | 0.008 |

Table 3. *(Continued.)*

| Sample | 46 | 46 | 46 | 46 | 47b | 47b | 47b |
|---|---|---|---|---|---|---|---|
| Analysis | 69/1 | 71/1 | 72/1 | 78/1 | 49/1 | 50/1 | 51/1 |
| Location | Core | Core | Core | Core | Rim | Core | Core |
| M2Ca | 0.902 | 0.879 | 0.698 | 0.886 | 0.874 | 0.883 | 0.014 |
| M2Na | 0.041 | 0.036 | 0.088 | 0.048 | 0.052 | 0.052 | 0.001 |
| M2K | 0 | 0 | 0.006 | 0 | 0 | 0 | 0.002 |
| **Total** | 4 | 4 | 3.994 | 4 | 4 | 4 | 3.998 |
| End member calculation | | | | | | | |
| WO | 47.608 | 47.105 | 39.792 | 47.324 | 46.443 | 47.105 | 0.699 |
| EN | 42.202 | 42.591 | 46.388 | 42.442 | 45.861 | 45.557 | 77.983 |
| FS | 10.19 | 10.304 | 13.82 | 10.233 | 7.696 | 7.339 | 21.318 |
| WEF | 95.679 | 96.268 | 90.503 | 95.057 | 94.677 | 94.697 | 99.93 |
| JD | 2.076 | 3.732 | 5.752 | 2.95 | 3.459 | 4.267 | 0.053 |
| AE | 2.245 | 0 | 3.745 | 1.994 | 1.864 | 1.036 | 0.017 |
| Mg# | 83.13 | 83.40 | 79.98 | 83.33 | 87.93 | 88.16 | 81.46 |

| Sample | 47b | 47b | 47b | H2 | H2 | H2 |
|---|---|---|---|---|---|---|
| Analysis | 53/1 | 55/1 | 56/1 | 27/1 | 31/1 | 32/1 |
| Location | Core | Core | Core | Core | Core | Core |
| $SiO_2$ | 53.85 | 54.69 | 53.02 | 53.3 | 52.07 | 52.07 |
| $TiO_2$ | 0.08 | 0.01 | 0 | 0.16 | 0.44 | 0.32 |
| $Al_2O_3$ | 2.19 | 1.56 | 2.19 | 2.17 | 3.41 | 3.16 |
| FeO | 4.41 | 13.88 | 4.54 | 10.43 | 5.47 | 5.61 |
| $Cr_2O_3$ | 0.18 | 0 | 0.17 | | | |
| MnO | 0.15 | 0.17 | 0.14 | 0.27 | 0.11 | 0.2 |
| MgO | 15.86 | 28.34 | 15.75 | 21.08 | 14.76 | 15.31 |
| CaO | 22.6 | 0.37 | 22.64 | 11.54 | 22.9 | 22.55 |
| $Na_2O$ | 0.69 | 0 | 0.63 | 0.51 | 0.85 | 0.91 |
| $K_2O$ | 0 | 0 | 0.04 | 0 | 0 | 0 |
| **Total** | 100.01 | 99.02 | 99.12 | 99.46 | 100.01 | 100.13 |
| TSi | 1.965 | 1.972 | 1.952 | 1.943 | 1.906 | 1.9 |
| TAl | 0.035 | 0.028 | 0.048 | 0.057 | 0.094 | 0.1 |
| TFe3 | 0 | 0 | 0 | 0 | 0 | 0 |
| M1Al | 0.059 | 0.038 | 0.047 | 0.037 | 0.053 | 0.035 |
| M1Ti | 0.002 | 0 | 0 | 0.004 | 0.012 | 0.009 |
| M1Fe3 | 0.016 | 0 | 0.043 | 0.047 | 0.077 | 0.111 |
| M1Fe2 | 0.056 | 0 | 0.041 | 0 | 0.053 | 0.012 |
| M1Cr | 0.005 | 0 | 0.005 | 0 | 0 | 0 |
| M1Mg | 0.863 | 0.961 | 0.864 | 0.912 | 0.805 | 0.833 |
| M2Mg | 0 | 0.562 | 0 | 0.234 | 0 | 0 |
| M2Fe2 | 0.063 | 0.419 | 0.056 | 0.271 | 0.038 | 0.048 |
| M2Mn | 0.005 | 0.005 | 0.004 | 0.008 | 0.003 | 0.006 |
| M2Ca | 0.883 | 0.014 | 0.893 | 0.451 | 0.898 | 0.881 |
| M2Na | 0.049 | 0 | 0.045 | 0.036 | 0.06 | 0.064 |
| M2K | 0 | 0 | 0.002 | 0 | 0 | 0 |
| **Total** | 4 | 4 | 3.998 | 4 | 4 | 4 |
| End member calculation | | | | | | |
| WO | 46.86 | 0.729 | 46.962 | 23.443 | 47.914 | 46.601 |
| EN | 45.756 | 77.667 | 45.457 | 59.585 | 42.97 | 44.023 |
| FS | 7.383 | 21.604 | 7.58 | 16.972 | 9.115 | 9.376 |
| WEF | 95.037 | 100 | 95.384 | 96.298 | 93.711 | 93.255 |
| JD | 3.915 | 0 | 2.404 | 1.618 | 2.576 | 1.627 |
| AE | 1.048 | 0 | 2.213 | 2.083 | 3.714 | 5.118 |
| Mg# | 88.31 | 81.09 | 87.93 | 80.93 | 85.00 | 85.14 |

range (37.90–39.91 $SiO_2$ wt%). Forsterite components of these olivines ($Fo_{75–76}$) are much lower than those of the primary olivines from Zabargad peridotites ($Fo_{90.5–87.3}$). Forsterite component of olivine from ultramafic cumulate rocks is also low ($Fo_{72.03}$) (table 7; sample AD 443C).

### 5.7 *Spinel*

Chemical analyses of spinel from olivine metanorite are given in table 8. Spinels are represented by Al–Cr–Mg–spinel and Cr–magnetite. In table 8, the Al–Cr–Mg-rich spinel has a very restricted $Al_2O_3$ (40.03–44.56 wt%), $Cr_2O_3$ (24.62–25.73 wt%) and MgO (7.78–9.07 wt%). Groundmass spinels are slightly $Cr_2O_3$-rich than the spinels occurring as inclusion within olivine. Spinel inclusions within olivine, on the other hand, are slightly enriched in Al, Mg and $Fe^{3+}$ than the groundmass spinels. On the whole a restricted range of $Fe^{3+}/Fe^{2+}$ (0.10–0.15) and Cr# (Cr/Cr+Al, 0.20–0.26) ratios are revealed in spinels.

High $Fe^{3+}$ concentrations in spinels are characteristics of mafic/ultramafic rocks of subduction zone environment (e.g., Alaskan-type complex) (e.g.,

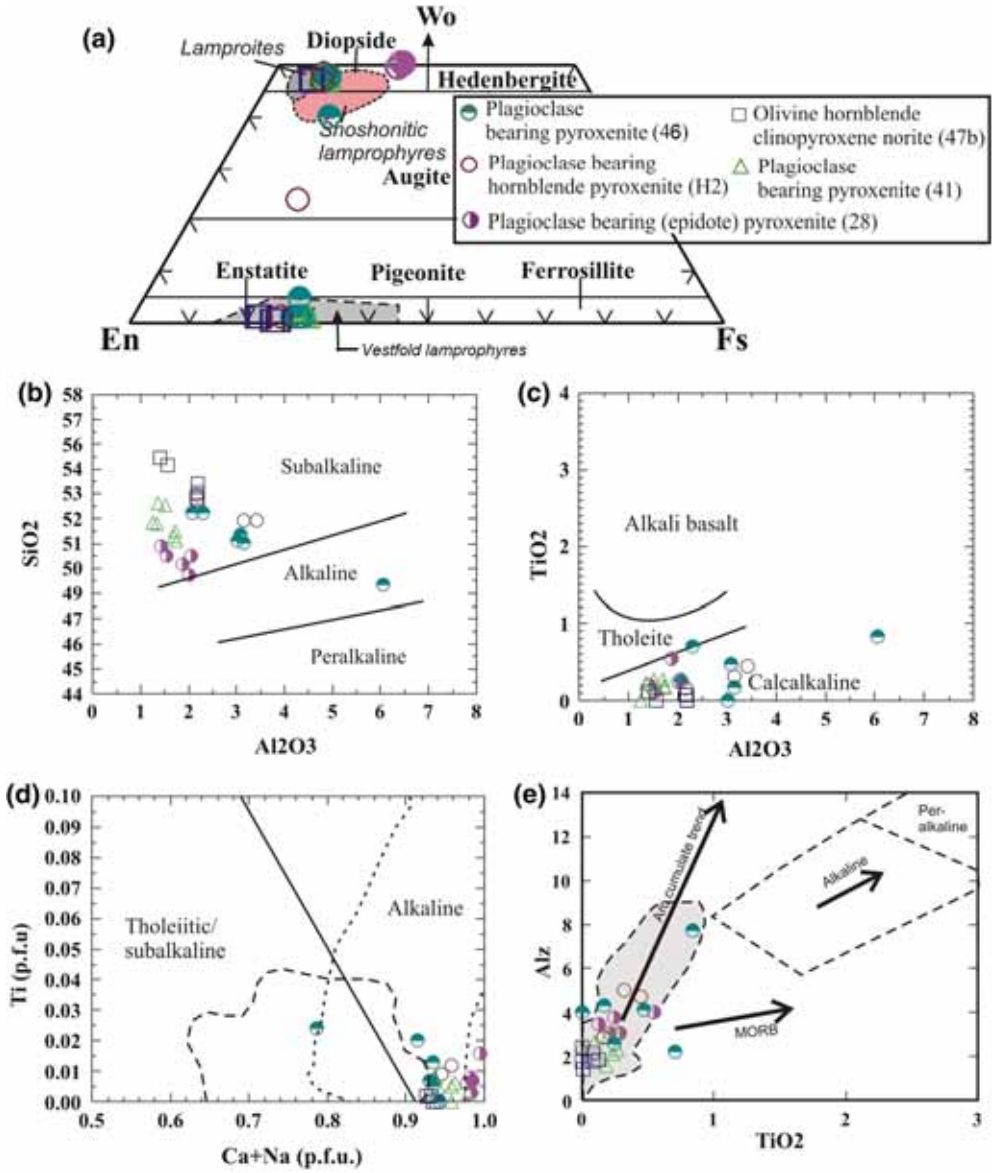


Figure 6. Pyroxene composition from present study area plotted in the (**a**) pyroxene quadrilateral (after Morimoto 1988; fields of lamproites and shoshonitic lamprophyre are from Rock 1991). Compositions of clinopyroxenes are also plotted in the chemical discrimination diagrams of various authors. (**b**) and (**c**) after Le Bas (1962). (**d**) after Letterrier *et al.* (1982). (**e**) after Le Bas (1962) and modified after Loucks (1990). Alz = percentage of tetrahedral sites occupied by Al. Major oxides are given in weight (%).

Table 4. *Representative analyses of orthopyroxenes from mafic and ultramafic intrusives and cationic calculation on the basis of 6 oxygen.*

| Sample | 41 | 41 | 41 | 41 | 41 | 41 | 41 | 41 | 41 |
|---|---|---|---|---|---|---|---|---|---|
| Analysis | 12\1 | 13/1 | 14/1 | 25/1 | 27/1 | 36/1 | 37/1 | 6\1 | 7\1 |
| Location | Rim | Core | Core | Core | Rim | Core | Core | Core | Core |
| $SiO_2$ | 51.96 | 52.8 | 53.59 | 52.91 | 53.61 | 52.29 | 52.86 | 53.6 | 53.73 |
| $TiO_2$ | 0.14 | 0 | 0 | 0.13 | 0.09 | 0.19 | 0.05 | 0.16 | 0.15 |
| $Al_2O_3$ | 1.12 | 1 | 0.97 | 0.89 | 0.86 | 0.96 | 0.97 | 0.91 | 0.95 |
| FeO | 18.64 | 17.69 | 17.9 | 18.88 | 18.5 | 18.45 | 18.2 | 18.15 | 18.27 |
| $Cr_2O_3$ | 0.07 | 0.1 | 0 | 0.05 | 0.02 | 0.11 | 0.1 | 0.09 | 0.1 |
| MnO | 0.34 | 0.41 | 0.39 | 0.41 | 0.31 | 0.32 | 0.27 | 0.43 | 0.33 |
| MgO | 25.24 | 25.53 | 26.18 | 25.03 | 26.07 | 25.68 | 25.41 | 26.01 | 26.05 |
| CaO | 0.35 | 0.36 | 0.29 | 0.27 | 0.25 | 0.25 | 0.27 | 0.32 | 0.25 |
| $Na_2O$ | 0.03 | 0.02 | 0.02 | 0 | 0 | 0 | 0 | 0 | 0.02 |
| $K_2O$ | 0 | 0.01 | 0 | 0 | 0.02 | 0.05 | 0.01 | 0.01 | 0.03 |
| **Total** | 97.89 | 97.92 | 99.34 | 98.57 | 99.73 | 98.3 | 98.14 | 99.68 | 99.88 |
| TSi | 1.936 | 1.961 | 1.959 | 1.963 | 1.957 | 1.937 | 1.962 | 1.957 | 1.958 |
| TAl | 0.049 | 0.039 | 0.041 | 0.037 | 0.037 | 0.042 | 0.038 | 0.039 | 0.041 |
| $TFe^{3+}$ | 0.015 | 0 | 0 | 0 | 0.006 | 0.021 | 0 | 0.004 | 0.001 |
| M1Al | 0 | 0.005 | 0.001 | 0.002 | 0 | 0 | 0.005 | 0 | 0 |
| M1Ti | 0.004 | 0 | 0 | 0.004 | 0.002 | 0.005 | 0.001 | 0.004 | 0.004 |
| $M1Fe^{3+}$ | 0.056 | 0.033 | 0.041 | 0.027 | 0.039 | 0.051 | 0.028 | 0.032 | 0.034 |
| M1Fe2 | 0 | 0 | 0 | 0 | 0 | 0 | 0 | 0 | 0 |
| M1Cr | 0.002 | 0.003 | 0 | 0.001 | 0.001 | 0.003 | 0.003 | 0.003 | 0.003 |
| M1Mg | 0.938 | 0.959 | 0.958 | 0.966 | 0.958 | 0.94 | 0.963 | 0.961 | 0.959 |
| M2Mg | 0.464 | 0.454 | 0.469 | 0.418 | 0.46 | 0.478 | 0.443 | 0.455 | 0.456 |
| $M2Fe^{2+}$ | 0.509 | 0.517 | 0.506 | 0.559 | 0.52 | 0.5 | 0.537 | 0.519 | 0.521 |
| M2Mn | 0.011 | 0.013 | 0.012 | 0.013 | 0.01 | 0.01 | 0.008 | 0.013 | 0.01 |
| M2Ca | 0.014 | 0.014 | 0.011 | 0.011 | 0.01 | 0.01 | 0.011 | 0.013 | 0.01 |
| M2Na | 0.002 | 0.001 | 0.001 | 0 | 0 | 0 | 0 | 0 | 0.001 |
| M2K | 0 | 0 | 0 | 0 | 0.001 | 0.002 | 0 | 0 | 0.001 |
| **Total** | 4 | 4 | 4 | 4 | 3.999 | 3.998 | 4 | 4 | 3.999 |
| End member calculation | | | | | | | | | |
| WO | 0.696 | 0.72 | 0.569 | 0.538 | 0.488 | 0.494 | 0.54 | 0.627 | 0.49 |
| EN | 69.837 | 71.024 | 71.429 | 69.434 | 70.835 | 70.566 | 70.647 | 70.937 | 71.046 |
| FS | 29.467 | 28.256 | 28.002 | 30.027 | 28.677 | 28.941 | 28.813 | 28.435 | 28.464 |
| WEF | 99.777 | 99.853 | 99.855 | 100 | 100 | 100 | 100 | 100 | 99.856 |
| JD | 0 | 0.019 | 0.003 | 0 | 0 | 0 | 0 | 0 | 0 |
| AE | 0.223 | 0.128 | 0.141 | 0 | 0 | 0 | 0 | 0 | 0.144 |
| Mg# | 73.96 | 75.16 | 75.41 | 73.55 | 74.72 | 74.48 | 74.54 | 75.03 | 74.94 |

| Sample | 46 | 46 | 46 | 46 | 46 | 46 | 47b | 47b | H2 | H2 | H2 |
|---|---|---|---|---|---|---|---|---|---|---|---|
| Analysis | 43/1 | 49/1 | 55/1 | 60/1 | 62/1 | 67/1 | 36/1 | 37/1 | 28/1 | 29/1 | 30/1 |
| Location | Core | Core | Core | Core | Core | Core | Core | Core | Core | Core | Core |
| $SiO_2$ | 52.78 | 53.45 | 53.51 | 53.39 | 53.36 | 53.47 | 54.84 | 54.85 | 53.39 | 53.94 | 54.43 |
| $TiO_2$ | 0 | 0.05 | 0.27 | 0.03 | 0.02 | 0 | 0 | 0.07 | 0 | 0 | 0.03 |
| $Al_2O_3$ | 1.8 | 1.9 | 1.54 | 1.72 | 1.43 | 1.68 | 2.21 | 1.92 | 1.58 | 1.2 | 1.42 |
| FeO | 17.45 | 17.06 | 18.2 | 18.37 | 17.84 | 18.11 | 14.4 | 14.05 | 16.59 | 16.59 | 16.63 |
| $Cr_2O_3$ | 0.01 | 0.2 | 0 | 0.01 | 0.04 | 0 | 0.12 | 0.22 | | | |
| MnO | 0.36 | 0.39 | 0.37 | 0.35 | 0.35 | 0.42 | 0.34 | 0.32 | 0.16 | 0.35 | 0.35 |
| MgO | 25.6 | 26.07 | 25.96 | 25.41 | 25.85 | 25.91 | 29.24 | 28.95 | 27.4 | 27.92 | 27.59 |
| CaO | 2.2 | 0.39 | 0.36 | 0.29 | 0.35 | 0.28 | 0.27 | 0.35 | 0.4 | 0.37 | 0.35 |
| $Na_2O$ | 0.03 | 0.02 | 0 | 0 | 0.03 | 0.02 | 0 | 0.01 | 0.03 | 0.02 | 0.06 |
| $K_2O$ | 0 | 0.03 | 0 | 0.02 | 0 | 0 | 0 | 0.03 | 0.01 | 0.01 | 0.01 |
| **Total** | 100.23 | 99.56 | 100.21 | 99.59 | 99.27 | 99.89 | 101.42 | 100.77 | 99.56 | 100.4 | 100.87 |

Table 4. *(Continued.)*

| Sample | 46 | 46 | 46 | 46 | 46 | 46 | 47b | 47b | H2 | H2 | H2 |
|---|---|---|---|---|---|---|---|---|---|---|---|
| Analysis | 43/1 | 49/1 | 55/1 | 60/1 | 62/1 | 67/1 | 36/1 | 37/1 | 28/1 | 29/1 | 30/1 |
| Location | Core | Core | Core | Core | Core | Core | Core | Core | Core | Core | Core |
| TSi | 1.913 | 1.946 | 1.943 | 1.953 | 1.953 | 1.946 | 1.928 | 1.942 | 1.931 | 1.933 | 1.945 |
| TAl | 0.077 | 0.054 | 0.057 | 0.047 | 0.047 | 0.054 | 0.072 | 0.058 | 0.067 | 0.051 | 0.055 |
| $TFe^{3+}$ | 0.011 | 0 | 0 | 0 | 0 | 0 | 0 | 0 | 0.002 | 0.016 | 0 |
| M1Al | 0 | 0.028 | 0.009 | 0.028 | 0.015 | 0.018 | 0.02 | 0.023 | 0 | 0 | 0.004 |
| M1Ti | 0 | 0.001 | 0.007 | 0.001 | 0.001 | 0 | 0 | 0.002 | 0 | 0 | 0.001 |
| $M1Fe^{3+}$ | 0.089 | 0.02 | 0.033 | 0.018 | 0.032 | 0.037 | 0.048 | 0.027 | 0.072 | 0.068 | 0.054 |
| M1Fe2 | 0 | 0 | 0 | 0 | 0 | 0 | 0 | 0 | 0 | 0 | 0 |
| M1Cr | 0 | 0.006 | 0 | 0 | 0.001 | 0 | 0.003 | 0.006 | 0 | 0 | 0 |
| M1Mg | 0.911 | 0.945 | 0.951 | 0.954 | 0.952 | 0.945 | 0.929 | 0.943 | 0.928 | 0.932 | 0.941 |
| M2Mg | 0.472 | 0.47 | 0.455 | 0.432 | 0.459 | 0.461 | 0.604 | 0.586 | 0.549 | 0.56 | 0.528 |
| $M2Fe^{2+}$ | 0.429 | 0.5 | 0.52 | 0.544 | 0.515 | 0.514 | 0.376 | 0.389 | 0.428 | 0.413 | 0.443 |
| M2Mn | 0.011 | 0.012 | 0.011 | 0.011 | 0.011 | 0.013 | 0.01 | 0.01 | 0.005 | 0.011 | 0.011 |
| M2Ca | 0.085 | 0.015 | 0.014 | 0.011 | 0.014 | 0.011 | 0.01 | 0.013 | 0.015 | 0.014 | 0.013 |
| M2Na | 0.002 | 0.001 | 0 | 0 | 0.002 | 0.001 | 0 | 0.001 | 0.002 | 0.001 | 0.004 |
| M2K | 0 | 0.001 | 0 | 0.001 | 0 | 0 | 0 | 0.001 | 0 | 0 | 0 |
| **Total** | 4 | 3.999 | 4 | 3.999 | 4 | 4 | 4 | 3.999 | 4 | 4 | 4 |
| End member calculation | | | | | | | | | | | |
| WO | 4.253 | 0.776 | 0.706 | 0.577 | 0.693 | 0.551 | 0.515 | 0.675 | 0.775 | 0.706 | 0.673 |
| EN | 68.864 | 72.132 | 70.854 | 70.344 | 71.196 | 70.968 | 77.549 | 77.686 | 73.884 | 74.075 | 73.83 |
| FS | 26.883 | 27.093 | 28.44 | 29.079 | 28.111 | 28.481 | 21.937 | 21.639 | 25.341 | 25.219 | 25.497 |
| WEF | 99.78 | 99.855 | 100 | 100 | 99.782 | 99.855 | 100 | 99.929 | 99.782 | 99.856 | 99.573 |
| JD | 0 | 0.085 | 0 | 0 | 0.07 | 0.047 | 0 | 0.032 | 0 | 0 | 0.032 |
| AE | 0.22 | 0.06 | 0 | 0 | 0.148 | 0.098 | 0 | 0.038 | 0.218 | 0.144 | 0.396 |
| Mg# | 75.47 | 76.22 | 74.95 | 74.36 | 75.24 | 75 | 80.98 | 81.21 | 77.6 | 77.92 | 77.67 |

| Sample | 47b | 47b | 47b | 47b | H2 | H2 | H2 |
|---|---|---|---|---|---|---|---|
| Analysis | 39/1 | 41/1 | 42/1 | 57/1 | 28/1 | 29/1 | 30/1 |
| Location | Core | Core | Core | Core | Core | Core | Core |
| $SiO_2$ | 39.91 | 38.68 | 39.36 | 38.25 | 53.39 | 53.94 | 54.43 |
| $TiO_2$ | 0 | 0.02 | 0.07 | 0 | 0 | 0 | 0.03 |
| $Al_2O_3$ | 0 | 0 | 0.02 | 0 | 1.58 | 1.2 | 1.42 |
| FeO | 22.63 | 23.17 | 22.33 | 23.11 | 16.59 | 16.59 | 16.63 |
| $Cr_2O_3$ | 0 | 0 | 0.08 | 0.03 | | | |
| MnO | 0.21 | 0.29 | 0.25 | 0.28 | 0.16 | 0.35 | 0.35 |
| MgO | 39.46 | 39.06 | 39.94 | 39.4 | 27.4 | 27.92 | 27.59 |
| CaO | 0.02 | 0 | 0.04 | 0.03 | 0.4 | 0.37 | 0.35 |
| $Na_2O$ | 0 | 0.03 | 0 | 0.01 | 0.03 | 0.02 | 0.06 |
| $K_2O$ | 0 | 0.02 | 0.02 | 0 | 0.01 | 0.01 | 0.01 |
| **Total** | 102.23 | 101.27 | 102.11 | 101.11 | 99.56 | 100.4 | 100.87 |
| TSi | 1.354 | 1.327 | 1.334 | 1.312 | 1.931 | 1.933 | 1.945 |
| TAl | 0 | 0 | 0.001 | 0 | 0.067 | 0.051 | 0.055 |
| $TFe^{3+}$ | 0 | 0 | 0 | 0 | 0.002 | 0.016 | 0 |
| M1Al | 0 | 0 | 0 | 0 | 0 | 0 | 0.004 |
| M1Ti | 0 | 0.001 | 0.002 | 0 | 0 | 0 | 0.001 |
| $M1Fe^{3+}$ | 0 | 0 | 0 | 0 | 0.072 | 0.068 | 0.054 |
| M1Fe2 | 0 | 0 | 0 | 0 | 0 | 0 | 0 |
| M1Cr | 0 | 0 | 0.002 | 0.001 | 0 | 0 | 0 |
| M1Mg | 1 | 0.999 | 0.996 | 0.999 | 0.928 | 0.932 | 0.941 |
| M2Mg | 0.996 | 0.998 | 1.022 | 1.015 | 0.549 | 0.56 | 0.528 |
| $M2Fe^{2+}$ | 0.642 | 0.665 | 0.633 | 0.663 | 0.428 | 0.413 | 0.443 |
| M2Mn | 0.006 | 0.008 | 0.007 | 0.008 | 0.005 | 0.011 | 0.011 |
| M2Ca | 0.001 | 0 | 0.001 | 0.001 | 0.015 | 0.014 | 0.013 |

Table 4. *(Continued.)*

| Sample | 47b | 47b | 47b | 47b | H2 | H2 | H2 |
|---|---|---|---|---|---|---|---|
| Analysis | 39/1 | 41/1 | 42/1 | 57/1 | 28/1 | 29/1 | 30/1 |
| Location | Core | Core | Core | Core | Core | Core | Core |
| M2Na | 0 | 0.002 | 0 | 0.001 | 0.002 | 0.001 | 0.004 |
| M2K | 0 | 0.001 | 0.001 | 0 | 0 | 0 | 0 |
| **Total** | 4 | 3.999 | 3.999 | 4 | 4 | 4 | 4 |
| End member calculation | | | | | | | |
| WO | 0.027 | 0 | 0.055 | 0.041 | 0.775 | 0.706 | 0.673 |
| EN | 75.466 | 74.795 | 75.877 | 74.983 | 73.884 | 74.075 | 73.83 |
| FS | 24.507 | 25.205 | 24.068 | 24.976 | 25.341 | 25.219 | 25.497 |
| WEF | 100 | 99.851 | 100 | 99.951 | 99.782 | 99.856 | 99.573 |
| JD | 0 | 0 | 0 | 0 | 0 | 0 | 0.032 |
| AE | 0 | 0.003 | 0.001 | 0.001 | 0.218 | 0.144 | 0.396 |
| Mg# | 78.53 | 77.95 | 78.95 | 78.14 | 77.60 | 77.92 | 77.67 |

Nixon *et al.* 1990) while low $Fe^{3+}$ concentrations are characteristics of ophiolites (Dick 1977) and layered mafic intrusions (Jackson 1963). Roeder (1994) suggested that high $Fe^{3+}$ content of spinel is either due to its reaction with intercumulus liquid or due to ion-exchange with olivine in sub-solidus stage.

Plots of spinels from olivine metanorite on the Mg# *vs.* Cr# and Mg# *vs.* $Fe^{3+}$# are shown in figure 9(a and b). On figure 9(a), spinel compositions lie outside the three fields, but three of the four plots lie close to the field of Alpine-type complexes. On figure 9(b), however, all the four plots lie very near the lower boundaries of the Alpine type complexes and Stratiform complexes.

Cr-magnetite contains about 9.59 wt% $Cr_2O_3$ whereas the $Al_2O_3$ (0.0 wt%) and MgO (0.07 wt%) contents are negligible. The MnO contents in both types of spinel are low.

## 6. Bulk-rock geochemistry

The major and trace element compositions for eight new representative samples from the Purulia mafic–ultramafic intrusions are listed in table 9 (sl. no. 1 to 8). These samples show wide compositional variation in both major and trace elements from norite, hornblendite and pyroxenite. In the TAS diagram, the samples of mafic and ultramafic rocks plot in the fields of basalt, basaltic andesite and andesite (figure 10a). These rocks show enrichment of both incompatible and compatible trace elements. For example, they show enrichments of $K_2O$ (0.18–2.6 wt%) and Ba + Sr (133–2750 ppm) together with high $FeO_t$ + MgO (9.74–30.26 wt%) and high Cr (93–1648 ppm) and Ni (34–735 ppm) concentrations (table 9). In the MgO *vs.* $K_2O$ diagram after Ferré and Leake (2001) most of the samples (except one melaolivine hornblende clinopyroxene norite and one plagioclase pyroxenite) plot within the high-K field (figure 10b). The hornblende and biotite bearing mafic and ultramafic rocks of present study are petrographically similar to the appinite, kentallenite, durbachite, vaugnerite, redwizite, etc. So we plot these samples in the $k$ ($100K_2O/(K_2O + Na_2O)$) *vs.* *mg* ($100 * MgO/(MgO + FeO_t)$) diagram proposed by Rock (1991) which can chemically classify the rocks of appinite, kentallenite, vaugnerite, durbachite and redwizite series. The mafic–ultramafic rocks of present study principally plot within the kentallenite field while one sample plots in the redwizite field (figure 10c). In the AFM diagram (figure 10d), the samples of present study plot in the field of arc-related ultramafic and mafic cumulates.

The N-MORB normalized trace element patterns (normalization values after Sun and McDonough 1989) the rocks of present study show enrichment in large ion lithophile elements relative to high field strength elements with distinct positive Pb anomaly and negative Nb and Ti anomalies (figure 10e), as seen in the post-collisional mafic–ultramafic rocks of lamprophyre, appinite, vaugnerite and durbachite affinity (cf. Scarrow *et al.* 2009). The chondrite-normalized REE diagrams (normalization values after Sun and McDonough 1989) for the gabbro-norite and the olivine hornblende pyroxenite are given in figure 10(f). The gabbro-norite and olivine hornblende pyroxenite show essentially parallel REE patterns (figure 10f) with total REE varying

Table 5. *Representative analyses of amphiboles from mafic and ultramafic intrusives and cationic calculation on the basis of 23 oxygen.*

| Sample | 41 | 41 | 41 | 41 | 41 | 41 | 46 | 46 |
|---|---|---|---|---|---|---|---|---|
| Analysis | 15/1 | 19/1 | 1\1 | 2\1 | 32/1 | 38/1 | 46/1 | 50/1 |
| Location | Core | Core | Core | Rim | Core | Core | Core | Core |
| $SiO_2$ | 44.7 | 45.39 | 44.48 | 44.78 | 43.68 | 44.34 | 41.75 | 41.97 |
| $TiO_2$ | 1.68 | 1.76 | 1.84 | 1.76 | 1.88 | 1.54 | 1.41 | 1.06 |
| $Al_2O_3$ | 9.47 | 8.68 | 9.93 | 9.87 | 9.42 | 9.28 | 13.68 | 13.3 |
| FeO | 9.35 | 9.38 | 9.96 | 9.9 | 9.75 | 9.38 | 10.12 | 9.64 |
| $Cr_2O_3$ | 0.68 | 0.64 | 0.69 | 0.65 | 0.5 | 0.58 | 0.35 | 0.57 |
| MnO | 0.11 | 0.08 | 0.11 | 0 | 0.03 | 0.05 | 0.06 | 0.11 |
| MgO | 15.04 | 15.25 | 14.58 | 15.1 | 14.52 | 14.75 | 13.67 | 14.18 |
| CaO | 11.84 | 11.81 | 11.92 | 12.21 | 11.92 | 11.66 | 11.59 | 11.62 |
| $Na_2O$ | 1.14 | 1.34 | 1.34 | 1.4 | 1.36 | 1.36 | 2.07 | 2.01 |
| $K_2O$ | 1.12 | 0.89 | 1.15 | 1.11 | 1.1 | 1.12 | 1.21 | 1.35 |
| **Total** | 95.13 | 95.22 | 96 | 96.78 | 94.16 | 94.06 | 95.91 | 95.81 |
| TSi | 6.604 | 6.699 | 6.551 | 6.539 | 6.572 | 6.644 | 6.161 | 6.188 |
| TAl | 1.396 | 1.301 | 1.449 | 1.461 | 1.428 | 1.356 | 1.839 | 1.812 |
| Sum T | 8 | 8 | 8 | 8 | 8 | 8 | 8 | 8 |
| CAl | 0.252 | 0.207 | 0.274 | 0.236 | 0.241 | 0.281 | 0.539 | 0.497 |
| CCr | 0.079 | 0.075 | 0.08 | 0.075 | 0.059 | 0.069 | 0.041 | 0.066 |
| $CFe^{3+}$ | 0.404 | 0.343 | 0.326 | 0.34 | 0.252 | 0.306 | 0.461 | 0.514 |
| CTi | 0.187 | 0.195 | 0.204 | 0.193 | 0.213 | 0.174 | 0.157 | 0.118 |
| CMg | 3.313 | 3.355 | 3.201 | 3.287 | 3.257 | 3.295 | 3.007 | 3.117 |
| $CFe^{2+}$ | 0.751 | 0.815 | 0.901 | 0.869 | 0.975 | 0.869 | 0.788 | 0.675 |
| CMn | 0.014 | 0.01 | 0.014 | 0 | 0.004 | 0.006 | 0.007 | 0.014 |
| CCa | 0 | 0 | 0 | 0 | 0 | 0 | 0 | 0 |
| Sum C | 5 | 5 | 5 | 5 | 5 | 5 | 5 | 5 |
| BMg | 0 | 0 | 0 | 0 | 0 | 0 | 0 | 0 |
| $BFe^{2+}$ | 0 | 0 | 0 | 0 | 0 | 0 | 0 | 0 |
| BMn | 0 | 0 | 0 | 0 | 0 | 0 | 0 | 0 |
| BCa | 1.874 | 1.867 | 1.881 | 1.91 | 1.921 | 1.872 | 1.833 | 1.836 |
| BNa | 0.126 | 0.133 | 0.119 | 0.09 | 0.079 | 0.128 | 0.167 | 0.164 |
| Sum B | 2 | 2 | 2 | 2 | 2 | 2 | 2 | 2 |
| ACa | 0 | 0 | 0 | 0 | 0 | 0 | 0 | 0 |
| ANa | 0.201 | 0.251 | 0.264 | 0.307 | 0.318 | 0.267 | 0.425 | 0.41 |
| AK | 0.211 | 0.168 | 0.216 | 0.207 | 0.211 | 0.214 | 0.228 | 0.254 |
| Sum A | 0.412 | 0.418 | 0.48 | 0.513 | 0.529 | 0.481 | 0.653 | 0.664 |
| **Total** | 15.412 | 15.418 | 15.48 | 15.513 | 15.529 | 15.481 | 15.653 | 15.664 |

between 130.93 and 318.63 ppm. These rocks show enrichment in LREE relative to the HREE $[(La/Lu)_n = 14.72–25.44]$.

Field investigations show that the mafic–ultramafics of present study are largely unmetamorphosed. These occur as small rounded enclaves, small dykes/sills and also as dykes with apophyses within the porphyritic granitoid host. Goswami and Bhattacharyya (2014) inferred a post-collisional tectonic setting for the porphyritic granitoids with which the mafic–ultramafics are spatially and temporally associated. Tectonic setting of the mafic–ultramafic rocks of Purulia was investigated using the discrimination diagrams proposed by Müller and Groves (1997) (figure 10g and h). In the $Al_2O_3$ *vs.* $TiO_2$ diagram (figure 10g) of these authors the rocks of present study plot in the arc-related tectonic-setting whereas in the $TiO_2/Al_2O_3$ *vs.* $Zr/Al_2O_3$ diagram (figure 10h) most of the samples of the present study plot in the continental arc and post-collisional arc settings.

## 7. Physico-chemical conditions of crystallization

Temperature ($T$), pressure ($P$), and oxygen fugacity ($fO_2$) strongly influence the mineral compositions and crystallization history in magmatic systems. Therefore, evaluating intrinsic parameters of the

Table 5. *(Continued.)*

| Sample | 46 | 46 | 46 | 46 | 46 | 47b | H2 | H2 |
|---|---|---|---|---|---|---|---|---|
| Analysis | 56/1 | 59/1 | 73/1 | 79/1 | 80/1 | 40/1 | 35/1 | 36/1 |
| Location | Core | Core | Core | Core | Core | Core | Core | Rim |
| $SiO_2$ | 41.48 | 41.75 | 42.45 | 42.15 | 42.33 | 41.3 | 41.65 | 41.69 |
| $TiO_2$ | 1.36 | 1.34 | 1.35 | 1.29 | 1.56 | 0.61 | 0.96 | 1.52 |
| $Al_2O_3$ | 13.04 | 12.94 | 12.98 | 14.01 | 13.02 | 15.5 | 14.34 | 13.84 |
| FeO | 10.13 | 9.88 | 10.22 | 9.84 | 9.97 | 7.42 | 9.62 | 9.95 |
| $Cr_2O_3$ | 0.16 | 0.36 | 0.16 | 0.48 | 0.42 | 0.64 | 0 | 0 |
| MnO | 0.03 | 0.1 | 0 | 0.11 | 0.08 | 0.04 | 0.04 | 0.09 |
| MgO | 13.72 | 13.99 | 13.76 | 13.74 | 13.9 | 14.94 | 14.75 | 14.55 |
| CaO | 11.47 | 11.68 | 11.65 | 11.52 | 11.57 | 11.75 | 11.99 | 12.1 |
| $Na_2O$ | 2.17 | 2.12 | 2.05 | 2.21 | 2.11 | 2.66 | 2.75 | 2.76 |
| $K_2O$ | 1.41 | 1.35 | 1.32 | 1.37 | 1.38 | 1.18 | 1.04 | 1.07 |
| **Total** | 94.97 | 95.51 | 95.94 | 96.72 | 96.34 | 96.04 | 97.14 | 97.57 |
| TSi | 6.203 | 6.204 | 6.275 | 6.17 | 6.232 | 6.031 | 6.061 | 6.075 |
| TAl | 1.797 | 1.796 | 1.725 | 1.83 | 1.768 | 1.969 | 1.939 | 1.925 |
| Sum T | 8 | 8 | 8 | 8 | 8 | 8 | 8 | 8 |
| CAl | 0.499 | 0.468 | 0.535 | 0.586 | 0.49 | 0.696 | 0.519 | 0.449 |
| CCr | 0.019 | 0.042 | 0.019 | 0.055 | 0.049 | 0.074 | 0 | 0 |
| $CFe^{3+}$ | 0.4 | 0.4 | 0.343 | 0.408 | 0.371 | 0.416 | 0.501 | 0.386 |
| CTi | 0.153 | 0.15 | 0.15 | 0.142 | 0.173 | 0.067 | 0.105 | 0.167 |
| CMg | 3.058 | 3.099 | 3.032 | 2.999 | 3.051 | 3.252 | 3.2 | 3.16 |
| $CFe^{2+}$ | 0.867 | 0.828 | 0.92 | 0.797 | 0.856 | 0.49 | 0.67 | 0.826 |
| CMn | 0.004 | 0.013 | 0 | 0.014 | 0.01 | 0.005 | 0.005 | 0.011 |
| CCa | 0 | 0 | 0 | 0 | 0 | 0 | 0 | 0 |
| Sum C | 5 | 5 | 5 | 5 | 5 | 5 | 5 | 5 |
| BMg | 0 | 0 | 0 | 0 | 0 | 0 | 0 | 0 |
| $BFe^{2+}$ | 0 | 0 | 0 | 0 | 0 | 0 | 0 | 0 |
| BMn | 0 | 0 | 0 | 0 | 0 | 0 | 0 | 0 |
| BCa | 1.838 | 1.86 | 1.845 | 1.807 | 1.825 | 1.838 | 1.87 | 1.889 |
| BNa | 0.162 | 0.14 | 0.155 | 0.193 | 0.175 | 0.162 | 0.13 | 0.111 |
| Sum B | 2 | 2 | 2 | 2 | 2 | 2 | 2 | 2 |
| ACa | 0 | 0 | 0 | 0 | 0 | 0 | 0 | 0 |
| ANa | 0.467 | 0.47 | 0.433 | 0.434 | 0.428 | 0.591 | 0.646 | 0.669 |
| AK | 0.269 | 0.256 | 0.249 | 0.256 | 0.259 | 0.22 | 0.193 | 0.199 |
| Sum A | 0.736 | 0.726 | 0.682 | 0.69 | 0.687 | 0.811 | 0.839 | 0.868 |
| Sum_cat | 15.736 | 15.726 | 15.682 | 15.69 | 15.687 | 15.811 | 15.839 | 15.868 |

Note: $Fe^{2+}$, $Fe^{3+}$ estimation according to Leake (1997).

magmatic system, using mineral composition, is important to rebuild the magmatic history of the studied rocks. To estimate the intrinsic parameters of the magma using the mineral chemistry (i.e., clinopyroxene, orthopyroxene, olivine, plagioclase, hornblende, biotite and spinel), common thermo-barometers and oxybarometers proposed by various authors have been used. Such studies have already been carried out in vaugnerites and durbachites of Variscan belt of Europe. The vaugnerites of Corsica Batholith, France crystallized from mantle generated lamprophyric magmas that yield 675 ± 25°C solidus temperature (hornblende–plagioclase thermometry of Holland and Blundy 1994) for a maximum pressure of 3.5 ± 0.5 kbar (Al-in amphibole barometry) under $\log fO_2 \sim -16$ and $H_2O$ content around 3–4 wt%. The liquidus temperature of this magma is suggested to be >900°C (Ferré and Leake 2001). Biotites and amphiboles of durbachites of Bohemian massif are shown to be crystallized at around 650 and 750°C, respectively, while temperature of primary crystallization of opx–cpx pair yields 900–950°C (cf. Holub 1997). Application of two-pyroxene thermometry yields values 970–1040°C for phlogopite–pyroxenites, genetically related to durbachites of Bohemian massif (Trubac *et al.* 2015).

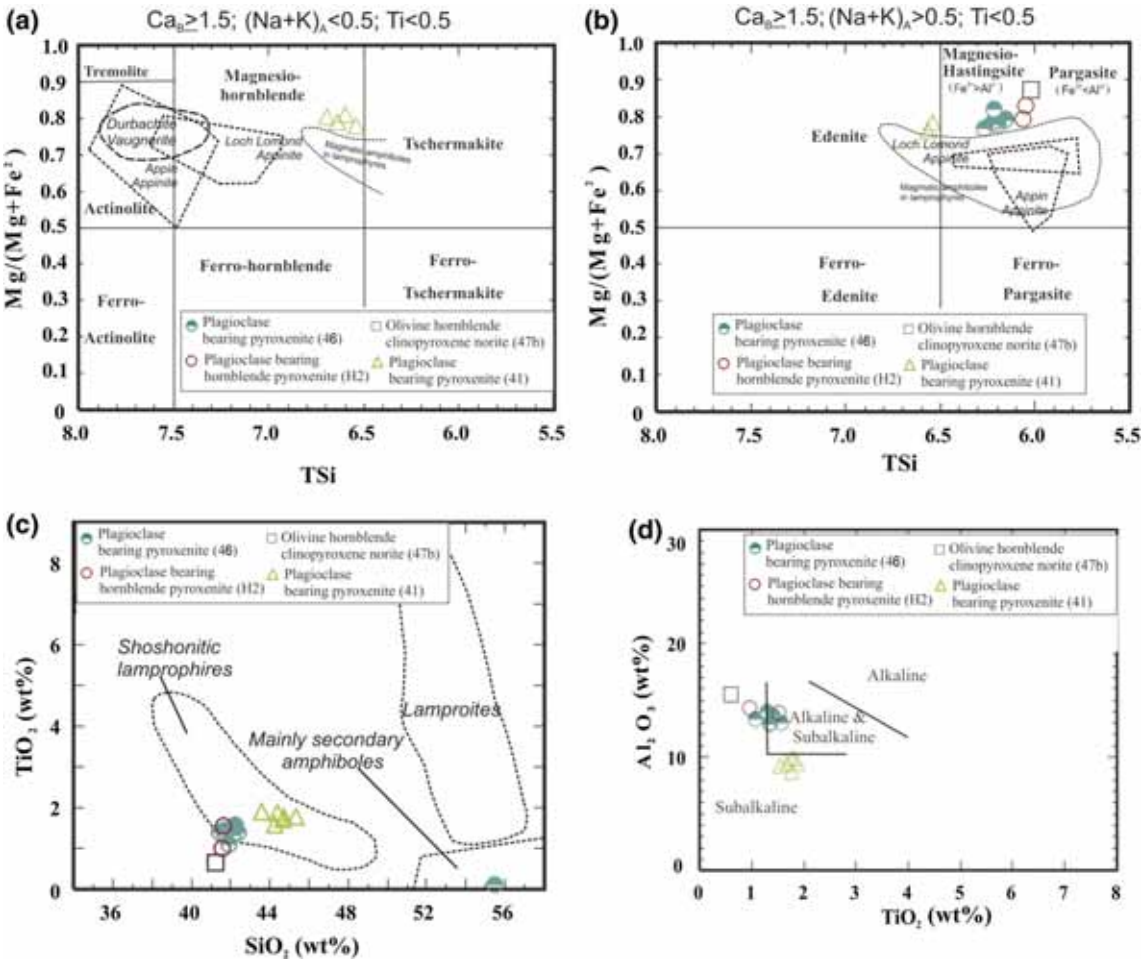


Figure 7. (**a** and **b**) Amphibole compositions from the mafic–ultramafic suite of Purulia plotted in fields of calcic amphiboles (after Leake *et al.* 1997). Field of amphiboles of Appin and Loch Lomond appinites are drawn from Hamidullah (2007) and field of durbachite–vaugnerite is drawn from Buda and Dobosi (2004). Plots of Ca-amphiboles of present study in (**c**) $SiO_2$ *vs.* $TiO_2$ (in wt%) diagram (after Rock 1991) and (**d**) $TiO_2$ *vs.* $Al_2O_3$ (in wt%) diagram (after Molina *et al.* 2009).

Experimental work of Montel and Weisbrod (1986) reveals that temperature of vaugneritic magmas was around 1000°C whereas their solidus temperature was at about 790°C, at $PH_2O = P_{tot} = 2$ kbar. More recent experimental studies on mafic durbachite of the Bohemian massif show that the temperature of magma was around 900–1000°C at 100–200 Ma pressure, at water saturated condition (1.1–6.1 $H_2O$ wt%) and oxidizing conditions (above Ni–NiO buffer) when olivine, phlogopite and augite were in co-crystallizing phases (Parat *et al.* 2010).

In the light of above findings, we summarize the results of our investigations on the intrinsic parameters of the parental magma of the mafic–ultramafic rocks of present study which will show that these parameters are closely similar to those of the vaugnerites and durbachites of Variscan belt.

### 7.1 *Geothermometry*

Results from applications of various geothermometers to the mafic–ultramafic rocks of Purulia are summarized in table 10.

Most of the ultramafic and mafic cumulates of Purulia contain touching clinopyroxene–orthopyroxene pairs allowing temperature calculations. Compositions of coexisting orthopyroxene and clinopyroxene pairs have been used for thermometric calibration assuming equilibrium prior to hornblende crystallization. Temperature obtained by two-pyroxene thermometers of Wood and Banno (1973) gives a range between 975–1088°C which is quite similar to the temperature range (985–1444°C) obtained from the application of two-pyroxene solvus thermometer of Taylor (1998). It is worthy of mention that liquidus temperature of vaugnerite magma was experimentally determined as ∼1000°C at 2 kbar pressure (Montel and Weisbrod 1986).

Table 6. *Representative analyses of biotite from mafic and ultramafic intrusives and cationic calculation on the basis of 22 oxygen.*

| Sample | 41 | 41 | 41 | 41 | 41 | 41 | 41 | 41 |
|---|---|---|---|---|---|---|---|---|
| Analysis | 11\1 | 22/1 | 23/1 | 28/1 | 29/1 | 34/1 | 35/1 | 39/1 |
| Location | Core | Core | Rim | Core | Core | Core | Core | Core |
| $SiO_2$ | 36.67 | 36.67 | 36.93 | 36.11 | 36.53 | 35.98 | 36.58 | 37.56 |
| $TiO_2$ | 5.33 | 5.55 | 5.41 | 5.88 | 5.52 | 5.41 | 5.25 | 5.27 |
| $Al_2O_3$ | 13.92 | 13.69 | 14.01 | 13.21 | 13.38 | 13.58 | 13.34 | 13.85 |
| $Cr_2O_3$ | 0.65 | 0.55 | 0.64 | 0.69 | 0.66 | 0.67 | 0.67 | 0.65 |
| FeO | 10.85 | 10.81 | 10.98 | 11.05 | 10.92 | 11.32 | 10.66 | 10.64 |
| MnO | 0 | 0 | 0 | 0.03 | 0 | 0.08 | 0.06 | 0.04 |
| MgO | 15.83 | 15.93 | 16.18 | 15.9 | 16.37 | 16.08 | 15.9 | 16.03 |
| BaO | n.d. | n.d. | n.d. | n.d. | n.d. | n.d. | n.d. | n.d. |
| CaO | 0.09 | 0.04 | 0.06 | 0.03 | 0.11 | 0.05 | 0.01 | 0 |
| $Na_2O$ | 0.07 | 0.11 | 0.14 | 0.08 | 0.18 | 0.11 | 0.07 | 0.07 |
| $K_2O$ | 10.17 | 9.75 | 9.89 | 9.28 | 9.31 | 9.55 | 9.74 | 9.54 |
| **Total** | 93.58 | 93.1 | 94.24 | 92.26 | 92.98 | 92.83 | 92.28 | 93.65 |
| Si | 5.774 | 5.788 | 5.765 | 5.758 | 5.772 | 5.72 | 5.826 | 5.865 |
| $Al^{IV}$ | 2.226 | 2.212 | 2.235 | 2.242 | 2.228 | 2.28 | 2.174 | 2.135 |
| $Al^{VI}$ | 0.355 | 0.333 | 0.34 | 0.239 | 0.262 | 0.263 | 0.328 | 0.412 |
| Ti | 0.631 | 0.659 | 0.635 | 0.705 | 0.656 | 0.647 | 0.629 | 0.619 |
| $Fe^{2+}$ | 1.429 | 1.427 | 1.433 | 1.474 | 1.443 | 1.505 | 1.42 | 1.389 |
| Cr | 0.081 | 0.069 | 0.079 | 0.087 | 0.082 | 0.084 | 0.084 | 0.08 |
| Mn | 0 | 0 | 0 | 0.004 | 0 | 0.011 | 0.008 | 0.005 |
| Mg | 3.716 | 3.749 | 3.765 | 3.78 | 3.856 | 3.811 | 3.775 | 3.732 |
| Ba | 0 | 0 | 0 | 0 | 0 | 0 | 0 | 0 |
| Ca | 0.015 | 0.007 | 0.01 | 0.005 | 0.019 | 0.009 | 0.002 | 0 |
| Na | 0.021 | 0.034 | 0.042 | 0.025 | 0.055 | 0.034 | 0.022 | 0.021 |
| K | 2.043 | 1.963 | 1.97 | 1.888 | 1.877 | 1.937 | 1.979 | 1.9 |
| **Total** | 16.291 | 16.241 | 16.274 | 16.207 | 16.25 | 16.301 | 16.247 | 16.158 |
| FeO/MgO | 0.69 | 0.68 | 0.68 | 0.69 | 0.67 | 0.70 | 0.67 | 0.66 |
| Fe/(Fe+Mg) | 0.28 | 0.28 | 0.28 | 0.28 | 0.27 | 0.28 | 0.27 | 0.27 |
| Mg/(Fe+Mg) | 0.72 | 0.72 | 0.72 | 0.72 | 0.73 | 0.72 | 0.73 | 0.73 |

| Sample | 41 | 46 | 46 | 46 | 46 | 46 | 46 | 46 |
|---|---|---|---|---|---|---|---|---|
| Analysis | 41/1 | 47/1 | 53/1 | 54/1 | 57/1 | 63/1 | 64/1 | 68/1 |
| Location | Core | Core | Core | Core | Core | Core | Core | Core |
| $SiO_2$ | 36.98 | 37.53 | 36.84 | 36.34 | 36.8 | 34.93 | 35.79 | 36.74 |
| $TiO_2$ | 6.27 | 3.17 | 3.68 | 3.42 | 3.17 | 3.26 | 3.49 | 3.37 |
| $Al_2O_3$ | 13.68 | 15.4 | 15.24 | 15.03 | 15.27 | 14.77 | 14.75 | 15.38 |
| $Cr_2O_3$ | 0.61 | 0.46 | 0.09 | 0.14 | 0.22 | 3.44 | 0.21 | 0.24 |
| FeO | 10.85 | 9.61 | 10.32 | 9.84 | 9.97 | 8.78 | 9.58 | 10.14 |
| MnO | 0 | 0.07 | 0 | 0 | 0.04 | 0 | 0.02 | 0.06 |
| MgO | 16.46 | 18.26 | 17.66 | 17.89 | 17.61 | 17.26 | 17.51 | 18.1 |
| BaO | n.d. | n.d. | n.d. | n.d. | n.d. | n.d. | n.d. | n.d. |
| CaO | 0.02 | 0.03 | 0 | 0.04 | 0 | 0.16 | 0 | 0 |
| $Na_2O$ | 0.07 | 0.22 | 0.22 | 0.28 | 0.29 | 0.32 | 0.28 | 0.26 |
| $K_2O$ | 9.35 | 9.4 | 9.4 | 9.61 | 9.53 | 9.16 | 9.38 | 9.6 |
| **Total** | 94.29 | 94.15 | 93.45 | 92.59 | 92.9 | 92.08 | 91.01 | 93.89 |
| Si | 5.748 | 5.787 | 5.747 | 5.728 | 5.773 | 5.565 | 0.174 | 5.713 |
| $Al^{IV}$ | 2.252 | 2.213 | 2.253 | 2.272 | 2.227 | 2.435 | 0.085 | 2.287 |
| $Al^{VI}$ | 0.252 | 0.583 | 0.547 | 0.518 | 0.594 | 0.336 | 0 | 0.529 |
| Ti | 0.733 | 0.368 | 0.432 | 0.406 | 0.374 | 0.391 | 11.163 | 0.394 |
| $Fe^{2+}$ | 1.41 | 1.239 | 1.346 | 1.297 | 1.308 | 1.17 | 0.039 | 1.319 |
| Cr | 0.075 | 0.056 | 0.011 | 0.017 | 0.027 | 0.433 | 0.001 | 0.029 |
| Mn | 0 | 0.009 | 0 | 0 | 0.005 | 0 | 0 | 0.008 |

Table 6. *(Continued.)*

| Sample | 41 | 46 | 46 | 46 | 46 | 46 | 46 | 46 |
|---|---|---|---|---|---|---|---|---|
| Analysis | 41/1 | 47/1 | 53/1 | 54/1 | 57/1 | 63/1 | 64/1 | 68/1 |
| Location | Core | Core | Core | Core | Core | Core | Core | Core |
| Mg | 3.814 | 4.197 | 4.107 | 4.204 | 4.118 | 4.1 | 0.127 | 4.196 |
| Ba | 0 | 0 | 0 | 0 | 0 | 0 | 0 | 0 |
| Ca | 0.003 | 0.005 | 0 | 0.007 | 0 | 0.027 | 0 | 0 |
| Na | 0.021 | 0.066 | 0.067 | 0.086 | 0.088 | 0.099 | 0.003 | 0.078 |
| K | 1.854 | 1.849 | 1.871 | 1.933 | 1.907 | 1.862 | 0.058 | 1.904 |
| Cations | 16.162 | 16.372 | 16.381 | 16.468 | 16.421 | 16.418 | 11.65 | 16.457 |
| FeO/MgO | 0.66 | 0.53 | 0.58 | 0.55 | 0.57 | 0.51 | 0.55 | 0.56 |
| Fe/(Fe+Mg) | 0.27 | 0.23 | 0.25 | 0.24 | 0.24 | 0.22 | 0.23 | 0.24 |
| Mg/(Fe+Mg) | 0.73 | 0.77 | 0.75 | 0.76 | 0.76 | 0.78 | 0.77 | 0.76 |
| Sample | 46 | 46 | 46 | 47b | 47b | 47b | 47b | 47b |
| Analysis | 74/1 | 76/1 | 81/1 | 32/1 | 33/1 | 43/1 | 44/1 | 60/1 |
| Location | Core | Core | Core | Core | Core | Rim | Core | Core |
| $SiO_2$ | 36.39 | 36.6 | 35.33 | 36.96 | 37.06 | 37.55 | 36.2 | 37.13 |
| $TiO_2$ | 3.51 | 3.63 | 3.17 | 3.06 | 4.05 | 2.84 | 2.52 | 2.32 |
| $Al_2O_3$ | 14.79 | 15.37 | 14.87 | 14.87 | 15.35 | 16.11 | 15.26 | 15.98 |
| $Cr_2O_3$ | 0.15 | 0.17 | 0.33 | 0.33 | 0.61 | 0.39 | 0.59 | 0.82 |
| FeO | 10.33 | 9.9 | 9.59 | 7.35 | 7.52 | 6.39 | 6.64 | 7.11 |
| MnO | 0.01 | 0.06 | 0.02 | 0.07 | 0.06 | 0.02 | 0 | 0 |
| MgO | 17.64 | 17.58 | 17.85 | 19.61 | 19.04 | 20.47 | 19.82 | 21.09 |
| BaO | n.d. | n.d. | n.d. | n.d. | n.d. | n.d. | n.d. | n.d. |
| CaO | 0.04 | 0 | 0.11 | 0.12 | 0.1 | 0.06 | 0.04 | 0.09 |
| $Na_2O$ | 0.35 | 0.27 | 0.32 | 0.47 | 0.47 | 0.51 | 0.48 | 0.47 |
| $K_2O$ | 9.5 | 9.6 | 9.26 | 8.81 | 8.94 | 9.64 | 9.45 | 8.87 |
| **Total** | 92.71 | 93.18 | 90.85 | 91.65 | 93.2 | 93.98 | 91 | 93.88 |
| Si | 5.741 | 5.728 | 5.679 | 5.789 | 5.718 | 5.723 | 5.722 | 5.671 |
| $Al^{IV}$ | 2.259 | 2.272 | 2.321 | 2.211 | 2.282 | 2.277 | 2.278 | 2.329 |
| $Al^{VI}$ | 0.489 | 0.561 | 0.494 | 0.532 | 0.507 | 0.615 | 0.563 | 0.546 |
| Ti | 0.417 | 0.427 | 0.383 | 0.36 | 0.47 | 0.326 | 0.3 | 0.267 |
| $Fe^{2+}$ | 1.363 | 1.296 | 1.289 | 0.963 | 0.97 | 0.814 | 0.878 | 0.908 |
| Cr | 0.019 | 0.021 | 0.042 | 0.041 | 0.074 | 0.047 | 0.074 | 0.099 |
| Mn | 0.001 | 0.008 | 0.003 | 0.009 | 0.008 | 0.003 | 0 | 0 |
| Mg | 4.149 | 4.102 | 4.277 | 4.579 | 4.379 | 4.651 | 4.67 | 4.802 |
| Ba | 0 | 0 | 0 | 0 | 0 | 0 | 0 | 0 |
| Ca | 0.007 | 0 | 0.019 | 0.02 | 0.017 | 0.01 | 0.007 | 0.015 |
| Na | 0.107 | 0.082 | 0.1 | 0.143 | 0.141 | 0.151 | 0.147 | 0.139 |
| K | 1.912 | 1.917 | 1.899 | 1.76 | 1.76 | 1.874 | 1.906 | 1.728 |
| Cations | 16.464 | 16.414 | 16.506 | 16.407 | 16.326 | 16.491 | 16.545 | 16.504 |
| FeO/MgO | 0.59 | 0.56 | 0.54 | 0.37 | 0.39 | 0.31 | 0.34 | 0.34 |
| Fe/(Fe+Mg) | 0.25 | 0.24 | 0.23 | 0.17 | 0.18 | 0.15 | 0.16 | 0.16 |
| Mg/(Fe+Mg) | 0.75 | 0.76 | 0.77 | 0.83 | 0.82 | 0.85 | 0.84 | 0.84 |

However, Ca-in-orthopyroxene thermometric formulation of Brey and Köhler (1990) gives a range of 775–836°C which is close to the temperature obtained by two-pyroxene thermometer of Wells (1977) that gives a range of temperature between 817–856°C. Thermometry using the concentrations of $Fe^{2+}$ and Mg in coexisting ortho- and clinopyroxene is a technique that has long been applied to mafic rocks due to the availability of thermodynamic and experimental data. However, a variety of datasets and calibrations have been used for this thermometer and as a result a wide range of temperature estimates can be obtained. The major demerit of this technique is that the results usually underestimate peak temperatures due to retrograde exchange of $Fe^{2+}$ and Mg (Frost and Chacko 1989). We interpret that the lower temperature range of crystallization obtained for

Table 6. *(Continued.)*

| Sample | 47b | H2 | H2 |
|---|---|---|---|
| Analysis | 61/1 | 33/1 | 34/1 |
| Location | Core | | |
| $SiO_2$ | 38.28 | 37.24 | 36.53 |
| $TiO_2$ | 2.51 | 3.06 | 2.95 |
| $Al_2O_3$ | 16 | 15.77 | 15.43 |
| $Cr_2O_3$ | 0.7 | n.d. | n.d. |
| FeO | 6.93 | 9.4 | 8.9 |
| MnO | 0.01 | 0.02 | 0 |
| MgO | 21.18 | 19.44 | 17.15 |
| BaO | n.d. | 0.42 | 0.71 |
| CaO | 0.12 | 0.08 | 0.1 |
| $Na_2O$ | 0.53 | 0.55 | 0.36 |
| $K_2O$ | 9.1 | 9.1 | 8.87 |
| **Total** | 95.36 | 95.08 | 91 |
| Si | 5.744 | 5.694 | 5.827 |
| $Al^{IV}$ | 2.256 | 2.306 | 2.173 |
| $Al^{VI}$ | 0.571 | 0.534 | 0.726 |
| Ti | 0.283 | 0.352 | 0.354 |
| $Fe^{2+}$ | 0.87 | 1.202 | 1.187 |
| Cr | 0.083 | 0 | 0 |
| Mn | 0.001 | 0.003 | 0 |
| Mg | 4.738 | 4.431 | 4.078 |
| Ba | 0 | 0.025 | 0.044 |
| Ca | 0.019 | 0.013 | 0.017 |
| Na | 0.154 | 0.163 | 0.111 |
| K | 1.742 | 1.775 | 1.805 |
| Cations | 16.461 | 16.498 | 16.322 |
| FeO/MgO | 0.33 | 0.48 | 0.52 |
| Fe/(Fe+Mg) | 0.16 | 0.21 | 0.23 |
| Mg/(Fe+Mg) | 0.84 | 0.79 | 0.77 |

mafic–ultramafic rocks of present study by several calibrations (e.g., Wells 1977; Kretz 1982; see table 10) actually represent blocking temperatures of the retrograde exchange reaction (Winter 2002).

Hornblende–plagioclase thermometers are critical to understanding the thermal evolution of the mafic–ultramafic suite. Blundy and Holland (1990) and Holland and Blundy (1994) published three different calibrations of the amphibole–plagioclase thermometers for different hornblende solid-solution models. The empirical thermometer of Blundy and Holland (1990) yielded unusually high temperatures for some lithologies. Later on, Holland and Blundy (1994) proposed two different amphibole–plagioclase thermometers based on albite + edenite = anorthite + richterite and quartz + edenite = albite + tremolite reactions for quartz-free and quartz-bearing rocks, respectively. Since no free-quartz is seen in the mafic–ultramafic suite of present study, we used the edenite–richterite thermometer to calculate the crystallization temperature which gives a narrow range from 781° to 818°C, which all lie above the wet granite solidus.

The Ti-content of biotite has been regarded as a relative measure of temperature of biotite crystallization (Engel and Engel 1960; Rutherford 1969). High $TiO_2$ content of biotite in mafic–ultramafic suite of Purulia implies its involvement in high temperature equilibration. The empirical correlation between temperature and Ti content and Mg# of biotite was established by many authors (Patiño Douce 1993; Henry *et al.* 2005). Ti-in-biotite thermometer of Henry *et al.* (2005) yields temperature range of 634–805°C for biotite crystallization of mafic–ultramafic rocks of present study, which is slightly lower than the equilibrium temperatures determined from coexisting hornblende–plagioclase pairs and consistent with their crystallization later to the amphiboles.

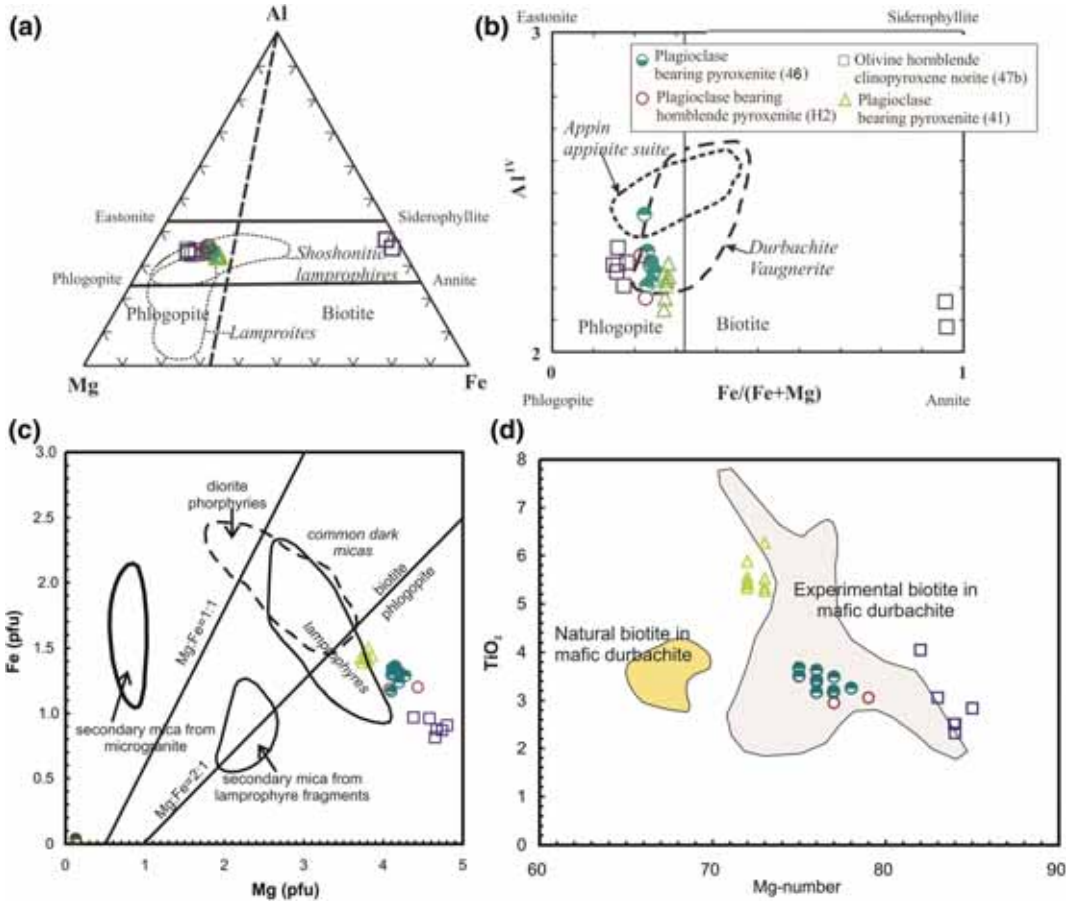


Figure 8. (**a**) Biotites from the mafic–ultramafic rocks of Purulia are plotted on an Al–Mg–Fe (mole%) diagram. The compositional ranges for biotites from the shoshonitic lamprophyres and lamproites worldwide are from Rock (1991). (**b**) Biotite compositions from the mafic–ultramafic rocks of Purulia in the phlogopite–biotite classification diagram (after Deer *et al.* 1962). Field of durbachite–vaugnerite is drawn from Buda and Dobosi (2004) while that of appinite is drawn from Hamidullah (2007). (**c**) Compositional variations of biotites from mafic–ultramafic rocks of Purulia in the Fe *vs.* Mg (in atoms per formula unit) diagram. Fields of primary and secondary biotites of lamprophyres and other rocks are from Pivec *et al.* (2002). (**d**) Plots of compositions of biotites of mafic–ultramafic rocks of Purulia in the Mg-number [Mg/(Mg+Fe)] *vs.* $TiO_2$ diagram. Compositional fields for experimental and natural biotites of the mafic durbachite are from Parat *et al.* (2010).

### 7.2 *Pressure of crystallization*

The composition of amphiboles can record the crystallization conditions ($P$, $T$, $fO_2$, $fH_2O$) of magmas (Ridolfi *et al.* 2010 and references therein). The studied mafic–ultramafic rocks contain abundant amphibole crystals and hence we used the composition of amphibole to estimate $P$–$T$ conditions and the depth of magma differentiation.

Many authors (see Pál-Molnár *et al.* 2015 and references therein) provide composition of amphiboles crystallized from alkaline basic magma ($SiO_2$: 46–56 wt%, MgO: 12–2.7 wt%) between 2–20 kbar and 920–1050°C. The amphiboles of the plagioclase-bearing pyroxenite (sample 46), olivine metanorite (sample 47b) and hornblende–orthopyroxene gabbro (H2) of present study when plotted in the Total-Al *vs.* Mg# and Total-Al *vs.* Ti diagrams of Pál-Molnár *et al.* (2015) (figure not shown), the plots of these amphiboles suggest crystallization at pressure and temperature between 4–10 kbar and 920–1050°C, respectively. However, amphiboles of plagioclase-bearing pyroxenite (sample 41) fall outside the fields of the experimentally derived amphiboles.

The total Al-content in amphibole structure (per formula unit) of calcic-amphibole in calc-alkaline magma is a sensitive indicator of pressure of crystallization and this can be used as a geobarometer to establish the depth of emplacement of magma (Hammerstrom and Zen 1986; Hollister *et al.* 1987; Johnson and Rutherford 1988; Schmidt 1992). Electron-microprobe data from amphibole

Table 7. *Representative analyses of olivine from mafic and ultramafic intrusives and cationic calculation on the basis of 4 oxygen.*

| Sl. no. | 1 | 2 | 3 | 4 | 5 |
|---|---|---|---|---|---|
| Sample | 47b | 47b | 47b | 47b | AD 443C |
| Analysis | 38/1 | 39/1 | 41/1 | 42/1 | |
| Location | Rim | Core | Rim | Core | |
| $SiO_2$ | 37.9 | 37.91 | 38.68 | 39.36 | 38.08 |
| $TiO_2$ | 0.14 | 0 | 0.02 | 0.07 | |
| $Al_2O_3$ | 0 | 0 | 0 | 0.02 | 0.01 |
| FeO | 22.93 | 22.63 | 23.17 | 22.33 | 24.57 |
| MnO | 0.28 | 0.21 | 0.29 | 0.25 | 0.26 |
| MgO | 38.55 | 39.46 | 39.06 | 39.94 | 36.1 |
| CaO | 0 | 0.02 | 0 | 0.04 | 0.04 |
| $Na_2O$ | 0 | 0 | 0.03 | 0 | |
| $K_2O$ | 0 | 0 | 0.02 | 0.02 | |
| **Total** | 99.8 | 100.23 | 101.27 | 102.03 | 99.06 |
| Si | 0.992 | 0.986 | 0.996 | 1.001 | 1.009 |
| Al | 0 | 0 | 0 | 0.001 | |
| Ti | 0.003 | 0 | 0 | 0.001 | |
| $Fe^{2+}$ | 0.502 | 0.492 | 0.499 | 0.475 | 0.544 |
| Mn | 0.006 | 0.005 | 0.006 | 0.005 | 0.005 |
| Mg | 1.504 | 1.53 | 1.5 | 1.514 | 1.426 |
| Ca | 0 | 0.001 | 0 | 0.001 | 0.001 |
| Na | 0 | 0 | 0.001 | 0 | |
| K | 0 | 0 | 0.001 | 0.001 | |
| **Total** | 3.007 | 3.014 | 3.003 | 2.999 | 2.985 |
| Mg/(Fe+Mg) | 0.75 | 0.76 | 0.75 | 0.76 | 0.72 |

Note: Sl. no. 1–4 from present study. Sl. no. 5 is from Mandal *et al.* (2007).

phenocrysts of Purulia mafic–ultramafic suite were used for estimating pressure, using the formulation of Schmidt (1992) as follows:

$$P\,(\pm 0.6\ \text{kbar}) = -3.01 + 4.76\text{Al}^{\text{t}} \quad \left(r^2 = 0.99\right).$$

Analyzed amphibole phenocrysts of websterite, olivine metanorite, hornblende gabbro-norite and olivine–hornblende pyroxenite show similar pressure estimates which range between 8.0 and 9.7 kbar and indicate intermediate-pressure fractionation. In one sample (sample 41, plagioclase-bearing pyroxenite), however, a lower pressure around 4.8 kbar was obtained using Al-in hornblende barometer of Schmidt (1992).

McCarthy and Patino Douce (1998) proposed silica–Ca-tschermak's–anorthite barometer that uses compositions of coexisting plagioclase, clinopyroxene and quartz. This empirical barometer gives a lower pressure of 4.3 kbar for plagioclase-bearing pyroxenite. However, for websterite and olivine metanorite this barometer gives 8.7 kbar and 9.2 kbar, respectively. The same barometer gives pressure as high as 10.7 kbar for hornblende gabbro-norite.

$Al_2O_3$ and $TiO_2$ content of natural Ca-amphibole depends upon pressure and temperature conditions of crystallization (Helz 1973; Ernst and Liu 1998). When the compositions of amphiboles of present study are plotted in the semiquantitative petrogenetic grid employing $Al_2O_3$ and $TiO_2$ contents of Ca-amphibole (Ernst and Liu 1998) of sub-alkaline rocks, we find that amphiboles of websterite and hornblende-bearing plagioclase pyroxenite give their crystallization pressure and temperature 10–15 kbar and 700–800°C. Plagioclase-bearing pyroxenites show lower pressure of crystallization, below 5 kbar, at elevated temperature level of >800°C. Amphibole of metanorite contains high $Al_2O_3$ (15.5 wt%) and low $TiO_2$ (0.61 wt%) and hence ∼20 kbar pressure and 650°C temperature are inferred for crystallization/recrystallization for this amphibole (figure 11a).

Ridolfi *et al.* (2010) have given several thermobarometric formulations applicable for amphibole with Mg#>0.5 crystallizing in calc-alkaline magma originated in subduction zones (i.e., <40 km and <1000 Mpa). The calculated barometry of hornblendes yield pressures for plagioclase-bearing pyroxenite and metanorite ranges from 2.2 kbar to 4.9 kbar and 5.8 kbar, respectively (table 10). Figure 11(b) shows $P$–$T$ estimates for selected hornblendes from plagioclase-bearing pyroxenite and hornblende gabbro-norite. Hornblende crystallization temperatures for plagioclase-bearing pyroxenite and metanorite range from 903° to 984°C and 1014°C, respectively (table 10). In the temperature *vs.* pressure diagram, hornblendes from one sample of plagioclase-bearing pyroxenite plot within domain 2 with similar crystallizing temperature ranging from 904° to 908°C, whereas another sample of plagioclase-bearing pyroxenite and a sample of hornblende gabbro-norite plot within domain 3, with high values ranging from 977° to 1014°C (figure 11b).

### 7.3 *Oxygen fugacity*

The fugacity of oxygen ($fO_2$) of magma depends on its source material and in turn, on its tectonic setting. Highly oxidizing magmas are found in convergent plate boundaries. Determining the $fO_2$ of parental magmas of mafic and ultramafic rocks may be difficult. However, some estimates can be done using the rock mineral assemblage and mineral

Table 8. *Representative analyses of spinel and magnetite from olivine metanorite and cationic calculation on the basis of 4 oxygen.*

| Sample | 47B | 47B | 47B | 47B | 47B |
|---|---|---|---|---|---|
| | Al–Mg-rich spinel | | | | Cr-Magnetite |
| Analysis | 47/1 | 48/1 | 58/1 | 59/1 | |
| Location | Inclusion within Olivine | | | | |
| $SiO_2$ | 0 | 0.01 | 0.02 | 0.05 | 0.43 |
| $TiO_2$ | 0.1 | 0.12 | 0.06 | 0.21 | 0 |
| $Cr_2O_3$ | 21.68 | 21.12 | 16.94 | 19.56 | 9.59 |
| $Al_2O_3$ | 40.08 | 40.03 | 44.56 | 40.43 | 0 |
| FeO | 28.08 | 28.42 | 27.66 | 29.69 | 88.8 |
| MnO | 0.3 | 0.18 | 0.21 | 0.03 | 0.13 |
| MgO | 7.78 | 7.89 | 9.07 | 8.06 | 0.07 |
| CaO | 0 | 0 | 0.04 | 0.02 | 0 |
| $Na_2O$ | 0.04 | 0.02 | 0.01 | 0.01 | 0 |
| $K_2O$ | 0.01 | 0 | 0 | 0.01 | 0 |
| **Totals** | 98.07 | 97.79 | 98.57 | 98.07 | 99.02 |
| Cations ($Fe^{2+}/Fe^{3+}$ charge balance) | | | | | |
| Si | 0.000 | 0.000 | 0.001 | 0.001 | 0.016 |
| Ti | 0.002 | 0.003 | 0.001 | 0.005 | 0.000 |
| Cr | 0.515 | 0.502 | 0.391 | 0.463 | 0.276 |
| Al | 1.419 | 1.420 | 1.532 | 1.426 | 0.000 |
| $Fe^{3+}$ | 0.064 | 0.073 | 0.074 | 0.100 | 1.693 |
| $Fe^{2+}$ | 0.641 | 0.642 | 0.600 | 0.643 | 1.008 |
| Mn | 0.008 | 0.005 | 0.005 | 0.001 | 0.004 |
| Mg | 0.348 | 0.354 | 0.394 | 0.360 | 0.004 |
| Ca | 0.000 | 0.000 | 0.001 | 0.001 | 0.000 |
| Na | 0.002 | 0.001 | 0.001 | 0.001 | 0.000 |
| K | 0.000 | 0.000 | 0.000 | 0.000 | 0.000 |
| **Total** | 3.000 | 3.000 | 3.000 | 3.000 | 3.000 |
| $Mg/(Mg+Fe^{2+}) * 100$ | 35.210 | 35.525 | 39.649 | 35.847 | 0.375 |
| $Cr/(Cr+Al) * 100$ | 26.621 | 26.137 | 20.317 | 24.499 | 100.000 |
| $Mg/(Mg+Fe^{2+}) * 100$ | 35.210 | 35.525 | 39.649 | 35.847 | 0.375 |
| $Fe^3/Fe^2$ | 0.10 | 0.11 | 0.12 | 0.15 | 1.68 |
| End members | | | | | |
| $FeCr_2O_4$ (Chromite) | 0.16 | 0.16 | 0.12 | 0.15 | 0.14 |
| $MgCr_2O_4$ | 0.09 | 0.09 | 0.08 | 0.08 | 0.00 |
| $FeAl_2O_4$ (Hercynite) | 0.45 | 0.45 | 0.46 | 0.46 | 0.00 |
| $MgAl_2O_4$ (Spinel) | 0.25 | 0.25 | 0.30 | 0.26 | 0.00 |
| $MnAl_2O_4$ (Galxite) | 0.01 | 0.00 | 0.00 | 0.00 | 0.00 |
| $FeFe_2O_4$ (Magnetite) | 0.02 | 0.02 | 0.02 | 0.03 | 0.84 |
| $MgFe_2O_4$ (Mg-Ferrite) | 0.01 | 0.01 | 0.01 | 0.02 | 0.00 |
| $MnFe_2O_4$ (Jacobsite) | 0.00 | 0.00 | 0.00 | 0.00 | 0.00 |
| **Total end members** | 0.99 | 1.00 | 1.00 | 1.00 | 0.98 |

chemistry. Under the high oxidizing conditions ($fO_2$ near hematite–magnetite buffer) titanomagnetite is one of the highest-temperature liquidus phases, whereas at the NNO (Ni–NiO) buffer, titanomagnetite crystallizes following olivine and calcic-clinopyroxene. Under lower oxidizing conditions, at around QFM (quartz–fayalite–magnetite) buffer, ilmenite crystallizes as high-temperature liquidus phase. Presence of magnetite and chromite in the mafic–ultramafics of the present study suggests that the crystallization took place under high oxygen-fugacity condition (Ishihara 1977).

Ridolfi *et al.* (2010) and later on, Ridolfi and Renzulli (2012) have given oxybarometric formulations using composition of amphiboles of calc-alkaline magma generated in convergent setting (<10 kbar). Ridolfi *et al.* (2010) have shown that in calc-alkaline rocks the $fO_2$ (relative to $\Delta$NNO) can

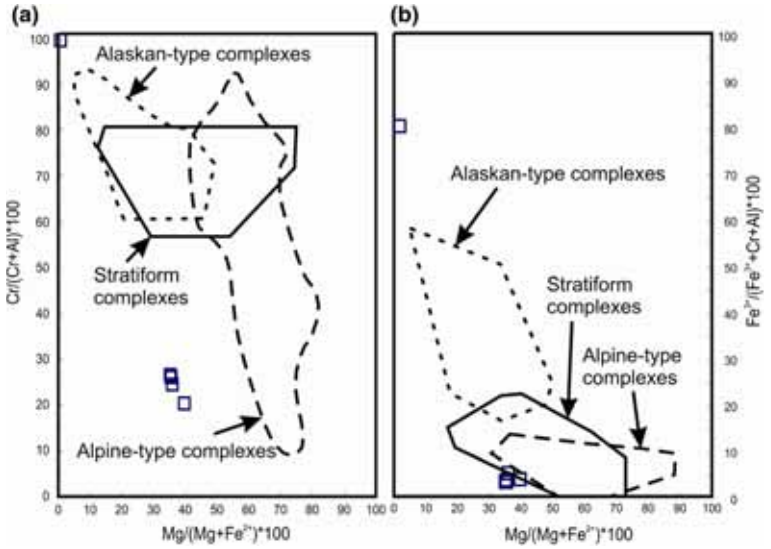


Figure 9. Plots of spinel composition of mafic rocks of Purulia in (**a**) 100Mg/(Mg+$Fe^{2+}$) *vs.* 100Cr/(Cr+Al) and (**b**) 100Mg/(Mg+$Fe^{2+}$) *vs.* 100$Fe^{3+}$/($Fe^{3+}$+Cr+Al) diagrams. Fields for alpine-type, Alaskan-type and Stratiform complexes are from Irvine (1967).

Table 9. *Representative major and trace element analyses of the mafic and ultramafic rocks.*

| Sample | 28 | 41 | 46 | 42 | 39 | 43 | 47a | 47b |
|---|---|---|---|---|---|---|---|---|
| Rock | Plagioclase-bearing Pyroxenite | | | Mela-olivine orthopyroxene gabbro | Mela-olivine hornblende clinopyroxene norite | Mela-clinopyroxene norite | Hornblende clinopyroxene (meta) norite | Olivine hornblende clinopyroxene (meta) norite |
| $SiO_2$ | 48.15 | 49.4 | 46.31 | 50.7 | 60.49 | 51.42 | 48.96 | 53.07 |
| $TiO_2$ | 0.45 | 0.59 | 1.02 | 0.87 | 0.99 | 0.52 | 0.38 | 0.38 |
| $Al_2O_3$ | 13.21 | 6.59 | 10.9 | 7.9 | 15.24 | 9.09 | 9.42 | 10.24 |
| $Fe_2O_3^T$ | 7.58 | 11.3 | 11.02 | 11.36 | 6.99 | 10.31 | 11.1 | 11.25 |
| MnO | 0.15 | 0.2 | 0.15 | 0.17 | 0.08 | 0.17 | 0.14 | 0.14 |
| MgO | 7.03 | 16.26 | 16.62 | 15.34 | 3.45 | 16.56 | 20.27 | 15.38 |
| CaO | 22.15 | 11.3 | 7.44 | 9.52 | 4.87 | 9.52 | 6.2 | 6.32 |
| $Na_2O$ | 0.21 | 0.74 | 1.52 | 0.88 | 2.97 | 1.17 | 2.05 | 2.62 |
| $K_2O$ | 0.18 | 0.38 | 2.08 | 1.18 | 2.6 | 0.62 | 1.48 | 1.51 |
| $P_2O_5$ | 0.21 | 0.25 | 0.57 | 0.42 | 0.62 | 0.13 | 0.13 | 0.11 |
| **Total** | 99.32 | 97.01 | 97.63 | 98.34 | 98.3 | 99.51 | 100.13 | 101.02 |
| Ba | 51 | 451 | 1102 | 1021 | 1881 | 341 | 453 | 391 |
| Rb | 9 | 10 | 56 | 28 | 73 | 16 | 70 | 91 |
| Sr | 82 | 302 | 706 | 523 | 689 | 170 | 337 | 377 |
| Nb | <5 | 3 | 17 | <5 | 26 | <5 | 14 | 12 |
| Zr | 49 | 93 | 156 | 91 | 197 | 56 | 116 | 98 |
| Y | 24 | 33 | 26 | 20 | 55 | 11 | 36 | 38 |
| Cr | 526 | 1530 | 1031 | 1210 | 93 | 1648 | 1612 | 1159 |
| Ni | 193 | 353 | 464 | 735 | 34 | 262 | 507 | 452 |
| Cu | <5 | 71 | 43 | 188 | 16 | 66 | 24 | 30 |
| Pb | 11 | 9 | 17 | <5 | 10 | <5 | 14 | 19 |

be calculated based on the Mg-content (pfu) of amphiboles. The $fO_2$ of plagioclase-bearing pyroxenite ($\Delta$NNO = +1.21 to +1.34) estimated following the calibration of Ridolfi *et al.* (2010) is higher than the $\Delta$NNO calculated from hornblende gabbro-norite ($\Delta$NNO = +1.95) (figure 11c). This variation of oxygen fugacity lies well within the range of relative $fO_2$ estimated from calc-alkaline

magmas ($\Delta$NNO from +1 to +3) as shown by Ridolfi *et al.* (2010).

The $fO_2$ relative to QFM-buffer ($\Delta$QFM) of basaltic magma could be estimated with the microprobe analyses of plagioclase and clinopyroxene by the method of France *et al.* (2010). The method is based on the differential behaviour of partitioning of $Fe^{2+}$ and $Fe^{3+}$ ions between coexisting clinopyroxene and melt, and plagioclase and melt. The clinopyroxene–plagioclase oxybarometer of France *et al.* (2010) is used to assess the $fO_2$ of mafic–ultramafics rocks of present study during crystallization. To apply this oxybarometer, we used the temperatures estimated with the two-pyroxene thermometers (table 10) and the bulk composition of the rock as an equivalent of the melt composition (see table 11). Based on the formulation of France *et al.* (2010), we obtained the oxygen fugacities values ($\Delta$QFM = –1.41 to +1.33) during crystallization of the magma, which are listed in table 10. The hornblende gabbronorite ($\Delta$QFM = +1.33) and plagioclase-bearing pyroxenite ($\Delta$QFM = +1.32) have yielded relatively higher $fO_2$ values than the websterite ($\Delta$QFM = –1.41) and olivine metanorite ($\Delta$QFM = –0.07).

Some of the olivines in olivine metanorite contain spinel inclusions. The $fO_2$ of the magma during crystallization is calculated according to the formulation of Nikolaev *et al.* (2016) using the composition of coexisting olivine–spinel. This oxybarometer is applicable for coexisting olivine ($X_{Fe}^{Ol} > 0.15$) and spinel in mafic magmas for temperatures >800°C. The results of this calculation are also shown in table 10. The pressure ($P$) was estimated as 9 kbar based on the average of pressure calculated with Al-in hornblende barometer (Schmidt 1992) and silica–Ca–tschermakite–anorthite barometer (McCarthy and Patino Douce 1998) while the temperature was estimated as 860°C by the Ca-exchange thermometer between olivine and clinopyroxene (Koehler and Brey 1990). Based on these calculations the $\Delta$QFM is estimated around +4.21 (following the formulation of Nikolaev *et al.* 2016).

### 7.4 *Water content of magma*

Water is a major volatile component of magma and controls various physico-chemical properties of the magma including phase relationships, viscosity, density, and diffusivity. Ridolfi *et al.* (2010) have shown that the $^{VI}Al$ content of amphibole is related to the water content of the melt. The $H_2O$-melt concentration during the crystallization of amphibole from the mafic–ultramafic rocks of the present area, calculated from Ridolfi *et al.*'s (2010) hygrometric formulation, ranges from 4.6% to 7.3% (table 10 and figure 11d).

## 8. Petrogenetic implications

### 8.1 *Field evidence for coexisting liquids of felsic and mafic magma*

The following field criteria suggest that the mafic/ultramafic rocks and the host porphyritic granitoids were not completely crystalline during emplacement.

1. Mafic rocks occur as rounded and oval-shaped patches (enclaves) throughout the host porphyritic granitoids suggesting mingling of felsic and mafic magma (e.g., Barbarin 2005; Kumar 2014).
2. Contacts between the mafic/ultramafic and porphyritic granitoids are generally sharp curvilinear which suggest that their parental magmas were under different viscosity.
3. The margins of the mafic/ultramafic enclaves may intricately interpenetrate with host porphyritic granitoids which suggests that both the mafic/ultramafic magma and the host granitoids were under compression before solidification.
4. The mafic and ultramafic rocks occur as small dykes and sills running parallel and transverse to the flow foliation of the porphyritic granitoids (figure 2a) suggesting injection of mafic magma along early fractures developed in the crystallizing granitoid body during cooling (Barbarin 2005).
5. Quenching textures are not observed across margins between granitoids and mafic/ultramafic enclaves which suggest that these were hot during emplacement.

We can suggest that parental magmas of both the mafic/ultramafic and felsic rock types coexisted as crystal mush while some interstitial liquid in them imparted fluidity and facilitated interaction. This in turn suggests a close relationship between the mafic/ultramafic rocks and granitoids.

### 8.2 *Evidence for the hydrous nature of the parental magma of the mafic–ultramafic rocks*

The following petrological and mineralo-chemical evidences indicate that the mafic–ultramafic rocks

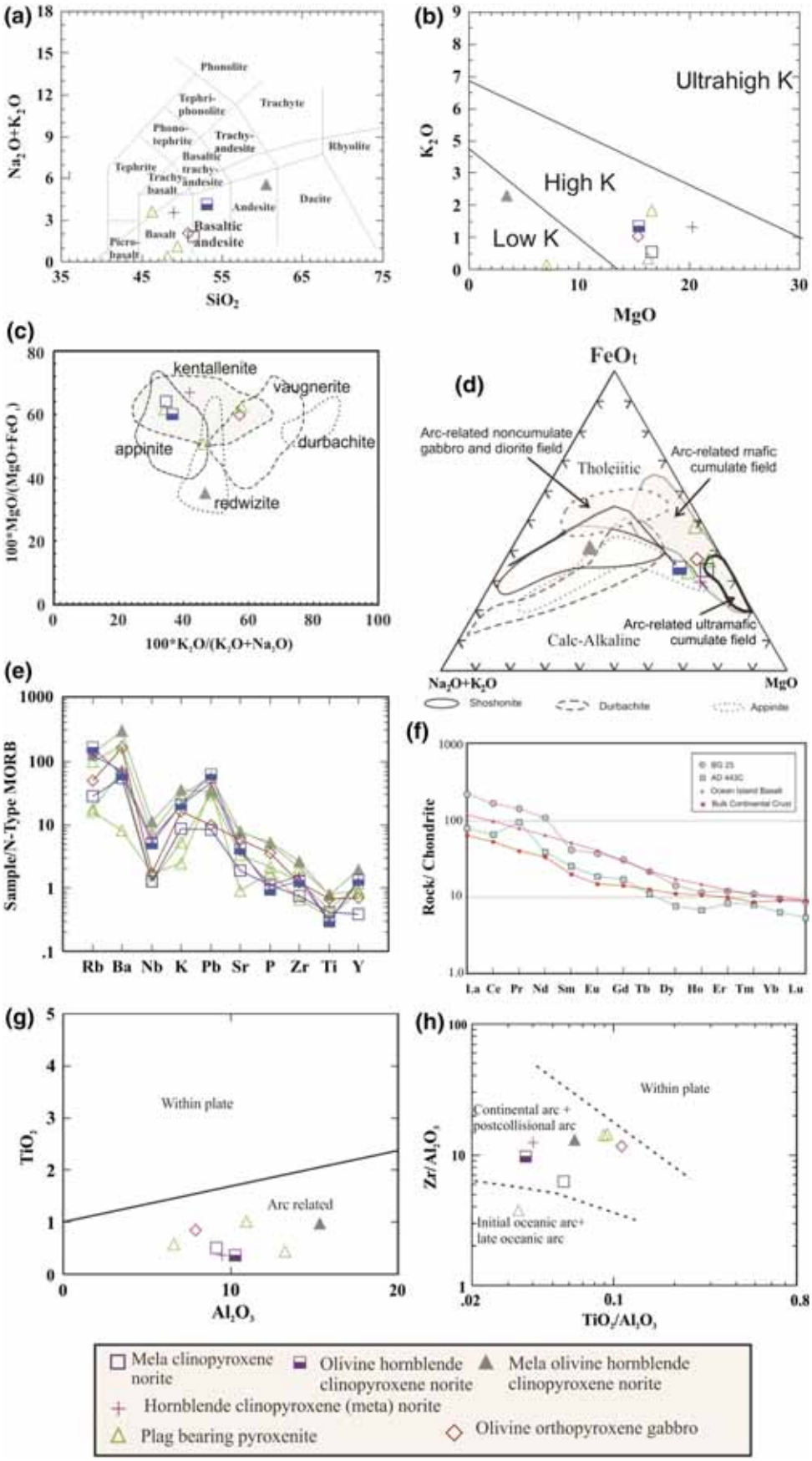
(a)
Phonolite
Tephri-phonolite
Trachyte
Phono-tephrite
Trachy-andesite
Rhyolite
Basaltic trachy-andesite
Tephrite
Trachy-basalt
Andesite
Dacite
Basalt
Basaltic andesite
Picro-basalt
$Na_2O+K_2O$
$SiO_2$
(b)
Ultrahigh K
High K
Low K
$K_2O$
MgO
(c)
kentallenite
vaugnerite
appinite
durbachite
redwizite
$100*MgO/(MgO+FeO_t)$
$100*K_2O/(K_2O+Na_2O)$
(d)
$FeO_t$
Arc-related noncumulate gabbro and diorite field
Tholeiitic
Arc-related mafic cumulate field
Arc-related ultramafic cumulate field
Calc-Alkaline
$Na_2O+K_2O$
MgO
Shoshonite
Durbachite
Appinite
(e)
Sample/N-Type MORB
Rb Ba Nb K Pb Sr P Zr Ti Y
(f)
Rock/ Chondrite
La Ce Pr Nd Sm Eu Gd Tb Dy Ho Er Tm Yb Lu
(g)
Within plate
Arc related
$TiO_2$
$Al_2O_3$
(h)
Within plate
Continental arc + postcollisional arc
Initial oceanic arc+ late oceanic arc
$Zr/Al_2O_3$
$TiO_2/Al_2O_3$
Mela clinopyroxene norite
Olivine hornblende clinopyroxene norite
Mela olivine hornblende clinopyroxene norite
Hornblende clinopyroxene (meta) norite
Plag bearing pyroxenite
Olivine orthopyroxene gabbro

of the present area accumulated from a water-enriched magma.

1. The characteristic feature of the mafic–ultramafic rocks of present study is the crystallization of euhedral clinopyroxene before the formation of labradoritic plagioclase (figure 4c and d). Müntener *et al.* (2001) suggested that high $H_2O$ contents (>3 wt%) of the magma leads to the crystallization of clinopyroxene before plagioclase. Crystallization of diopside before plagioclase in the mafic–ultramafic rocks of present study is consistent with the high (4.5–7.3 wt%) water content of parental melt as deduced in section 7.4 (also see figure 11d).
2. The mafic–ultramafic rocks are characterized by the development of euhedral hornblendes poikilitically enclosed within plagioclase which indicates their primary crystallization from the magma. Primary crystallization of hornblende from basaltic magma requires its high (>3 wt%) water content (Sisson and Grove 1993). Presence of primary hornblendes in the mafic–ultramafic rocks of Purulia is thus consistent with the estimation of high water content (4.5–7.3 wt% and table 10) of their parental magma.
3. In a basaltic melt high water content suppresses crystallization temperature of plagioclase which is otherwise higher in anhydrous basaltic magma (Sisson and Grove 1993). Hence, in the mafic–ultramafics of present study, plagioclase crystallization after hornblende (figure 4e) supports its formation in a water-enriched melt.
4. High water-pressure in the basaltic melt increases anorthite-enriched plagioclase to crystallize in the albite–anorthite–water system (Johannes 1978). High anorthite content of plagioclase (up to labradorite and rarely up to $An_{98}$) in large number of samples suggests high $P_{H_2O}$ of the parental magma.
5. In silica-saturated and silica-undersaturated melts under dry condition clinopyroxene incorporates Al in the $CaTiAl_2O_6$ molecule via the charge-coupled substitution of $^{vi}Mg^{iv}Si_2$ by $^{vi}Ti^{iv}Al_2$ when activity of titanium is greater than that of silicon in the melt specially in silica-undersaturated mafic melts (Loucks 1990). However, in hydrated mafic magma, the high $H_2O$ and $O_2$ fugacities supports coupled substitution of $^{vi}Mg^{iv}Si$ by $^{vi}Fe^{3+iv}Al$, and as a result Al is incorporated in clinopyroxene in the $CaFe^{3+}AlSiO_6$ molecule (Loucks 1990). High Al/Ti ratios (ranging between 5.05 and 47; av. 16.96, see figure 6c) of clinopyroxenes in the studied mafic–ultramafic rocks suggests that the crystallization took place under high water activity and high oxygen fugacity condition consistent with the calc-alkaline nature of the parental magma.
6. Relatively high $Cr_2O_3$ and Ca-contents of clinopyroxene, together with high Mg-content of olivine suggest that parental magma was hydrated basaltic one (Sisson and Grove 1993).

We know that both the asthenospheric and lithospheric mantle have very low water contents ($H_2O < 0.1$ wt%), and water content of the lower continental crust is particularly very very low (see Rudnick and Fountain 1995). However, fluids derived by dehydration of the subducting plate metasomatize the overlying lithospheric mantle wedge and as a result lithospheric mantle can contain high $H_2O$ (up to 12 wt%) content (Gaetani and Grove 1998). High $H_2O$ content of the mafic–ultramafic rocks of present study clearly suggest they crystallized from a hydrous basaltic magma having water content ranging between 4.5 and 7.3 wt% (table 10). We suggest that the parental mantle rock of the mafic–ultramafic rocks of present study, which underwent partial melting, was derived from a subduction-modified (metasomatized) mantle.

### 8.3 *Composition of the source magma of mafic rocks*

A sub-alkaline signature of the melt from which mafic–ultramafic rocks crystallized is inferred while describing the mineral chemistry of amphiboles and pyroxenes in section 5. The enrichment of calcium and aluminium in parental melt is inferred from the

Figure 10. Geochemical discrimination diagrams for mafic–ultramafic rocks of Purulia (**a**) total alkali *vs.* silica diagram (after Le Maitre *et al.* 2002), (**b**) MgO *vs.* $K_2O$ diagram (after Ferré and Leake 2001), (**c**) $100K_2O/(K_2O+Na_2O)$ *vs.* $100MgO/(MgO+FeO_t)$ diagram (after Rock 1991) and (**d**) $Na_2O+K_2O$–FeO(T)–MgO (AFM) diagram, after Irvine and Baragar (1971). (**e**) Spider plots normalized to NMORB (Sun and McDonough 1989). (**f**) Rare Earth Element patterns normalized to chondrite (McDonough and Sun 1995). REE data of the two mafic–ulutramafic samples were published in Mondal *et al.* (2007). These two samples were collected and analyzed by CB and BG, respectively. (**g**)–(**h**) Plots of samples of mafic–ultramafic rocks in tectonic discriminant diagrams $Al_2O_3$ *vs.* $TiO_2$ and $TiO_2/Al_2O_3$ *vs.* $Zr/Al_2O_3$ of Müller and Groves (1997).

Table 10. *Temperature, pressure, water content and oxygen fugacity of magma during crystallization.*

| | Temperature estimation (°C) | | | | | | | | | | | | | |
|---|---|---|---|---|---|---|---|---|---|---|---|---|---|---|
| Formulation | Holland and Blundy (1994) | Kretz (1982) | Wood and Banno (1973) | Wells (1977) | Henry *et al.* (2005) | Bertrand and Mercier (1985) | Brey and Köhler (1990) | Koehler and Brey (1990) | Taylor (1998) | Ridolfi *et al.* (2010) |
| Reaction | Plag/Hbl | Cpx/Opx | Cpx/Opx | Cpx/Opx | Ti in Biotite | Opx–Cpx solvus | Na in Pxn | Ol–Cpx Ca exchange | Opx–Cpx solvus | Amphibole composition |
| Sample | | | | | | | | | | |
| 41 | 785 | 605 | 1003 | 822 | 805 | 884 | 1052 | | 1017 | 905 |
| 46 | 782 | 578 | 1031 | 856 | 700 | 883 | 865 | | 985 | 980 |
| 47b | 799 | 500 | 975 | 817 | 634 | 743 | 650 | 860 | 1048 | |
| H1 | 819 | 1005 | 1088 | 828 | 772 | 1345 | 1004 | | 1444 | 1014 |

| | Pressure estimation (Kbar) | | | | | | | | | $H_2O$ in melt (wt%) | | $fO_2$ ($\Delta$NNO) | | |
|---|---|---|---|---|---|---|---|---|---|---|---|---|---|---|
| Formulation | Holland and Blundy (1994) | Hammerstrom and Zen (1986) | Hollister *et al.* (1987) | Johnson and Rutherford (1988) | Schmidt (1992) | Koehler and Brey (1990) | McCarthy and Patino Douce (1998) | Brey and Köhler (1990) | Ridolfi *et al.* (2010) | Ridolfi *et al.* (2010) | Amphibole composition | Ridolfi *et al.* (2010) | Nikolayev *et al.* (2016) | France *et al.* (2010) |
| Reactions | Plag/Hbl | Al-in hornblende | | | | Ol–Cpx Ca exchange | Silica–Ca-tschermak's–anorthite | | Amphibole composition | | | Amphibole composition | Oxygen-spinel | Fe-partitioning in Cpx–plag |
| Sample | | | | | | | | | | | | | | |
| 41 | 2.9 | 4.4 | 4.5 | 3.5 | 4.8 | | 4.3 | | 2.2 | 4.5 | | 1.2 | | 1.3 |
| 46 | 5.7 | 7.6 | 8.2 | 6.3 | 7.9 | | 8.7 | | 4.9 | 6.0 | | 1.1 | | −1.4 |
| 47b | 0.4 | 0.1 | 0.1 | 0.1 | 9.7 | 14.1 | 9.1 | | | 7.3 | | Not found | 3.7 | −0.7 |
| H1 | 5.0 | 8.2 | 8.8 | 6.8 | 8.5 | | 10.7 | | 5.8 | 6.2 | | 0.9 | | |

presence of anorthitic plagioclase and Al-rich chromian spinel in the rocks (Sisson and Grove 1993). In section 7.4, we have shown that the magma was rich in water. We can use the compositions of the chromian–spinel and olivine of olivine metanorite to estimate the composition of melt from which these minerals crystallized. $Al_2O_3$ contents, FeO/MgO ratios and $TiO_2$ contents of the parental melt can be calculated by the following equations:

$$(Al_2O_3)^{2.42}_{melt} = (Al_2O_3)_{spinel}/0.035$$

(after Maurel and Maurel 1982),

$$(FeO/MgO)^{melt} = (FeO/MgO)^{olivine}/(0.30 \pm 0.03)$$

(after Roeder and Emslie 1970);

$$(TiO_2)^{melt} = 1.0963 \times (TiO_2)^{10.7863}_{spinel}$$

(after Rollinson 2008).

The calculated $Al_2O_3$ component of the melt from which spinel of olivine metanorite crystallized is found to be 18.4–19.2 wt%. The FeO/MgO ratios of olivine (0.56–0.59) in olivine norite of present study require the parental melt with FeO/MgO ratios around 2. The $TiO_2$ content of the melt is estimated to be very low (<<0.01 wt%).

Chemometric equations for estimating major oxide composition of parental melt from the amphibole composition have been proposed by Ridolfi and Renzulli (2012) and Zhang *et al.* (2017). Composition of parental melt of mafic–ultramafic rocks of present study has been calculated and given in table 11. $Al_2O_3$ content of the parental melt of the mafic–ultramafic cumulates estimated by both the calibrations yield remarkably similar results (13.90–19.29 wt%). Estimated $SiO_2$ contents (48.16–67.64 wt%) of the melt using the formulation of Zhang *et al.* (2017) show lower values while $SiO_2$ contents calculated using the formulation of Ridolfi and Renzulli (2012) range between 62.39 and 74.52 wt%. On the other hand, CaO (3.01–11.73 wt%) contents of the parental melt estimated by the calibrations of Zhang *et al.* (2017) yield higher values than those estimated from the formulations of Ridolfi and Renzulli (2012), which gives a range of 2.37–8.45 wt% for CaO. Estimate of $TiO_2$ content of parental magma by Ridolfi and Renzulli (2012) calibration gives a range of 0.04–2.71 wt% while Zhang *et al.* (2017) calibration does not yield any

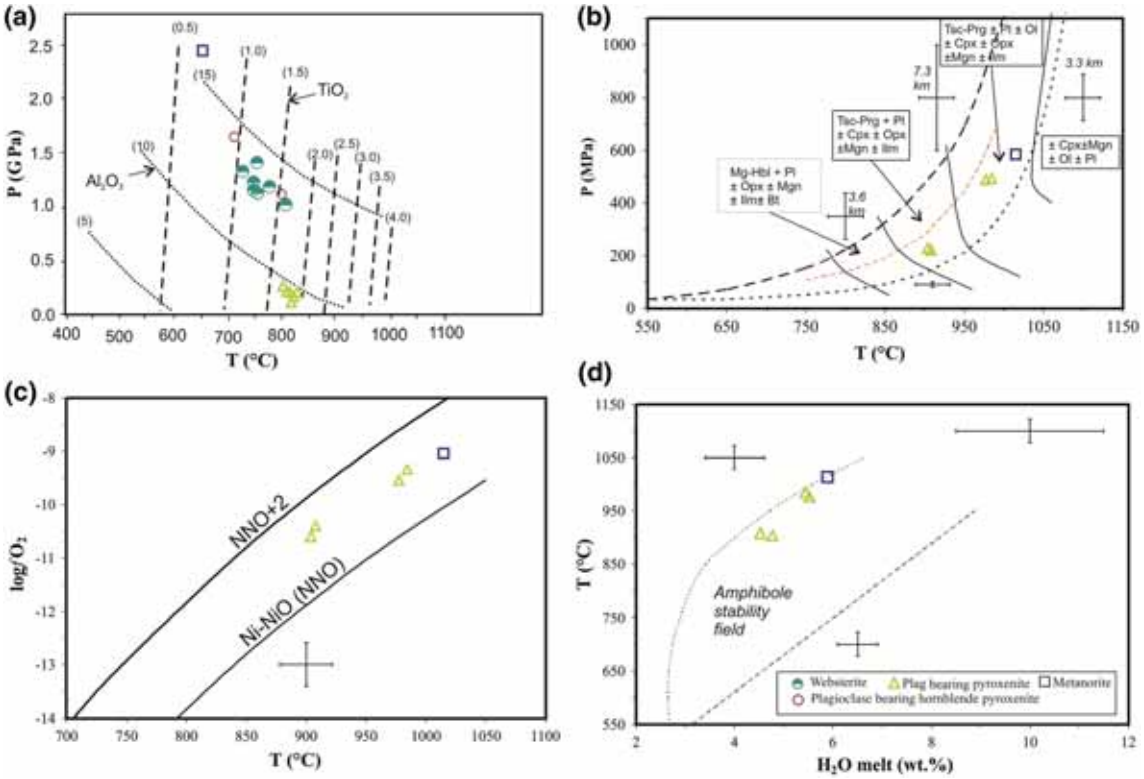


Figure 11. (**a**) $Al_2O_3$ and $TiO_2$ isopleths for amphibole in weight percent (Ernst and Liu 1998) with plot of amphiboles of the mafic–ultramafic rocks of Purulia. (**b**) Thermobarometric data, (**c**) oxygen fugacity, and (**d**) estimated melt $H_2O$ concentrations for mafic–ultramafic rocks of Purulia, based on recalculation of amphibole analyses using the method of Ridolfi *et al.* (2010).

result. Estimate of $K_2O$ content by Zhang *et al.* (2017) calibration yields 1.34–4.49 wt% while Ridolfi and Renzulli (2012) calibration for $K_2O$ gives a range of 8.27–16.04 wt%. Ridolfi and Renzulli (2012) formula gives that the parental magma of mafic–ultramafic rocks had Mg# [mol. MgO/$(MgO+FeO_t)$] ranging between 43.68 and 73.52 while calibrations of Zhang *et al.* (2017) gives that the parental magma had Mg# ranging between 46.73 and 59.78. It is to be noted here that the Mg# of the host porphyritic granitoids of these mafic–ultramafic rocks range from 30.19 to 47.73 (see Goswami and Bhattacharyya 2014). Thus the estimated composition of the parental magma of mafic–ultramafic rocks is consistent with the predicted composition of the hybrid magma formed by magma mixing between interacting mafic and felsic melt phases.

## 9. Conclusion

Pyroxenite, olivine pyroxenite, olivine–hornblende pyroxenite, plagioclase-bearing pyroxenite, olivine–pyroxene hornblendite, olivine hornblendite, clinopyroxene norite, orthopyroxene gabbro and norite, etc., comprise the mafic–ultramafic suite which occurs as sill, dyke, rounded enclaves and cumulate autoliths within porphyritic granitoids. While dykes and sills of mafic rocks depict injection of mafic magma along early fractures developed in the crystallizing granitoid magma during cooling, ulramafic rocks showing cumulate textures are autoliths formed from the fractional crystallization of the parental homogenized magma (cf. Barbarin 2005). Mafic magmatic enclaves are suggested to be formed due to the incomplete mixing of the mafic melt and granitoid magma (Kumar 2014). Thus mafic and ultramafic rocks are spatially and temporally related with the host porphyritic granitoids. The porphyritic granitoids were emplaced in a post-collisional tectonic setting (Goswami and Bhattacharyya 2014) around 998±10 Ma ago (Chakraborty *et al.* 2019). We can postulate similar age for the mafic–ultramafic suite. The undeformed and unmetamorphosed characters of mafic–ultramafic rocks also suggest their post-collisional emplacement. Mafic/ultramafic rocks have the same mineral constituents, however, at different modal proportions. Primary calcic clinopyroxene, orthopyroxene, hornblende, olivine, biotite and calcic plagioclase along with accessory magnetite, spinel, sphene, etc., are the constituent minerals of the rock suite.

Table 11. *Composition of parental melt deduced from amphibole composition following calibrations of Zhang et al. (2017) and Ridolfi and Renzulli (2012).*

| Sample | 41 | 41 | 41 | 41 | 41 | H2 | H2 | 47b |
|---|---|---|---|---|---|---|---|---|
| Analysis | 15/1 | 19/1 | 1\1 | 32/1 | 38/1 | 35/1 | 36/1 | 40/1 |
| Location | Core | Core | Core | Core | Core | | | Core |
| Melt composition (Zhang *et al.* 2017) | | | | | | | | |
| $SiO_2$ | 65.44 | 67.64 | 64.28 | 66.08 | 66.05 | 55.14 | 55.36 | 48.16 |
| $Al_2O_3$ | 14.04 | 13.90 | 14.28 | 14.21 | 14.18 | 18.92 | 18.40 | 19.19 |
| MgO | 0.76 | 0.59 | 0.77 | 0.76 | 0.69 | 3.63 | 3.09 | 5.05 |
| $Fe_2O_3^T$ | 1.83 | 1.56 | 2.05 | 1.89 | 1.77 | 6.60 | 6.27 | 7.91 |
| CaO | 3.47 | 3.01 | 3.53 | 3.42 | 3.40 | 8.65 | 7.55 | 11.73 |
| $K_2O$ | 4.36 | 4.32 | 4.49 | 4.18 | 4.24 | 1.34 | 1.89 | 1.99 |
| **Total** | 89.91 | 91.02 | 89.40 | 90.54 | 90.32 | 94.28 | 92.56 | 94.02 |
| Mg# | 49.01 | 46.93 | 46.73 | 48.28 | 47.52 | 56.15 | 53.43 | 59.78 |
| Melt composition (Ridolfi and Renzulli 2012) | | | | | | | | |
| $SiO_2$ | 72.79 | 74.52 | 71.76 | 72.69 | 74.46 | 65.31 | 64.81 | 62.39 |
| $TiO_2$ | 0.08 | 0.04 | 0.10 | 0.06 | 0.06 | 0.64 | 0.58 | 2.71 |
| $Al_2O_3$ | 14.31 | 13.93 | 14.67 | 14.74 | 14.39 | 19.17 | 18.88 | 19.29 |
| $Fe_2O_3^T$ | 1.06 | 1.08 | 1.16 | 1.21 | 0.91 | 2.16 | 2.38 | 1.79 |
| MgO | 1.26 | 1.05 | 1.25 | 1.07 | 0.82 | 0.72 | 0.88 | 1.36 |
| CaO | | | | | | 4.55 | 3.67 | 8.45 |
| $K_2O$ | 10.79 | 8.49 | 10.87 | 10.16 | 12.30 | 8.33 | 8.27 | 10.71 |
| **Total** | 100.30 | 99.11 | 99.81 | 99.92 | 102.94 | 100.87 | 99.47 | 106.71 |
| Mg# | 73.52 | 69.38 | 71.56 | 67.28 | 67.61 | 43.68 | 46.27 | 63.80 |

| Sample | 46 | 46 | 46 | 46 | 46 | 46 | 46 |
|---|---|---|---|---|---|---|---|
| Analysis | 46/1 | 50/1 | 56/1 | 59/1 | 73/1 | 79/1 | 80/1 |
| Location | Core | Core | Core | Core | Core | Core | Core |
| Melt composition (Zhang *et al.* 2017) | | | | | | | |
| $SiO_2$ | 56.98 | 54.89 | 57.47 | 56.28 | 59.99 | 54.55 | 56.48 |
| $Al_2O_3$ | 17.41 | 17.13 | 17.18 | 17.01 | 16.89 | 17.46 | 16.82 |
| MgO | 2.23 | 2.28 | 2.04 | 2.08 | 1.70 | 2.27 | 1.86 |
| $Fe_2O_3^T$ | 4.94 | 5.00 | 4.78 | 4.74 | 3.91 | 5.31 | 4.58 |
| CaO | 6.93 | 6.84 | 6.48 | 6.39 | 6.13 | 7.26 | 6.16 |
| $K_2O$ | 2.58 | 3.11 | 2.67 | 3.05 | 2.61 | 2.95 | 3.24 |
| **Total** | 91.08 | 89.26 | 90.62 | 89.54 | 91.23 | 89.80 | 89.13 |
| Mg# | 51.29 | 51.55 | 49.90 | 50.54 | 50.31 | 49.86 | 48.59 |
| Melt composition (Ridolfi and Renzulli 2012) | | | | | | | |
| $SiO_2$ | 64.82 | 66.72 | 67.69 | 67.19 | 68.15 | 65.32 | 66.80 |
| $TiO_2$ | 0.76 | 0.72 | 0.44 | 0.51 | 0.35 | 1.00 | 0.57 |
| $Al_2O_3$ | 17.93 | 17.50 | 17.84 | 17.55 | 17.47 | 17.92 | 17.41 |
| $Fe_2O_3^T$ | 1.93 | 1.35 | 1.39 | 1.43 | 1.42 | 1.50 | 1.44 |
| MgO | 1.24 | 1.06 | 0.59 | 0.89 | 0.69 | 1.07 | 0.96 |
| CaO | 4.94 | 3.86 | 2.54 | 2.74 | 2.37 | 5.08 | 2.97 |
| $K_2O$ | 10.11 | 14.29 | 16.04 | 14.21 | 13.38 | 14.21 | 14.73 |
| **Total** | 101.73 | 105.49 | 106.54 | 104.52 | 103.83 | 106.11 | 104.88 |
| Mg# | 59.95 | 64.73 | 49.94 | 59.40 | 53.16 | 62.36 | 60.97 |

The compositions of amphiboles, pyroxenes and biotites of those rocks show similarity with those from lamprophyres, appinites and durbachites. In the total alkali *vs.* $SiO_2$ (TAS) diagram, these rocks embrace the fields of basalt, basaltic andesite and andesite. In the $100K_2O/(K_2O+Na_2O)$ *vs.* $100MgO/(MgO+FeO_t)$ diagram of Rock (1991) the mafic–ultramafic rocks of present study largely fall in the field of kentallenite of appinite suite of Caledonide belt. These rocks are characterized by the enrichment of both the compatible (Ni and Cr) and incompatible elements (K, Rb and Ba) and LREEs and depleted Nb and Ti which are similar to the characters of the post-collisional mafic–ultramafic

rocks encountered in the Caledonides and Variscan belts of Europe. Assemblage of biotite–magnetite–sphene suggests that these rocks crystallized under high $fO_2$ condition. Presence of abundant primary amphibole and phlogopite suggests that these were crystallized from a hydrous magma. Crystallization of clinopyroxene before the formation of labradorite together with the crystallization of primary hornblende suggests high $H_2O$ contents (>3%) of the parental magma. High Al/Ti ratios, relatively high $Cr_2O_3$ and Ca-contents of clinopyroxene suggest that the crystallization took place under high water activity and high oxygen fugacity condition.

Liquidus temperature of the parental magma of the mafic–ultramafic rocks obtained by two-pyroxene thermometer of Wood and Banno (1973) (975–1088°C) is quite similar to the experimentally determined liquidus temperature of vaugnerite magma (∼1000°C) at 2 kbar pressure (Montel and Weisbord 1986). The near-solidus pressure and temperature of crystallization of the mafic–ultramafic rocks have been estimated using the amphibole–plagioclase geothermobarometeric calculations of Holland and Blundy (1994) and give a range between 2.9–5.7 kbar and 782–819°C. The high $fO_2$ ($\Delta$NNO ranges between +0.9 and +1.2) and water content of magma (4.5–7.3 wt%) were also estimated using amphibole composition following the formulations of Ridolfi *et al.* (2010). Similar $P$, $T$ and $fO_2$ values were obtained using other thermobarometric calibrations. High $fO_2$ and high water content of the magma are characteristics of calc-alkaline magma emplaced in convergent setting.

Computations of chemometric equations for determining major oxide composition of parental melt from the amphibole composition yields high $SiO_2$ (48.16–67.64 wt%), high CaO (3.01–11.73 wt%), high $K_2O$ (1.34–4.49 wt%) and low $TiO_2$ content (0.04–2.71 wt%) and intermediate Mg# (46.73–59.78) of the magma. The estimated composition of the parental magma is consistent with the predicted composition of the hybrid magma formed by magma mixing between interacting mafic and felsic melt phases.

## Acknowledgements

The Research Fellowship in Sciences for meritorious students (RFSMS) of the University Grants Commission, Government of India awarded to Susmita Das (No. F.7-47/2007 BSR) and research and fieldwork grants of the University of Calcutta given to Bapi Goswami are gratefully acknowledged. Thanks are due to Sri B Chattopadhyay, Dr S Nandy and Sri S K Tripathy (EPMA Laboratory, CHQ, GSI, Kolkata) for providing electron microprobe facilities. We are grateful to Prof J Mukhopadhyay, Prof A Roy and Dr S K Bhaduri for kindly analyzing the samples by XRF. We also thank two anonymous reviewers for their constructive comments and Prof Rajneesh Bhutani for the efficient editorial handling of this manuscript.

## References

Acharya S K 2003 A plate tectonic model for Proterozoic crustal evolution of Central Indian Tectonic Zone; *Gondwana Res.* **7** 9–31.

Barbarin B 2005 Mafic magmatic enclaves and mafic rocks associated with some granitoids of the central Sierra Nevada batholith, California: Nature, origin, and relations with the hosts; *Lithos* **80(1–4)** 155–177.

Beard J S, Ragland P C and Rushmer T 2004 Hydration crystallization reactions between anhydrous minerals and hydrous melt to yield amphibole and biotite in igneous rocks: Description and implications; *J. Geol.* **112(5)** 617–621.

Bertrand P and Mercier J C C 1985 The mutual solubility of coexisting ortho- and clinopyroxene: Toward an absolute geothermometer for the natural system? *Earth Planet. Sci. Lett.* **76(1–2)** 109–122.

Bhowmik S K, Wilde S A, Bhandari A, Pal T and Pant N C 2012 Growth of the Greater Indian Landmass and its Assembly in Rodinia: Geochronological evidence from the Central Indian tectonic Zone; *Gond. Res.* **22** 54–72.

Blundy J D and Holland T J B 1990 Calcic amphibole equilibria and a new amphibole–plagioclase geothermometer; *Contrib. Mineral. Petrol.* **104** 208–224.

Bora S, Kumar S, Yi K, Kim N and Lee T H 2013 Geochemistry and U–Pb SHRIMP zircon chronology of granitoids and microgranular enclaves from Jhirgadandi Pluton of Mahakoshal belt, Central India Tectonic Zone India; *J. Asian Earth Sci.* **70–71** 99–114.

Bowes D R and Košler J 1993 Geochemical comparisons of the subvolcanic appinite suites of the British Caledonides and the Durbachite suite of the central European Hercynides: Evidence for associated shoshonitic and granitic magmatism; *Miner. Petrol.* **48** 47–63.

Brey G P and Köhler T 1990 Geothermobarometry in four-phase lherzolites. II. New thermobarometers, and practical assessment of existing thermobarometers; *J. Petrol.* **31(6)** 1353–1378.

Buda G and Dobosi G 2004 Lamprophyre-derived high-K mafic enclaves in Variscan granitoids from the Mecsek Mts (South Hungary); *Neues. Jb. Miner. Abh.: J. Mineral. Geochem.* **180(2)** 115–147.

Castro A, Corretge´ G, de la Rosa J D and Fernandéz C 2003 The appinite migmatite complex of Sanabria, NW Iberian massif, Spain; *J. Petrol.* **44** 1309–1344.

Chakraborty T, Upadhyay D, Ranjan S, Pruseth K L and Nanda J K 2019 The geological evolution of the Gangpur Schist Belt, eastern India: Constraints on the formation of the Greater Indian Landmass in the Proterozoic; *J. Metamorph. Geol.* **37(1)** 113–151.

Couzinié S, Moyen J-F, Villaros A, Paquette J-L, Scarrow J H and Marignac C 2014 Temporal relationships between Mg–K mafic magmatism and catastrophic melting of the Variscan crust in the southern part of Velay Complex (Massif Central, France); *J. Geosci.-Czech.* **59(1)** 69–86.

Couzinié S, Laurent O, Moyen J F, Zeh A, Bouilhol P and Villaros A 2016 Post-collisional magmatism: Crustal growth not identified by zircon Hf–O isotopes; *Earth Planet. Sci. Lett.* **456** 182–195.

Dai L Q, Zhao Z F, Zheng Y F and Zhang J 2015 Source and magma mixing processes in continental subduction factory: Geochemical evidence from post-collisional mafic igneous rocks in the Dabie orogeny; *AGU pub.* **16** 659–680.

Deer W A, Howie R A and Zussman J 1992 An introduction to the rock forming minerals, 2nd edn, Longman Group UK, Harlow, 232p.

Dick H J B 1977 Partial melting in the Josephine peridotite: (1) The effect on mineral composition and its consequences for geobarometry and geothermometry; *Am. J. Sci.* **277** 801–832.

Engel A E J and Engel C 1960 Progressive metamorphism and granitisation of the major paragneiss, Northwest Adirondack Mountains, New York. Part II: Mineralogy; *Bull. Geol. Soc. Amer.* **71** 1–58.

Ernst W G and Liu j 1998 Experimental phase-equilibrium study of Al- and Ti-contents of calcic amphibole in MORB – A semiquantitative thermobarometer; *Am. Mineral.* **83** 952–969.

Ferré E C and Leake B E 2001 Geodynamic significance of early orogenic high-K crustal and mantle melts: Example of the Corsica Batholith; *Lithos* **59(1–2)** 47–67.

Fowler M B, Kocks H, Darbyshire D P F and Greenwood P B 2008 Petrogenesis of high Ba–Sr plutons from the Northern Highlands Terrane of the British Caledonian Province; *Lithos* **105** 129–148.

Fowler M B, Henney P J 1996 Mixed Caledonian appinite magmas: Implications for lamprophyre fractionation and high Ba–Sr granite genesis; *Contrib. Mineral. Petrol.* **126(1–2)** 199–215.

France L, Koepke J, Ildefonse B, Cichy S B and Deschamps F 2010 Hydrous Partial Melting in the Sheeted Dike Complex at Fast Spreading Ridges: Experimental and Natural Observations; *Contrib. Mineral. Petrol.* **160** 683–704.

Frost B R and Chacko T 1989 The granulite uncertainty principle: Limitations on thermobarometry in granulites; *J. Geol.* **97(4)** 435–450.

Gaetani G A and Grove T L 1998 The influence of water on melting of mantle peridotite; *Contrib. Mineral. Petrol.* **131** 323–346.

Girardeau J and Mevel C 1982 Amphibolitized sheared gabbros from ophiolites as indicators of the evolution of the oceanic crust: Bay of Islands, Newfoundland; *Earth Planet. Sci. Lett.* **61(1)** 151–165.

Goswami B and Bhattacharyya C 2008 (published in 2010) Tectonothermal evolution of Chhotanagpur Granite Gneiss Complex from northeastern part of Puruliya district, West Bengal, eastern India; *Ind. J. Geol.* **80(1–4)** 41–54.

Goswami B and Bhattacharyya C 2014 Petrogenesis of shoshonitic granitoids, eastern India: Implications for the late Grenvillian post-collisional magmatism; *Geosci. Frontiers* **5** 821–843.

Goswami B, Roy P, Basak A, Das S and Bhattacharyya C 2018 Physico-chemical conditions of four calc-alkaline granitoid plutons of Chhotanagpur Gneissic Complex, eastern India: Tectonic implications; *J. Earth Syst. Sci.* **127(8)** Article ID 120.

Hamidullah S 2007 Petrography and mineral chemistry as indicators of variations of crystallization conditions in the Loch Lomond and Appin appinite suites, western Scotland; *Proc. Geol. Assoc.* **118(1)** 101–115.

Hammerstrom J M and Zen E 1986 Aluminium-in-hornblende. An empirical igneous barometer; *Am. Mineral.* **71** 1297–1313.

Helz R T 1973 Phase relations of basalts in their melting range at $PH_2O$ = 5 5 kb as a function of oxygen fugacity; *J. Petrol.* **14** 249–302.

Henry D J, Guidotti C V and Thomson J A 2005 The Ti-saturation surface for low-to-medium pressure metapelitic biotites: Implications for geothermometry and Ti-substitution mechanisms; *Am. Mineral.* **90(2–3)** 316–328.

Hofmann A W 1988 Chemical differentiation of the Earth: The relationship between mantle, continental crust, and oceanic crust; *Earth Planet. Sci. Lett.* **90** 297–314.

Holland J B and Blundy T J B 1994 Non-ideal interactions in calcic amphiboles and their bearing on amphibole-plagioclase thermometry; *Contrib. Mineral. Petrol.* **116** 433–447.

Hollister L S, Grissom G C, Peters E K, Stowell H H and Sisson V B 1987 Confirmation of empirical correlation of Al in hornblende with pressure of solidification of calc-alkaline plutons; *Am. Mineral.* **72** 231–239.

Holub F V 1997 Ultrapotassic plutonic rocks of the durbachite series in the Bohemian Massif: petrology, geochemistry and petrogenetic interpretation; *Sbor. Geol. Ved, Ložisk. Geol. Miner.* **31** 5–26.

Irvine T N 1967 Chromian spinel as a petrogenetic indicator: part 2. Petrologic applications; *Can. J. Earth Sci.* **4** 71–103.

Ishihara S 1977 The magnetite-series and ilmenite-series granitic rocks; *Mining Geol.* **27** 293–305.

Jackson E D 1963 Stratigraphic and lateral variations of chromite compositions in the Stillwater Complex; *Mineral. Soc. Amer. Spl. Paper* **1** 46–54.

Jahn B M, Wu F, Lo C H and Tsai C H 1999 Crust-mantle interaction induced by deep subduction of the continental crust: Geochemical and Sr–Nd isotopic evidence from post-collisional mafic–ultramafic intrusions of the northern Dabie complex, central China; *Chem. Geol.* **157(1–2)** 119–146.

Janoušek V and Holub F V 2007 The causal link between HP–HT metamorphism and ultrapotassic magmatism in collisional orogens: Case study from the Moldanubian Zone of the Bohemian Massif; *Proc. Geol. Assoc.* **118(1)** 75–86.

Jayananda M, Miyazaki T, Gireesh R V, Mahesha N and Kano T 2009 Synplutonic mafic dykes from late Archaean granitoids in the Eastern Dharwar Craton, Southern India; *J. Geol. Soc. India* **73(1)** 117.

Johannes W 1978 The melting of plagioclase in the system Ab–An–$H_2O$ and Qz–Ab–An–$H_2O$ at $P(H_2O)$ = 5 kbar, an equilibrium problem; *Contrib. Mineral. Petrol.* **66** 295–303.

Johnson M C and Rutherford M J 1988 Experimental calibration of the al-in-hornblende geobarometer with application to Long Valley Caldera (California) volcanic rocks; *Geology* **17** 837–841.

Karmakar S, Bose S, Sarbadhikari A B and Das K 2011 Evolution of granulite enclaves and associated gneisses from Purulia, Chhotanagpur Granite Gneiss Complex, India: Evidence for 990–940 Ma tectonothermal event(s) at the eastern India cratonic fringe zone; *J. Asian Earth Sci.* **41(1)** 69–88.

Koehler T and Brey G P 1990 Calcium exchange between olivine and clinopyroxene calibrated as a geothermobarometer for natural peridotites from 2 to 60 kb with applications; *Geochim. Cosmochim. Acta.* **54(9)** 2375–2388.

Kretz R 1982 Transfer and exchange equilibrium in a portion of the pyroxene quadrilateral as deduced from natural and experimental data; *Geochim. Cosmochim. Acta.* **46** 411–421.

Kumar S 2014 Magmatic Processes: Review of Some Concepts and Models; In: *Modelling of Magmatic and Allied Processes* (eds) Kumar S and Singh R N, Society of Earth Scientists Series, pp. 1–23.

Le Bas M J 1962 The role of aluminum in igneous clinopyroxenes with relation to their parentage; *Am. J. Sci.* **260** 267–288.

Le Maitre R W 2002 A Classification of Igneous Rocks and a Glossary of Terms: Recommendations of the International Union of Geological Sciences Sub-commission on the Systematics of Igneous Rocks, Blackwell, Oxford.

Leake B E 1997 Nomenclature of amphiboles: Report of the Subcommittee on Amphiboles of the International Mineralogical Association, Commission on New Minerals and Mineral Names; *Am. Mineral.* **82** 1019–1037.

Leterrier J, Maury R C, Thonon P, Girard D and Marchal M 1982 Clinopyroxene composition as a method of identification of the magmatic affinities of palaeo-volcanic series; *Earth Planet. Sci. Lett.* **59** 139–154.

Loucks R R 1990 Discrimination of ophiolitic from non-ophiolitic ultramafic–mafic allochthons in orogenic belts by the Al/Ti ratios in clinopyroxene; *Geology* **18** 346–349.

Mahadevan T M 2002 Geology of Bihar and Jharkhand, Geological Society of India, Bangalore, 563p.

Macpherson C G, Dreher S T and Thirlwall M F 2006 Adakites without slab melting: High pressure differentiation of island arc magma, Mindanao, the Philippines; *Earth Planet. Sci. Lett.* **243(3–4)** 581–593.

Mandal A, Goswami B, Mukherjee S, Das S, Bhattacharyya I and Bhattacharyya C 2007 Mantle metasomatism of Ultramafic intrusives in Chhotanagpur Granite Gneiss Complex, Puruliya district, West Bengal, Eastern India: Evidence from trace element and REE geochemistry; In: *Igneous Petrology: 21st Century Perspective* (eds) Ray J and Bhattacharyya C, Allied Publishers Pvt. Ltd, pp. 122–142.

Maurel C and Maurel P 1982 Étude expérimentale de la solubilité du chrome dans les bains silicatés basiques et sa distribution entre liquide et minéraux coexistants: Conditions d'existence du spinelle chromifère; *Bull. Minéral.* **105** 640–647.

Mazumdar S K 1988 Crustal evolution of the Chhotanagpur gneissic complex and the Mica Belt of Bihar; In: *Precambrian of the Eastern Indian Shield* (ed.) Mukhopadhyay D, *Mem. Geol. Soc. India* **8** 49–84.

McCarthy T C and Patino Douce A E 1998 Empirical calibration of the silica-ca-tschermak-anorthite (SCAn) geobarometer; *J. Metamorph. Geol.* **16** 675–686.

McDonough W F and Sun S S 1995 The composition of the Earth; *Chem. Geol.* **120(3–4)** 223–253.

Molina J, Scarrow J, Montero P G and Bea F 2009 High-Ti amphibole as a petrogenetic indicator of magma chemistry: Evidence for mildly alkalic–hybrid melts during evolution of Variscan basic–ultrabasic magmatism of Central Iberia; *Contrib. Mineral. Petrol.* **158** 69–98.

Montel J M and Weisbrod A 1986 Characteristics and evolution of 'vaugneritic magmas': An analytical and experimental approach, on the example of the Cévennes Médianes (French Massif Central); *Bull. Minéral.* **109(5)** 575–587.

Morimoto N 1988 Nomenclature of pyroxenes; *Miner. Petrol.* **39(1)** 55–76.

Müller D and Groves D I 1997 Potassic Igneous Rocks and Associated Gold–Copper Mineralization, 3rd edn, Springer-Verlag, Berlin, pp. 1–238.

Müntener O, Kelemen P B and Grove T L 2001 The role of $H_2O$ during crystallization of primitive arc magmas under uppermost mantle conditions and genesis of igneous pyroxenites: An experimental study; *Contrib. Mineral. Petrol.* **141(6)** 643–658.

Nikolaev G S, Ariskin A A, Barmina G S, Naza-rov M A and Almeev R R 2016 Test of the Ballhaus–Berry–Green Ol–Opx–Sp Oxybarometer and calibration of a new equation for estimating the redox state of melts saturated with olivine and spinel; *Geochem. Int.* **54(4)** 301–320.

Nisbet E G and Pearce J A 1977 Clinopyroxene composition in mafic lavas from different tectonic settings; *Contrib. Mineral. Petrol.* **63** 149–160.

Nixon G T, Cabri L J and Laflamme J H G 1990 Platinum-group element mineralization in lode and placer deposits associated with the Tulameen Alaskan-type complex, British Columbia; *Can. Mineral.* **28** 503–535.

Pál-Molnár E, Batki A, Almási E, Kiss B, Upton B G J, Markl G, Odling N and Harangi S 2015 Origin of mafic and ultramafic cumulates from the Ditrău Alkaline Massif, Romania; *Lithos* **239** 1–18.

Parat F, Holtz F, René M and Almeev R 2010 Experimental constraints on ultrapotassic magmatism from the Bohemian Massif (durbachite series, Czech Republic); *Contrib. Mineral. Petrol.* **159(3)** 331–347.

Patiño Douce A E 1993 Titanium substitution in biotite: An empirical model with applications to thermometry, $O_2$ and $H_2O$ barometries, and consequences for biotite stability; *Chem. Geol.* **108(1–4)**133–162.

Piccardo G B, Messiga B and Vannucci R 1988 The Zabargad peridotite–pyroxenite association: Petrological constraints on its evolution; *Tectonophys.* **150(1–2)** 135–162.

Pivec E, Holub F V, Lang M, Novak J K and Stemprok M 2002 Rock-forming minerals of lamprophyres and associated mafic dykes from the Krusné hory/Erzgebirge (Czech Republic); *J. Geosci.* **47(1–2)** 23–34.

Radhakrishna B P and Naqvi S M 1986 Precambrian continental crust of India and its evolution; *J. Geol.* **94(2)** 145–166.

Ridolfi F, Renzulli A and Puerini M 2010 Stability and chemical equilibrium of amphibole in calc-alkaline magmas: An overview, new thermobarometric formulations and

application to subduction-related volcanoes; *Contrib. Mineral. Petrol.* **160** 45–66.

Ridolfi F and Renzulli A 2012 Calcic amphiboles in calc-alkaline and alkaline magmas: Thermobarometric and chemometric empirical equations valid up to 1130°C and 2.2 GPa; *Contrib. Mineral. Petrol.* **163** 877–895.

Rock N M S 1991 Lamprophyres, Thomson Litho Ltd, East Kilbride, 285p.

Roeder P L 1994 Chromite: From the fiery rain of chondrules to the Kilauea Iki lava lake; *Can. Mineral.* **32** 729–746.

Roeder P L and Emslie R 1970 Olivine-liquid equilibrium; *Contrib. Mineral. Petrol.* **29(4)** 275–289.

Rollinson H 2008 The geochemistry of mantle chromitites from the northern part of the Oman ophiolite: Inferred parental melt compositions; *Contrib. Mineral. Petrol.* **156(3)** 273–288.

Rudnick R and Fountain D 1995 Nature and composition of the continental crust: A lower crustal perspective; *Rev. Geophys.* **33(3)** 267–309.

Rutherford M J 1969 An Experimental determination of iron biotites – alkali feldspars equilibria; *J. Petrol.* **10** 381–408.

Scarrow J H, Molina J F, Bea F and Montero P 2009 Within plate calc-alkaline rocks: Insights from alkaline mafic magma peraluminous crustal melt hybrid appinites of the central Iberian Variscan continental collision; *Lithos* **110** 50–64.

Schaltegger U 1997 Magma pulses in the Central Variscan Belt: Episodic melt generation and emplacement during lithospheric thinning; *Terra Nova* **9** 242–245.

Schmidt M W 1992 Amphibole composition in Tonalite as a function of pressure, an experimental calibration of the Al-in–hornblende barometer; *Contrib. Mineral. Petrol.* **110** 304–310.

Sen S 1956 Structures of porphyritic granite and associated rocks in east Manbhum, Bihar, India; *Bull. Geol. Soc. Am.* **67** 647–670.

Sisson T W and Grove T L 1993 Experimental investigations of the role of $H_2O$ in calc-alkaline differentiation and subduction zone magmatism; *Contrib. Mineral. Petrol.* **113** 143–166.

Słaby E and Martin H 2008 Mafic and felsic magma interaction in granites: The Hercynian Karkonosze Pluton (Sudetes, Bohemian Massif); *J. Petrol.* **49(2)** 353–391.

Solgadi F, Moyen J F, Vanderhaeghe O, Sawyer E W and Reisberg L 2007 The role of crustal anatexis and mantle-derived magmas in the genesis of synorogenic Hercynian granites of the Livradois area, French Massif Central; *Can. Mineral.* **45(3)** 581–606.

Sun S and McDonough W F 1989 Chemical and isotopic systematics of oceanic basalts: Implications for mantle compositions and processes; In: *Magmatism in the Ocean Basins* (eds) Saunders A D and Norry M J, *Geol. Soc. London, Spl. Publ.* **42** 313–345.

Taylor W R 1998 An experimental test of some geothermometer and geobarometer formulations for upper mantle peridotites with application to the thermobarometry of fertile lherzolite and garnet websterite; *Neues Jb. Miner. Abh.* **172** 381–408.

Trubac J, Vrana S, Haluzova E and Ackerman L 2015 Petrology and geochemical characteristics of phlogopite pyroxenite related to durbachites, Moldanubian Zone, Bohemian Massif; *J. Geosci.* **60(2)** 73–90.

Wells R A 1977 Pyroxene Thermometry in simple and complex systems; *Contrib. Mineral. Petrol.* **62** 129–139.

Winter J D 2002 An Introduction to Igneous and Metamorphic Petrology, 1st edn, Pearson Education Inc., New York, pp. 1–745.

Wood B J and Banno S 1973 Garnet orthopyroxene and orthopyroxene clinopyroxene relationships in simple and complex systems; *Contrib. Miner. Petrol.* **42** 109–124.

Wyllie P J 1995 Experimental petrology of upper mantle materials, processes and products; *J. Geodyn.* **20** 429–468.

Zhang J, Humphreys M C S, Cooper G F, Davidson J P and Macpherson C G 2017 Magma mush chemistry at subduction zones, revealed by new melt major element inversion from calcic amphiboles; *Am. Mineralogist.* **102(6)** 1353–1367.

Zhao Z F, Dai L Q and Zheng Y F 2013 Post-collisional mafic igneous rocks record crust–mantle interaction during continental deep subduction; *Sci. Rep.* **3(3413)** 1–6.

Corresponding editor: Rajneesh Bhutani